

ORGANIC THIN-FILM TRANSISTORS
BASED ON
DIPOLAR SQUARAIN DYES

Dissertation zur Erlangung des
naturwissenschaftlichen Doktorgrades
der Julius-Maximilians-Universität Würzburg

vorgelegt von
Marcel Gsänger
aus Gunzenhausen

Würzburg 2013

Eingereicht bei der Fakultät für Chemie und Pharmazie am 13. März 2013

Gutachter der schriftlichen Arbeit:

1. Gutachter: Prof. Dr. Frank Würthner
2. Gutachter: Prof. Dr. Jens Pflaum

Prüfer des öffentlichen Promotionskolloquiums:

1. Prüfer: Prof. Dr. Frank Würthner
2. Prüfer: Prof. Dr. Jens Pflaum
3. Prüfer: Prof. Dr. Christoph Lambert

Datum des öffentlichen Promotionskolloquiums:

05. August 2013

Doktorurkunde ausgehändigt am

für meine Eltern

Danksagung

Meinem Doktorvater, Herrn Prof. Dr. Frank Würthner danke ich für die Überlassung des sehr interessanten Forschungsthemas, seine immerwährende Unterstützung im Fortgang meiner Promotion, seine Anregungen und die ausgezeichneten Arbeitsbedingungen im Arbeitskreis Würthner.

Bei Dr. Matthias Stolte bedanke ich mich für die lehrreichen Diskussionen, seine hilfreichen Ideen bei der Konstruktion der Apparatur für das *solution shearing*, die Durchführung der EOAM, das Korrekturlesen dieser Arbeit und das gute Arbeitsklima in unserem Büro.

Herrn Dr. Christian Burschka danke ich für die Unterstützung bei der Messung der Kristalle und bei der Lösung der Kristallstruktur.

Herrn Dr. Vladimir Stepanenko danke ich für die AFM und SEM Aufnahmen und für seine stete Hilfsbereitschaft bei der Diskussion der Ergebnisse.

Frau Ana-Maria Krause danke ich für die Durchführung von DSC und CV Messungen und ihre immerwährende Hilfsbereitschaft.

Herrn Prof. Dr. Jens Pflaum danke ich für seine Hilfsbereitschaft, die Unterstützung bei der Interpretation meiner Ergebnisse sowie die XRD-Messungen der Dünnschichtproben.

Frau Prof. Dr. Anke Krüger und Ihrem Arbeitskreis danke ich für die Ermöglichung der TGA-Messungen.

Ganz besonders bedanke ich mich bei Herrn Dr. Peter Frischmann und Herrn Dr. Gustavo Fernández für das Korrekturlesen meiner Arbeit.

Herrn Dr. Ulrich Mayerhöffer und Frau Eva Kirchner danke ich für das Überlassen der in dieser Arbeit untersuchten Squarainfarbstoffe.

Herrn Dr. Hagen Klauk und Frau Dr. Ute Zschieschang danke ich für das Überlassen der TPA- und FOPA-Substrate, die freundliche Unterstützung und die lehrreichen Diskussionen.

Frau Eva Kirchner und Herrn Robert Hofmockel danke ich für die Unterstützung, die gute Zusammenarbeit und das freundschaftliche Arbeitsklima während ihrer Hiwi-Zeit.

Frau Christiana Toussaint danke ich für die Hilfe in allen organisatorischen Belangen.

Herrn Bernd Brunner danke ich für die Unterstützung bei allen Computerproblemen.

Herrn Michael Ramold danke ich für den Bau der Apparatur für das *solution shearing* und seine schnelle, fachlich versierte Hilfe bei der Lösung einer Vielzahl technischer Herausforderungen.

Ulrich, Sabin, Moritz und Matthias danke ich für die vielen hilfreichen Diskussionen und ihre stete Hilfsbereitschaft.

Matthias und Michael aus dem Arbeitskreis Groll sage ich ein Dankeschön für die angenehme Zusammenarbeit im Labor und die immerwährende gute Laune der beiden.

Bei allen aktuellen und ehemaligen Mitarbeitern des AK Würthner bedanke ich mich für die schöne Zeit, die angenehme Arbeitsatmosphäre aber auch für die Mittwochabende.

Hannah, Steffi, Susi, Tine, Verena, André, Ben, Felix, Jojo, Sabin, Martin und Ulrich danke ich für die vielen schönen Abende und Unternehmungen sowie dafür, dass sie immer ein offenes Ohr für mich hatten.

Ganz besonderer Dank gebührt meiner Familie, vor allen Dingen meinen Eltern, für die unschätzbare Unterstützung, ohne die mein Studium nicht möglich gewesen wäre.

List of Abbreviations

AFM	atomic force microscopy
a-Si:H	hydrogenated amorphous silicon
BC	bottom-contact
BG	bottom-gate
BHJ	bulk heterojunction
CV	cyclic voltammetry
DOS	density of states
DPP	diketopyrrolopyrrole
DSC	differential scanning calorimetry
EOAM	electro optical absorption measurements
FOPA	12,12,13,13,14,14,15,15,16,16,17,17,18,18,18H-pentadecafluorooctadecyl phosphonic acid
HMDS	hexamethyldisilazane
HOMO	highest occupied molecular orbital
ITO	indium tin oxide
LUMO	lowest occupied molecular orbital
MC	merocyanine
MOSFET	metal-oxide semiconductor field-effect transistor
NDI	1,4:5,8-naphthalenetetracarboxylic diimide
NIR	near infrared
NDA	1,4:5,8-naphthalenetetracarboxylic dianhydride
<i>o</i> -DCB	<i>ortho</i> -dichlorobenzene
(O)FET	(organic) field-effect transistor
OLED	organic light emitting diode
OPM	optical polarizing microscopy
OTES	<i>n</i> -octadecyltriethoxysilane
(O)TFT	(organic) thin-film transistor
OTS	octadecyltrichlorosilane
P3HT	poly(3-hexylthiophene)
Pc	phthalocyanine
PCBM	[6,6]-phenyl-butyric-acid methyl ester
PCE	power-conversion efficiencies
PDI	3,4:9,10-perylenetetracarboxylic diimide
PMMA	poly(methyl methacrylate)
PDA	3,4:9,10-perylenetetracarboxylic dianhydride
PVP	poly-4-vinylphenol
RC	rocking curve
RMS	root mean square
SAM	self-assembled monolayer
SEM	scanning electron microscopy
TC	top-contact
TEM	transmission electron microscopy
TGA	thermogravimetric analysis
TPA	tetradecylphosphonic acid
UV/Vis	ultraviolet/visible
XRD	X-ray diffraction

Table of Contents

CHAPTER 1	INTRODUCTION AND AIM OF THESIS	1
CHAPTER 2	STATE OF KNOWLEDGE	4
2.1	Thin-Film Transistors	4
2.2	Charge Transport in Organic Materials	10
2.3	Deposition Methods for the Fabrication of Organic Semiconductor Thin-Films	13
2.4	Organic Semiconductor Materials based on Organic Colorants	18
2.4.1	Phthalocyanines	19
2.4.2	Arylene Diimides	25
2.4.3	Diketopyrrolopyrroles	30
2.4.4	Merocyanines	33
2.4.5	Squaraines	35
CHAPTER 3	RESULTS AND DISCUSSION	37
3.1	Squaraine-Based Thin-Film Transistors – Deposition by Spin Coating	37
3.1.1	Performance of the Transistor Devices	37
3.1.2	Spectroscopic and AFM Studies	40
3.2	Squaraine-Based Thin-Film Transistors – Deposition by Solution Shearing	45
3.2.1	The Solution Shearing Method	45
3.2.2	Optimization of the Processing Conditions	46
3.2.3	Performance and Long Term Stability of Transistor Devices Prepared under Optimized Conditions	49
3.2.4	Spectroscopic and AFM Studies of the Thin-Films	54
3.2.5	X-Ray Analysis of the Thin-Films and Crystal Structure of SQc	58
3.3	Squaraine-Based Thin-Film Transistors – Deposition by Vacuum Sublimation	62
3.3.1	Performance of the Transistor Devices	62
3.3.2	Spectroscopic and AFM Studies of the Thin-Films	65
CHAPTER 4	SUMMARY IN ENGLISH	69
CHAPTER 5	SUMMARY IN GERMAN	75
CHAPTER 6	EXPERIMENTAL SECTION	81
6.1	Equipment, Methods and Materials	81
6.2	Substrates	86
6.3	Thin-Film Deposition	88

6.3.1	Spin Coating	88
6.3.2	Solution Shearing	88
6.3.3	Vapor Deposition	89
6.4	Device Fabrication and Characterization	90
6.5	Crystal Structure Data of SQc	91
REFERENCES		94
LIST OF PUBLICATIONS		104

CHAPTER 1

—

INTRODUCTION AND AIM OF THESIS

Modern electronics is not possible to imagine without a small but important component – the transistor, which is used to amplify or switch an electrical signal.^[1] Such devices are ubiquitous elements of integrated circuits such as microprocessors or random-access memory (RAM) elements applied in ordinary information and communication technology. Since the 1970s, monocrystalline silicon has been the traditional material used for all these applications. Temperatures of approximately 1500 °C are required during the fabrication of monocrystalline silicon, leading to high energy consumption as well as high manufacturing costs. However, these processing conditions are not applicable for large-area applications such as active matrix displays, which is the most common implementation of thin-film transistors (TFT). The devices are used in active matrix displays to switch the individual pixels of the display. Hydrogenated amorphous silicon (a-Si:H) is applied as the most common, state-of-the-art semiconducting material. Large-scale manufacturing was realized by deposition of the active layer by sublimation at high vacuum. Although this process takes place at lower temperatures than for monocrystalline silicon, elevated temperatures are still required for a-Si:H sublimation and the subsequent masking and lithographic steps performed during device fabrication. The principle disadvantage of such devices is clearly the high energy consumption required for maintaining high deposition temperatures and elaborate high-vacuum techniques.

Nowadays, demand for TFTs on flexible polymeric substrates has arisen for applications such as flexible displays^[2] or radiofrequency identification (RFID) tags^[3]. As the latter are thought to replace conventional barcodes, low-cost devices are demanded due to their single-

use only. The high temperatures during the fabrication of a-Si:H transistor devices impede the deposition on such polymeric substrates but open up the chance for using organic semiconductor materials instead. These compounds may even be processed from solution, depending on their molecular structure, giving rise to cheap and large-area processing on flexible substrates. To date, much scientific effort has been spent on the search for organic semiconductors^[4,5] and suitable deposition methods with the aim to reach the performance of a-Si:H. Organic polymers as well as small organic molecules are known to be applicable as such semiconducting materials. A large number of semiconducting organic molecules and polymers are already reported in the literature.^[5] Each class of compound features unique assets and drawbacks, e.g. small molecules are often poorly soluble whereas polymers are less likely to yield crystalline films. Despite these potential disadvantages, decent progress has been made in the development of organic electronic devices based on such materials. For example, the first flexible organic TFT driven OLED display (depicted in Figure 1) on a polymer substrate was presented in May 2010 by Sony.^[6]



Figure 1. The first flexible OLED display that can be rolled up on a pen while still displaying the video was presented in May 2010 by Sony. Reprinted with permission from ref. 6. Copyright 2011, Society for Information Display.

The search for new organic compounds providing enhanced solution processing of the active layer with respectable transistor performance is still ongoing. In 2009, the groups of Würthner and Meerholz reported on outstanding short-circuit currents of solution-processed, squaraine-based bulk-heterojunction solar cells.^[7] Additionally, they studied the performance of spin-coated transistor devices and found hole mobilities of up to $10^{-3} \text{ cm}^2 \text{ V}^{-1} \text{ s}^{-1}$.

Thus, this thesis will deal with the fabrication and characterization of TFTs based on acceptor-substituted squaraine dyes similar to those applied in organic photovoltaics in order to demonstrate their potential for thin-film transistor applications. Non-flexible substrates, namely heavily doped silicon wafers, were used for this study because these are well-

established in the community and facilitate the comparability of the results. Spin coating of a set of such squaraines initially was aimed at evaluating the influence of the chain lengths as well as of the molecular electronic structure on the transistor performance of the corresponding thin-films. The best performing molecules were selected for deposition by solution shearing, which is a method applied to attain higher film quality accompanied by better TFT characteristics as compared to spin-coated semiconductor layers. The construction of the necessary setup and the optimization of the deposition conditions are also covered by this thesis. Vacuum sublimation, known for yielding highly crystalline thin-films, was introduced as a third method to round out the investigation of the deposition techniques and of their influence on the transistor performance. Finally, the resulting devices were characterized by optical spectroscopy, atomic force microscopy and X-ray diffraction experiments to establish reliable relationships between molecular structure, crystal packing, thin-film morphology and transistor performance that may guide the development of future devices.

Chapter 2 deals with the working principle of TFTs and gives an idea of charge transport mechanisms in organic thin-film transistor (OTFT) devices. Furthermore, deposition techniques for the active layer are discussed with a focus on solution-based methods followed by a comprehensive overview of organic colorants, which have been applied as organic semiconductor materials.

Chapter 3 includes the preparation, characterization and discussion of OTFTs built from squaraine dye thin-films. While the general qualification of the squaraines for transistor applications was shown by deposition of the active layer using the spin coating method, distinct improvement of the transistor performance was achieved by performing solution shearing at previously optimized conditions with a setup constructed during this thesis. A further increase of the charge carrier mobility could be achieved by vacuum-deposition of the active layer. Optical spectroscopy, AFM studies, X-ray diffraction experiments as well as single crystal structure analysis were performed to gain insight into the packing arrangement of the films. These analyses revealed quite similar packing motifs for all deposition methods, indicated by J-type excitonic coupling. For solution-sheared samples it was even possible to identify the probable alignment of the molecules in these highly oriented thin-films.

Chapter 4 and *Chapter 5* finally give a summary of the thesis in English and German.

CHAPTER 2

—

STATE OF KNOWLEDGE

2.1 Thin-Film Transistors^[8,4d]

The concept of thin-film transistors was first introduced in the 1960s by Weimer^[9] and later successfully applied to obtain transistors composed of a-Si:H.^[10] Based on this research, fabrication of large area TFT devices was accessible, whereas crystalline silicon has one major disadvantage, namely the high processing temperatures and therefore limited range of applicable substrates, small area processing and quite thick semiconductor layers. Further progress in a-Si:H TFT fabrication has made these materials crucial elements of active-matrix liquid-crystal displays and other electronic devices.^[8a] Since the late 1980s, organic polymers as well as small organic molecules have been used to build thin-film transistors based on organic semiconductor materials.^[11]

In principle, various architectures are known for OTFTs. However, all OTFTs require the same five components: a thin layer of the organic semiconductor, an insulating dielectric, and three electrodes. Two of the components, the charge-injecting/charge-extracting source and drain electrodes, are directly attached to the semiconducting layer, while the third, the gate electrode, is isolated from the active layer by the dielectric. The most common TFT structure is the bottom-gate (BG) configuration that is schematically depicted in Figure 2. One advantage of BG devices is that no elaborate texturing of the gate electrode is necessary; hence, screening of new materials is quite easy in this configuration. Within the BG configuration, there are advantages and drawbacks depending on whether the source and drain are located on top of the semiconductor layer (top-contact (TC), Figure 2a) or at the interface of the semiconductor and dielectric (bottom-contact (BC), Figure 2b). The contacts of BG-BC

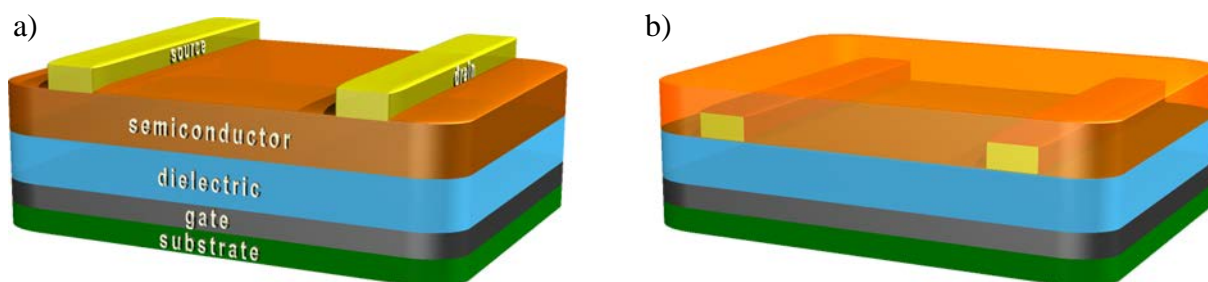


Figure 2. Most common TFT structures: a) bottom-gate, top-contact configuration. b) bottom-gate, bottom-contact configuration.

devices can be patterned well by microlithographic techniques without harming the subsequently processed active layer. However, this configuration is not beneficial for “mechanical” deposition methods of the semiconductor layer such as solution shearing, which endangers the quality of the contacts or even destroys them. Furthermore, the performance of such devices often suffers from the poor morphology of the active layer formed at the edges of the contacts.^[8e] So, the BG-TC configuration was employed for the semiconductor studies discussed in this thesis (see Chapter 3). In the BG-TC case the electrodes are deposited directly onto the semiconductor thin-film by means of shadow masks. A disadvantage of this configuration is the “access resistance” arising from the highly resistive semiconductor material located between the electrodes and the conduction channel. This effect becomes an issue for active layer widths greater than 5 nm.^[8e] However, these devices benefit from electrode metal penetration into the film leading to lower contact resistance due to improved gate-field-enhanced charge injection in such a staggered electrode configuration.^[8e]

Although flexible conducting polymers have been successfully used as gate electrodes,^[4d] highly doped silicon, which fortunately can serve as substrate at the same time, is more common for this purpose. Silicon substrates resist elevated processing temperatures, whereas polymeric substrates often suffer from low thermal stability. The active layer of an organic thin-film transistor is commonly vacuum sublimated or solution deposited by methods such as spin coating and drop casting. This topic is discussed in more detail in Chapter 2.3. Although organic polymers such as PMMA or PVP may be applied as the insulating dielectric layer, inorganic insulators (e.g. SiO₂, Al₂O₃ or Si₃N₄) are most often used for this purpose. The dielectric is essential for TFT operation, e.g. in TFTs designed for application in portable devices that require operation with low voltages. The operation voltage can be tuned by the thickness of the gate dielectric layer, which can be reduced by using dielectrics with high permittivity ϵ . However, it has been shown that an increase of the permittivity systematically reduces the charge carrier mobility,^[4d] and choosing the dielectric material is always a compromise between large gate coupling, low operating voltages, and small leakage currents.

Various materials are also available for the source and drain contacts. Noble metals, most often gold, are easily deposited by thermal evaporation in vacuum and patterned by shadow masks, photolithography or other methods. However, conducting polymers have also been employed to form the source and drain contacts due to their requirements similar to those of the gate electrode. To minimize the contact resistance of the electrodes, commonly high work function metals (such as Ag, Au, and ITO) are used to match the conduction band of p-type semiconductor materials. Low work function metals are suitable for n-type transistor operation, but suffer from their reactivity in air. Nevertheless, it was found that high work function metals still give good contacts and the resulting TFTs function well.^[8a]

While the source electrode is usually grounded during transistor operation, positive or negative voltages are applied between this and the two other electrodes (drain and gate). The potential difference between gate and source is referred to as gate voltage (V_g) and the difference between drain and source is named drain-source voltage (V_d). Depending on whether positive or negative V_d and V_g are applied to an OTFT device, negative, i.e. electrons, and positive charge carriers, i.e. holes, respectively, are injected from the source into the semiconductor. The charge carriers are accumulated in the active layer next to the interface with the dielectric and form the carrier channel of an OTFT. Organic semiconductors are known to contain approximately equal amounts of n- and p-type doping impurities. Thus they are called “compensated” materials and behave like intrinsic semiconductors. Respective OTFTs work in accumulation mode, while metal-oxide semiconductor field-effect transistors (MOSFETs) operate in inversion mode. The type of induced charge carriers not only depends on the polarity of the applied voltage, but also on the semiconductor and the metals used to form source and drain electrodes. The appropriate Fermi level of the electrodes with respect to the HOMO or LUMO levels of the organic semiconductor determines whether the material is p-type (i.e. hole transport) or n-type (i.e. electron transport), respectively (see Figure 3). HOMO and LUMO energy levels can be determined well for single molecules by methods such as cyclic voltammetry (HOMO), UV/Vis spectroscopy (LUMO) or photoelectron spectroscopy (HOMO and LUMO). Although, these values measured for molecular components cannot be considered the same as for the bulk materials, the molecular values are easily accessible experimentally and have been proven over the last few years of transistor research to be meaningful for evaluating the energy levels of the bulk materials.

The number of charge carriers accumulated in the channel depends on V_{GS} as well as on the capacitance of the dielectric (C_i). However, a gate voltage higher than a certain threshold voltage (V_{th}) has to be applied to obtain a commensurable drain current (I_d). This originates

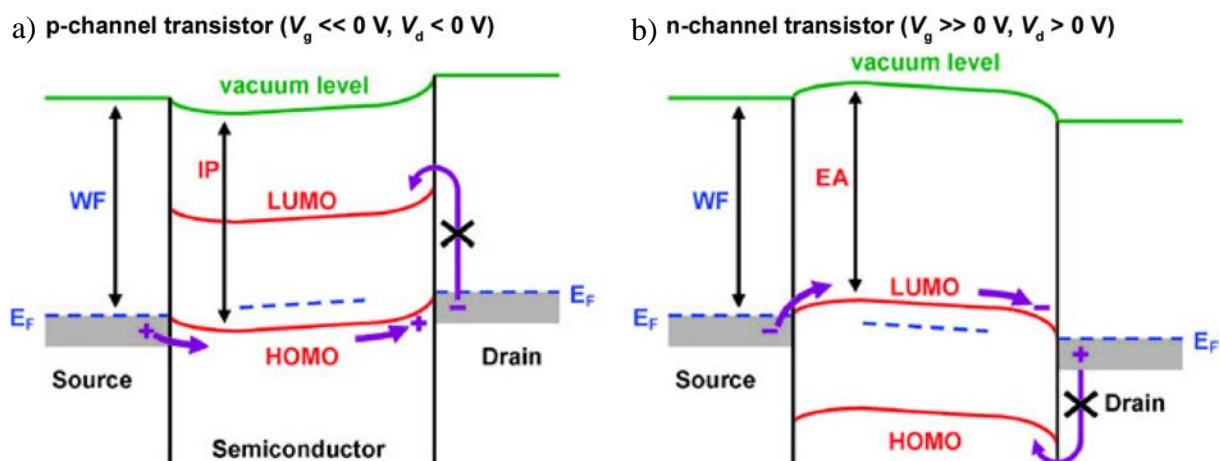


Figure 3. Energy level diagrams of a p-type (a) and n-type (b) organic field effect transistor, where the transport of holes and electrons is exemplified by the arrows. WF is the work function and E_F the Fermi level of the electrodes. IP is the ionization potential and EA the electron affinity of the semiconductor material.^[4d] Reproduced by permission of The Royal Society of Chemistry.

from deep traps in the active layer, which are overcome at $V_g = V_{th}$; further increase of V_g induces charge carriers which are, to a certain extent, mobile along the channel region (defined by the width W and the length L). It must be remembered that V_{th} is for metal-oxide semiconductor field-effect transistors defined as the minimum gate voltage needed to reach strong inversion. As this is not the case in OTFTs, this definition strictly cannot be adopted. Nevertheless the concept can also be used for OTFTs, where V_{th} marks the transition point from linear to saturation regime. Further contributions to the threshold voltage arise from grain boundaries, bending of the energy levels and interface interactions.

In general, the basic operation of field-effect transistors is explained in the following text with the help of the illustrations in Figure 4. With a gate voltage applied to the device a homogenous distribution of charge carriers in the channel region is obtained whilst no bias is applied between drain and source. A small V_d ($\ll V_g - V_{th}$) generates a linear gradient from the charge injecting source to the drain electrode. This is the so called linear operation regime of a transistor (Figure 4a), where the drain current follows Ohm's law and is therefore proportional to V_d and V_g . If the drain bias reaches $V_g - V_{th}$, a pinch off of the conduction channel is observed (Figure 4b). At this point the drain voltage exceeds the gate voltage, which leads to the formation of a depletion region next to the drain electrode. Further increase of V_d will expand this zone (Figure 4c), but will not essentially increase the drain current. This means that I_d becomes independent of the drain voltage and the saturation regime is reached.

For interpretation of the OTFT performance analytical approaches were made to extract values such as the charge carrier mobility, the on/off ratio and the threshold voltage from the transistor characteristics. If the gate bias is higher than the threshold voltage, the surface

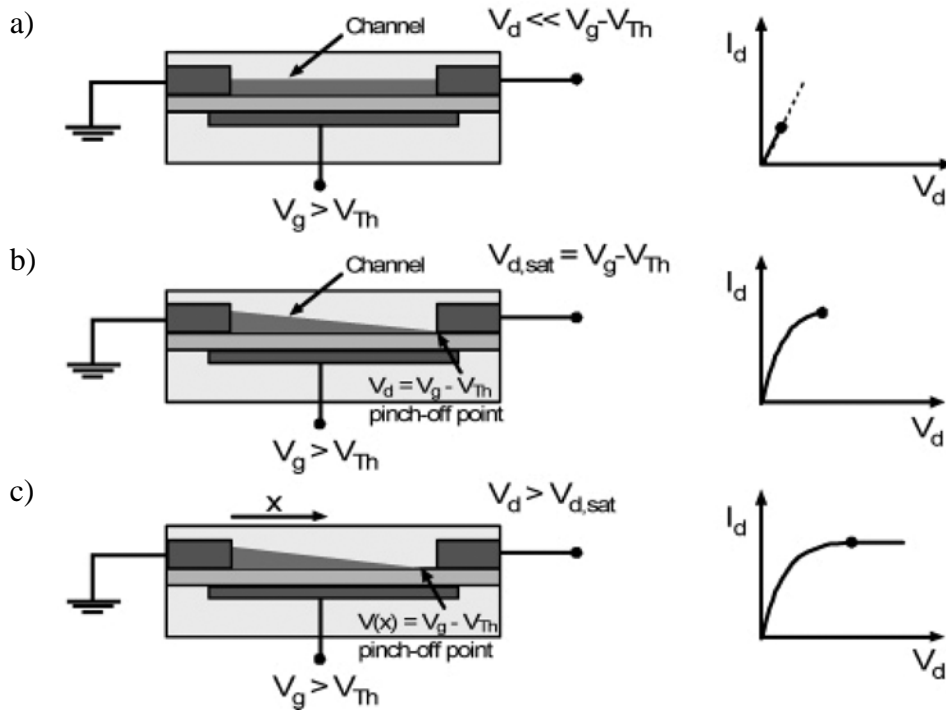


Figure 4. Transistor operation within different regimes: a) linear regime; b) at the transition point from linear to saturation regime; c) saturation regime. Reprinted with permission from ref. 8b. Copyright 2007, American Chemical Society.

charge density $Q_{\text{mob}}(x)$ of mobile charges at point x in the channel can be expressed via

$$Q_{\text{mob}}(x) = C_i (V_g - V_{\text{th}} - V(x)), \quad (2.1.1)$$

where C_i is the capacitance of the dielectric layer and $V(x)$ the potential at point x .

Several assumptions have to be made to obtain a formula, which can be used for calculation of the drain current. The first is the so-called gradual channel approximation. It means that the electric field generated by the gate voltage (z -direction) is much higher than the one perpendicular generated by the drain voltage, which is aligned along the x -direction. Second, the charge carrier mobility (μ) is assumed to be independent of the carrier density and hence the gate voltage. With the resistance, dR , of a thin element of the channel, dx , defined as

$$dR = \frac{dx}{WQ_{\text{mob}}(x)\mu}, \quad (2.1.2)$$

substituting $dR = I_d dR$ and subsequent integration over the whole channel length gives

$$I_d = \frac{W}{L} \mu C_i \left[(V_g - V_{\text{th}}) V_d - \frac{V_d^2}{2} \right]. \quad (2.1.3)$$

This general formula can be applied both to the linear and the saturation regime. In the first case of $V_d \ll V_g - V_{\text{th}}$, and hence it simplifies to

$$I_d = \frac{W}{L} \mu_{\text{lin}} C_i (V_g - V_{\text{th}}) V_d. \quad (2.1.4)$$

The channel is pinched off in the second case when $V_d \geq V_g - V_{\text{th}}$ and therefore the drain current can be expressed as

$$I_d = \frac{W}{2L} \mu_{\text{sat}} C_i (V_g - V_{\text{th}})^2. \quad (2.1.5)$$

Rearrangement of Eq. 2.1.4 and 2.1.5 leads to expressions for the charge carrier mobility in the linear as well as in the saturation regime:

$$\mu_{\text{lin}} = \frac{L}{C_i W V_d} \frac{\partial I_d}{\partial V_g}, \quad (2.1.6)$$

$$\mu_{\text{sat}} = \frac{2L}{C_i W} \left(\frac{\partial \sqrt{I_d}}{\partial V_g} \right)^2. \quad (2.1.7)$$

An exemplary output characteristic for a typical n-channel organic field-effect transistor, where the drain current is plotted against the drain voltage for various gate voltages, is shown in Figure 5a. Linear operation of the device at low V_d as well as the gradual transition to the saturation regime at high V_d can easily be seen. From the semi-logarithmic plot of I_d against V_g at constant V_d (the so-called transfer characteristic, Figure 5b and c) the onset voltage, V_{on} , can be extracted. This is the gate voltage after which a dramatic increase of the drain current is observed and that may be used as a characteristic value instead of the threshold voltage because of the more meaningful definition of V_{on} . The linear plot of the drain current against gate voltage depicts the proportionality of both values at low V_d (Eq. 2.1.4, Figure 5b). From this plot it is possible to extract μ_{lin} from the gradient according to Eq. 2.1.6. For the saturation regime, the square root of the drain current is plotted against the gate voltage and should

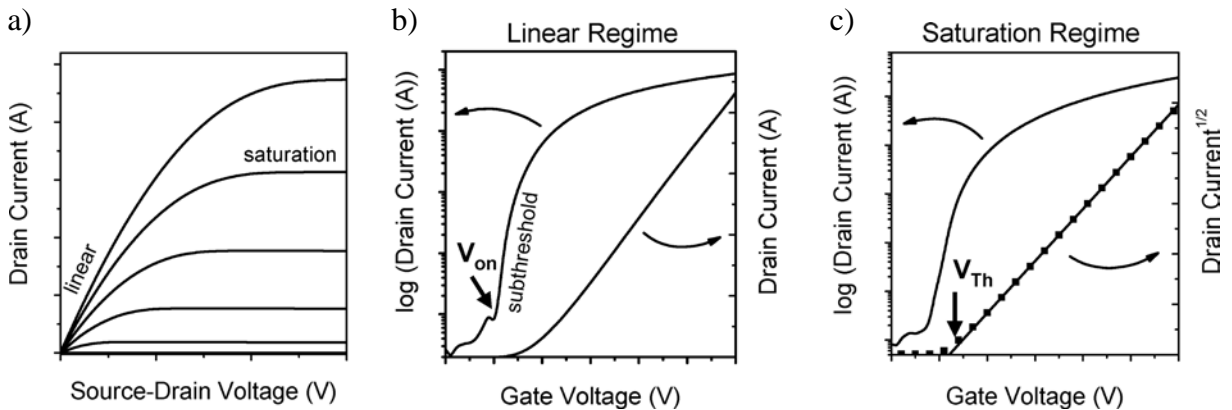


Figure 5. Output characteristic of a typical n-channel organic field-effect transistor for various V_g (a), transfer characteristics in the linear regime with $V_d \ll V_g - V_{\text{th}}$ (b), and in the saturation regime with $V_d > V_g - V_{\text{th}}$. Reprinted with permission from ref. 8b. Copyright 2007, American Chemical Society.

exhibit a linear dependence on V_g (Figure 5c). Here the gradient can be used to obtain μ_{sat} from Eq. 2.1.7, while linear extrapolation to the abscissa yields V_{th} .

High mobility is a favorable feature of organic thin-film transistors, since this leads to increased switching speeds of integrated circuits. Furthermore, threshold voltages near to 0 V are desirable, because only low gate voltages are needed to switch the transistor between on- and off-states. Finally, a high on/off ratio ($I_{\text{on}}/I_{\text{off}}$), *i.e.* the ratio of the drain current in the on-state and the drain current in the off-state, is a feature of high-performance transistor devices, where the smallest possible value of I_{off} is desired. That means that the leakage current in the channel and therefore the power consumption in the off-state of the transistor are minimized.

2.2 Charge Transport in Organic Materials^[12]

Since the discovery of organic semiconductor materials, researchers have studied the underlying mechanisms of charge transport. Hence, in the past 60 years numerous studies have been carried out. The main breakthrough was achieved in the mid-1970s by a theoretical description of hopping transport in disordered materials^[13], which was later subjected to a Monte-Carlo simulation by Bässler and co-workers^[14].

In general, band transport is the dominating mechanism in crystalline inorganic semiconductor materials giving rise to high charge carrier mobilities (more than $1,000 \text{ cm}^2 \text{ V}^{-1} \text{ s}^{-1}$ in single-crystal silicon^[15]). This can be explained by the linkage of the atoms by covalent bonds. That is, the electronic interactions between the atomic orbitals are strong leading to the formation of broad bands, the valence and conduction band. For single-crystalline organic semiconductors the molecular interactions are much weaker, because mostly van der Waals interactions link individual molecules. In consequence, weaker electronic interactions result and hence narrow bands are formed. This means, band transport with high charge carrier mobilities (up to $20 \text{ cm}^2 \text{ V}^{-1} \text{ s}^{-1}$ at room temperature^[12b]) can be observed only in very pure organic molecular crystals from low temperatures up to room temperature. However, at higher temperatures charge carriers are scattered in organic crystals with a mean free path in the order of the distance between adjacent molecules. Band transport is no longer possible and hence hopping transport becomes the dominating charge transport mechanism.^[12c]

Finally, things look quite different in organic thin-films, e.g. deposited by spin-coating or vacuum sublimation. Generally speaking, charge transport in organic semiconductor materials is based on the injection of an electron into the LUMO and the extraction of an electron from the HOMO-level of the molecule, respectively. This leads to an alteration of the distribution

of the remaining electrons resulting in changes in the bond lengths of the molecule. The energy resulting from this process is known as the geometric reorganization energy, while the interaction of a charge with the surrounding molecules is called a polaron. Due to the fact that organic semiconducting materials have quite low dielectric constants ($\epsilon \approx 3$), electron-electron correlations and electron-phonon couplings are present that are not observed for inorganic semiconductor crystals with higher dielectric constants ($\epsilon \approx 11$).

As long as chemical and physical defects (the so-called off-diagonal disorder) can be neglected, the charge transport in organic semiconductor materials is restricted only by the dynamic diagonal disorder arising from electron-phonon coupling. Polaronic transport may be split up into two cases, namely weak and strong electron-phonon coupling. For the first the charge carrier mobility is dominated by tunneling and hence a band-like temperature dependence of the mobility is found. Strong coupling leads to a lowering of the site energy by the polaron binding energy, which has to be overcome by thermal activation before the charge carriers can move further. This can be described as a phonon-assisted hopping process, where the degree of polaron coupling is decisive for the measurable charge carrier mobility, i.e. μ increases with temperature.^[12d]

In the early years of this research field, thin-films of organic semiconductors were mostly amorphous which means that static off-diagonal disorder has to be taken into consideration. The arbitrary orientation of molecules in such films together with random variations of the surrounding polarization induce a random distribution of the molecular energies. The resulting distribution of state energies is generally assumed to be of Gaussian shape (see Figure 6) with the width being dependent on the dipole moment and the polarizability of the

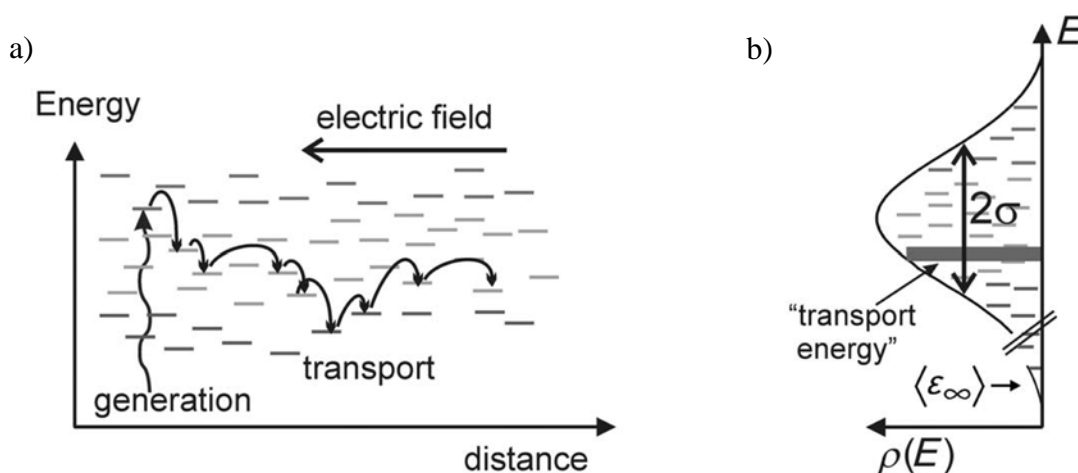


Figure 6. Schematic depiction of the hopping transport according to the model developed by Bässler (a) and distribution of the density of states for a disordered organic semiconductor material (b). Reprinted with permission from ref. 12d. Copyright 2008, WILEY-VCH Verlag GmbH & Co. KGaA, Weinheim.

semiconductor material.^[16] In other words, the band states of highly ordered materials are more and more localized on introduction of increasing disorder. As a consequence, uncorrelated hopping of charge carriers within a wide distribution of states is the dominant transport mechanism. Bäessler and co-workers developed a description for the charge transport in such disordered organic materials based on Monte-Carlo simulations.^[14] One has to take into account the charge hopping rates between sites as well as the density of the hopping states. The hopping rate ν_{ij} from an initial site i with energy E_i to a final site f with energy E_f can be expressed according to the Miller-Abrahams formalism^[17] as

$$\nu_{ij} = \nu_0 \exp\left(-2\gamma a \frac{r_{ij}}{a}\right) \cdot \begin{cases} \exp\left(-\frac{E_j - E_i}{kT}\right) & \text{if } E_j > E_i \\ 1 & \text{if } E_j < E_i, \end{cases} \quad (2.2.1)$$

with ν_0 a frequency pre-factor, r_{ij} the jump distance, a the intersite distance, and γ the inverse wave function localization radius. The energy of the states E may be expressed, as stated above, by a Gaussian distribution:

$$Q(E) = \frac{1}{\sqrt{2\pi}\sigma} \exp\left(-\frac{E^2}{2\sigma^2}\right), \quad (2.2.2)$$

where σ represents here the width of the density of states. With Eq. 2.2.1 and 2.2.2 subjected to a Monte-Carlo simulation, several statements on the hopping transport are possible. First, charge carriers relax into the tail of the density of states (DOS) distribution during the simulation; dispersive transport is the consequence. After reaching equilibrium, the mean energy of a charge carrier is dependent on disorder and temperature, and can be described as

$$\langle E_{\text{eq}} \rangle = \lim_{t \rightarrow 0} \langle E(t) \rangle = -\frac{\sigma^2}{kT}. \quad (2.2.3)$$

It is evident from this equation that the energy of the carriers decreases on decreasing temperature and, as a consequence thereof, the activation energy for a hop of the charge carrier to the transport energy level increases. Hence higher temperature also means higher mobilities. Second, a general expression for the charge carrier mobility in disordered organic semiconductors regarding the temperature and field dependence can be formulated as

$$\mu(T, F) = \mu_0 \exp\left[-\left(\frac{2\sigma}{3kT}\right)^2\right] \cdot \begin{cases} \exp\left[C(\sigma^2 - \Sigma^2)\sqrt{F}\right] & \text{if } \Sigma \geq 1.5 \\ \exp\left[C(\sigma^2 - 2.25)\sqrt{F}\right] & \text{if } \Sigma \leq 1.5 \end{cases}, \quad (2.2.4)$$

where C is a numerical constant. It accounts for the fact that the activation energy for charge transport is decreased by tilting of the DOS due to superposition of an electric field. So, a

Poole-Frenkel behavior can be stated for the charge transport in amorphous organic semiconductor films, where the mobility increases with the electric field strength. In summary, it can be stated that higher disorder broadens the density of states, increases the temperature and field dependence, and finally leads to low mobility transistor devices.

Beyond the model of Bässler presented here, some other theories for describing the charge transport in disordered organic materials have been reported in the literature over the years eliminating some drawbacks of the Bässler model.^[18] Vissenberg and Matters, for example, developed a variable-range hopping transport model, which is in contrast to the Bässler model directly applicable to the relatively high charge carrier concentrations in the accumulation layer of an OTFT.^[18a]

2.3 Deposition Methods for the Fabrication of Organic Semiconductor Thin-Films^[19]

The semiconductor layer is one of the vital elements in a TFT device determining the transistor performance. Hence, the deposition of the semiconductor plays an important role in the fabrication process, because at this step the morphology of the semiconductor film has to be built up in a fashion which promotes charge transport and leads to high charge carrier mobilities. One way to reach this goal is to improve the semiconductor / dielectric interface by modifying the surface of the dielectric with a self-assembled monolayer (SAM) of a silane or phosphonic acid. Besides determining the influence of the SAM on the molecular structure and morphology, the operating voltage of the OTFT can be significantly reduced by such a SAM.^[19b] Additionally, the deposition method affects the morphology of the active layer, and various methods are known to achieve high-quality semiconductor thin-films. In general, one has to select the right deposition method for the semiconductor layer depending on the kind of compound to be processed. Due to solubility reasons, for polymer materials mostly solution-based techniques are chosen, while small molecules often may be processed by thermal sublimation at high vacuum. It is well known that the thin-film morphology can be optimized by tuning the temperature of the substrate and the deposition rate of the organic material.^[20] Finally, the substrate has to be compatible with the deposition method, e.g. vapor deposition often requires high temperatures and is therefore not a suitable method for transistor fabrication on polymer substrates.

Intensive research in the field of small semiconductor molecules led to the discovery of new highly soluble compounds during the last decade. Consequently, fabrication of the OTFT semiconductor layer from solution has become increasingly important. Thus, several solution

deposition methods have been developed. As this thesis is focused on small molecule semiconductors and their processing from solution, a selection of relevant deposition methods is discussed in the following text.

The most common methods are drop casting and spin coating. Both are quite fast and hence suitable for initial screening of new semiconductor materials. For drop casting^[21], a certain amount of the semiconductor solution is placed on the substrate followed by evaporation of the low boiling solvent. Usually irregular films of low crystallinity are obtained by this method and the respective OTFTs perform quite badly. Spin coating^[22] yields more uniform thin-films. For this method, the substrate is completely covered by the solution and rotated at high speed. The fluid spins off at the edges leading to simultaneous evaporation of the solvent and thus to film formation from the center of the substrate. The thickness of the film depends on the speed of rotation, the concentration of the solution and the solvent, which usually is volatile. Treatment of the spin-coated films in vacuum or inert atmosphere at elevated temperatures is often beneficial for improved film quality. For example, Piliago *et al.* reported spin-coated and subsequently annealed films of *N,N'*-1*H*,1*H*-perfluorobutyl dicyanoperylene-carboxydiimide with electron mobilities of up to $0.15 \text{ cm}^2 \text{ V}^{-1} \text{ s}^{-1}$ in vacuum.^[23] Usually, uniform films consisting of randomly oriented molecules are obtained by this procedure. Ludwigs, Crossland and co-workers managed to obtain well-oriented films by spin coating of regioregular poly(3-hexylthiophene) (P3HT) followed by solvent vapor treatment.^[24] Anisotropic charge transport was found within the large spherulites, which was dependent on the orientation of the transistor channel with respect to the growth direction of the spherulite. Hole mobilities up to $0.2 \text{ cm}^2 \text{ V}^{-1} \text{ s}^{-1}$ were measured for devices aligned perpendicular to the radial spherulite growth direction, while OTFTs with parallel orientation exhibited charge carrier mobilities of only $0.07 \text{ cm}^2 \text{ V}^{-1} \text{ s}^{-1}$. Despite P3HT being a polymeric semiconductor, one can assume that well-oriented thin-films with a high degree of crystallinity are also desirable features for high performance OTFT devices based on small molecules.

Müllen and co-workers used the zone-casting technique (the principle is depicted in Figure 7b) for fabrication of devices based on discotic hexa-*peri*-hexabenzocoronene (see Figure 7a).^[25a] Columnar structures providing percolation pathways for charge carriers were observed. An increase in charge mobility of nearly two orders of magnitude (up to $0.01 \text{ cm}^2 \text{ V}^{-1} \text{ s}^{-1}$) was determined for OTFTs deposited by zone-casting compared to drop-casting. In the zone-casting method the solution of the organic semiconductor was supplied through a nozzle with a meniscus onto the substrate, which is slowly moving (see Figure 7b).

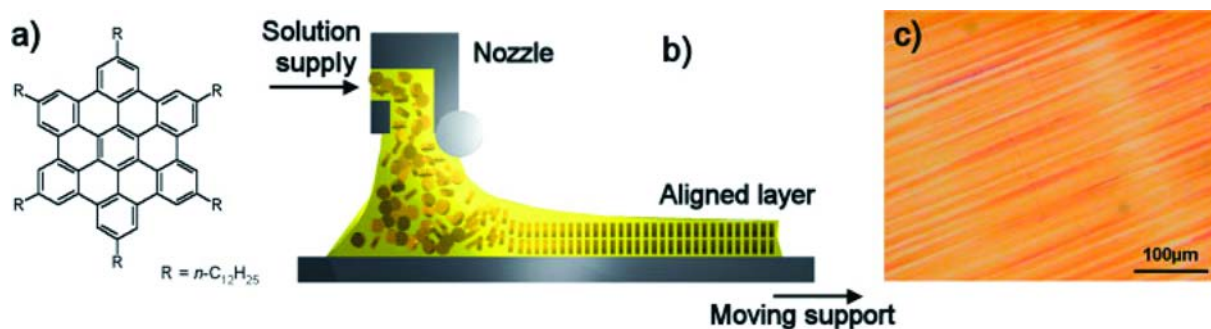


Figure 7. a) Chemical structure of the hexabenzocoronene derivative used for OTFT fabrication. b) Schematic depiction of the zone-casting technique. c) Optical microscopy picture of a zone-casted thin-film taken in reflection mode. Reprinted with permission from ref. 25a. Copyright 2005, WILEY-VCH Verlag GmbH & Co. KGaA, Weinheim.

A concentration gradient is formed along the meniscus due to evaporation of the solvent. Optimization of the concentration, deposition speed, solvent and temperature results in efficient self-assembly upon reaching a critical concentration. The self-assembled structures are deposited onto the substrate along the deposition direction, forming an aligned thin-film. The high quality of such hexabenzocoronene-based films is visualized by the microscopy picture in Figure 7c. Mas-Torrent *et al.* prepared highly oriented thin-films of dithiophene-tetrathiafulvalene by using the same procedure.^[25b] They successfully fabricated transistor devices with these films and measured charge carrier mobilities up to $0.17 \text{ cm}^2 \text{ V}^{-1} \text{ s}^{-1}$. Remarkably, their mobility is only one order of magnitude lower than the values measured for single-crystal devices.

Very recently, Jang *et al.* reached hole mobilities up to $1.5 \text{ cm}^2 \text{ V}^{-1} \text{ s}^{-1}$ for uniform large-area highly crystalline organic semiconductor thin-films prepared by the dip-coating method.^[26] Hereby a substrate is slowly withdrawn out of a solution of 6,13-bis(triisopropylsilylethynyl) pentacene and fluorinated 5,11-bis(triethylsilylethynyl) anthradithiophene, respectively (for a schematic depiction see Figure 8b). A meniscus is formed at the interface between the substrate and the solution leading to a concentration gradient along the direction of the movement, which induces alignment of the molecules. Growth of large-scale crystalline films (see Figure 8a) was reported for certain lifting-rates using low boiling solvents at optimized temperatures. It is noteworthy, that this method could also be applied successfully for constructing OTFTs on unconventional cylinder-shaped substrates.

Bao and co-workers developed and optimized another method for thin-film deposition known as solution shearing.^[27] As this method was applied for transistor fabrication within this thesis, a more detailed description of this procedure can be found in Chapter 3.2.1, while it will only be briefly covered here. Lee *et al.* covered substrates with solutions of

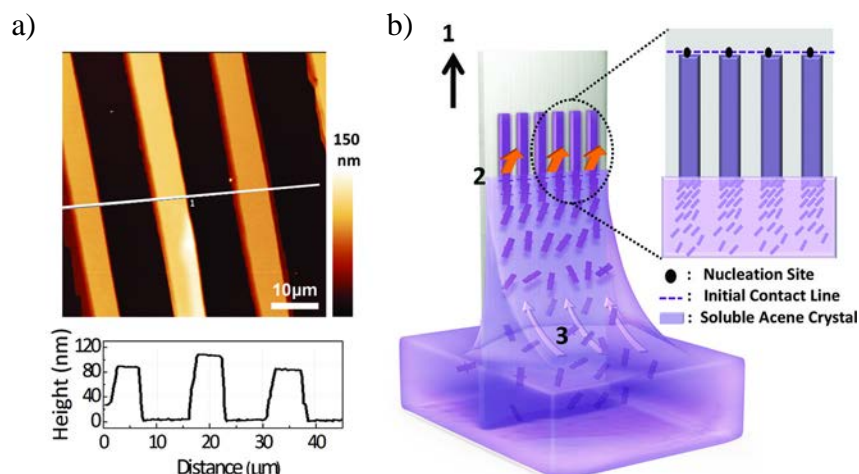


Figure 8. a) AFM image of 6,13-bis(triisopropylsilylethynyl) pentacene-based crystalline films grown by dip-coating. b) Schematic depiction of the dip-coating method. Reprinted with permission from ref. 26. Copyright 2012, WILEY-VCH Verlag GmbH & Co. KGaA, Weinheim.

dichlorinated NDIs bearing fluorinated alkyl chains.^[27c] When moving a shearing tool with a dewetting surface over the substrate, they obtained well-oriented thin-films over a large area. Devices based on these films revealed air-stable electron mobilities of up to $0.57 \text{ cm}^2 \text{ V}^{-1} \text{ s}^{-1}$. This is quite remarkable if one takes into account that the mobilities of vacuum-deposited and spin-coated films of the same compound are in the range of about $1.4 \text{ cm}^2 \text{ V}^{-1} \text{ s}^{-1}$ ^[27d] and $10^{-3} - 10^{-4} \text{ cm}^2 \text{ V}^{-1} \text{ s}^{-1}$ ^[27c], respectively.

Besides these mechanical procedures, surface selective deposition of the semiconductor material^[28] and directed crystal growth at the gap between a hydrophobic surface and a solution holding piece^[29] are examples for fabrication of highly oriented and crystalline thin-films from solution. In the first case, a substrate is pre-patterned with solution-wettable and non-wettable self-assembled monolayers.^[28] Applying a chlorobenzene solution of dioctylbenzothienobenzothiophene onto the patterned substrate yields self-organized organic semiconductor layers at the selected regions of the surface (Figure 9). Large sized grains and

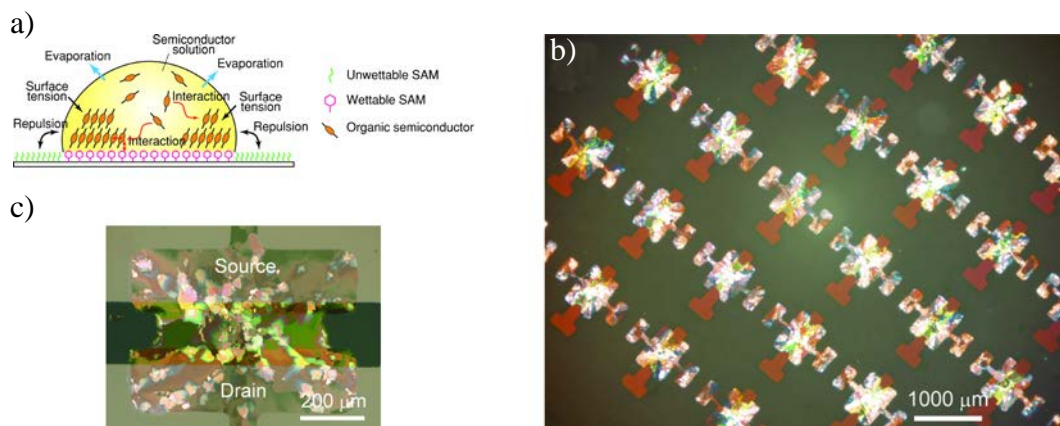


Figure 9. a) Schematic depiction of surface selective deposition of a semiconductor solution. b) OPM picture of an array of self-organized and crystalline transistor devices and c) of a single transistor device. Reprinted with permission from ref. 28a. Copyright 2009, American Institute of Physics.

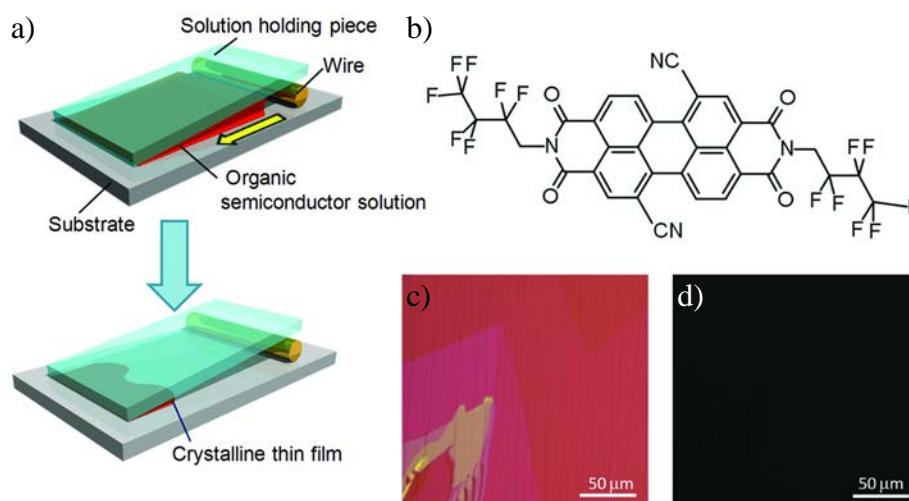


Figure 10. a) Schematic depiction of the method used for the fabrication of highly crystalline thin-films of *N,N'*-1*H*,1*H*-perfluorobutyldicyanoperylene-carboxydi-imide (b). c) to d) OPM pictures of the crystalline films with polarizer and analyzer at different angles with respect to each other. Reprinted with permission from ref. 29. Copyright 2011, WILEY-VCH Verlag GmbH & Co. KGaA, Weinheim.

layer by layer growth were observed within the fully covered channel region, where electron mobilities ranged from 0.2 to $1.5 \text{ cm}^2 \text{ V}^{-1} \text{ s}^{-1}$.

Facchetti, Takeya and co-workers developed a simple and effective solution deposition method for *N,N'*-1*H*,1*H*-perfluorobutyldicyanoperylene-carboxydiimide, by which they were able to overcome the drawback of uncontrolled crystallite-growth observed with methods like drop casting and spin coating (μ_n only about $0.16 \text{ cm}^2 \text{ V}^{-1} \text{ s}^{-1}$).^[29] They used the setup depicted in Figure 10a, where a substrate modified with a hydrophobic, fluorinated SAM was covered by a solution holding piece but separated at one edge by a spacer piece. First a semiconductor solution was filled into this gap and subsequent heating of the substrate led to evaporation of the solvent and growth of a highly crystalline film (see the OPM pictures in Figure 10b and c). Devices based on these films exhibited electron mobilities from 0.5 up to $1.5 \text{ cm}^2 \text{ V}^{-1} \text{ s}^{-1}$, which is indeed a remarkable improvement with regard to the non-oriented films obtained by ordinary deposition methods such as spin coating and drop casting.

Besides the herein reported procedures, a large number of other promising methods for solution deposition of organic semiconductors have been developed in recent years. These allow already, with certain limitations, large scale processing of highly ordered crystalline active layers in devices with long-term stability. Despite these advances, further research is needed to discover materials and methods that may be used in commercial applications.

2.4 Organic Semiconductor Materials based on Organic Colorants

Organic semiconductor materials which can be applied in organic TFTs have emerged as an important field of research in recent years.^[4] An overview covering the large number of organic compounds used for organic electronic applications was recently published by Zhu and co-workers.^[5] From this review it becomes evident that crucial progress has been achieved within the last years to reach the performance of a-Si:H ($\sim 1 \text{ cm}^2 \text{ V}^{-1} \text{ s}^{-1}$).^[4] Several p-type as well as n-type semiconducting materials based on small molecules have been discovered with TFT charge carrier mobilities in the range of $1 \text{ cm}^2 \text{ V}^{-1} \text{ s}^{-1}$ and a few exhibit even higher mobility. However, only p-type organic semiconductors with good performance and ambient stability are abundant, whereas the long term performance of most n-type semiconductors suffers due to the inherent instability of organic anions in the presence of oxygen and water. As a consequence, fabrication and characterization of n-channel OTFTs is often performed under inert conditions to reach the maximum possible charge carrier mobilities. Most devices degrade quickly after exposure to air; some do not even show a field-effect under ambient conditions.

Because of these limitations, a lot of scientific effort has been put into the development of ambient-stable, n-type organic semiconductors. For example, the effect of strong electron withdrawing groups on transistor performance in air has been intensively studied. Additionally, crystal engineering to prevent oxygen and water from penetrating into the active layer has also been investigated. In 2008 Shukla and co-workers from the Kodak Research Laboratories processed a n-type naphthalene diimide (NDI) derivative by vacuum sublimation, that was substituted at the *N,N'*-positions with dicyclohexyl groups.^[30] Respective devices showed electron mobilities of up to $7.5 \text{ cm}^2 \text{ V}^{-1} \text{ s}^{-1}$ under inert conditions with a decrease of the transistor performance to $6.2 \text{ cm}^2 \text{ V}^{-1} \text{ s}^{-1}$ upon exposure to air. Nevertheless, this is still one of the highest values reported for n-type organic semiconducting materials. The excellent performance can be ascribed to the crystal packing arrangement, where every molecule interacts with four neighbors due to π - π interactions leading to reticular pathways for efficient charge transport.

On the side of p-type semiconductor materials, Kang *et al.* reported in 2011 a record performance for devices based on alkyl-substituted dinaphtho[2,3-*b*:2',3'-*f*]thieno[3,2-*b*]thiophene.^[31] They found that vacuum-deposited transistors of the derivative with two *n*-decyl groups exhibited ambient stable hole mobilities as high as $8.0 \text{ cm}^2 \text{ V}^{-1} \text{ s}^{-1}$.

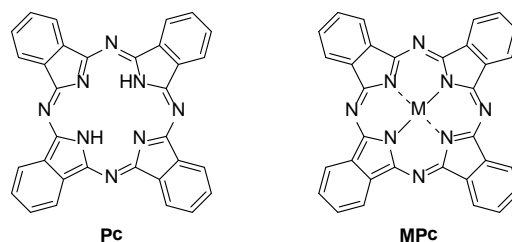
Besides small molecules, organic polymers are also of interest for application in OTFTs because of their excellent electronic properties and their solution-processability, which allows

easy deposition on various substrates such as other polymers. However, the large molecular weight and complex molecular structure hinder the formation of highly ordered (or even crystalline) structures that are desirable for efficient charge transport.^[5] Despite these drawbacks, high hole mobilities of up to $1.4 \text{ cm}^2 \text{ V}^{-1} \text{ s}^{-1}$ have been reported for a copolymer of benzothiadiazole and cyclopentadithiophene after deposition by the dip-coating method.^[32] In general, most organic polymers exhibit mobilities around $0.1 \text{ cm}^2 \text{ V}^{-1} \text{ s}^{-1}$ or lower.^[5] Polymers with n-type semiconducting properties are quite rare and typically show electron mobilities in the range of $0.01 \text{ cm}^2 \text{ V}^{-1} \text{ s}^{-1}$ or lower. One outstanding example, reported by Facchetti and coworkers, is a naphthalenedicarboximide-based copolymer with unprecedented ambient-stable OTFT performance (up to $0.85 \text{ cm}^2 \text{ V}^{-1} \text{ s}^{-1}$).^[33]

Amongst the small molecule organic semiconductors are also several representatives of the class of organic colorants. Thousands of different synthetic organic dyes have been made available in large scale by industry for the classical use of coloring of textiles, hair, paper, food and so forth. In addition, such colorants have been applied in laser printers, data storage devices, displays, biomedical sensors, solar cells and field-effect transistors.^[34] Since this thesis is focused on processing small molecule squaraine dyes as the active layer of OTFT devices, the following pages will give a review on five classes of organic colorants with respect to their capability as semiconductor materials in OFETs.

2.4.1 Phthalocyanines

In 1907, Brown and Tcherniac found by chance a synthetic pathway to phthalocyanines.^[35] They obtained the first representative of this new class of dyes as a blue solid by melting *o*-cyanobenzamide and subsequent washing with ethanol. While these researchers did not spend time on this observation, Linstead and co-workers made intensive studies on this new class of organic colorants in the early 1930s and even provided a guess for the structure of the phthalocyanines.^[36] Later, Robertson and co-workers reported crystal structures of nickel, copper, platinum and metal-free phthalocyanine and thereby confirmed the postulate that these dyes consist of four isoindole units being connected by an extended conjugated π -system and providing the possibility of metal coordination at the isoindole nitrogen atoms.^[37] The general structure of phthalocyanines is depicted in Scheme 1. A semiconducting behavior was discovered for several phthalocyanines in 1948, which still attracts interest in this class of dyes for organic electronics.^[38] Beside their application in OTFTs, metalphthalocyanines are well-known as active compounds in solar cells, optical limiters, and photoconductors.^[39]



Scheme 1. General structure of metal-free (Pc) and metal-containing phthalocyanines (MPc).

In the end of the 1980s, rare-earth phthalocyanines were used to make the first working metalphthalocyanine-based OTFTs.^[40] For this purpose, Madru *et al.* successively evaporated a thin-film of zinc phthalocyanine (ZnPc) and lutetium bisphthalocyanine (LuPc₂) on a Si wafer with a SiO₂ insulating layer.^[40a,b] After a gate voltage was applied to this bottom gate, top contact device, they observed *n*-type FET behavior with a mobility in the range of 10⁻⁴ cm² V⁻¹ s⁻¹.^[40a,b] Thin-film devices with values of up to 6 cm² V⁻¹ s⁻¹ have been realized by optimizing the deposition conditions.^[40d] Guillaud *et al.* reported that LuPc₂ and thulium bisphthalocyanine (TmPc₂) are able to act as intrinsic and extrinsic semiconductor materials, respectively.^[40e] While the transport of *n*-type charge carriers is favored in absence of air (μ_n up to 10⁻⁴ cm² V⁻¹ s⁻¹), *p*-type behavior with a mobility up to 10⁻² cm² V⁻¹ s⁻¹ has been observed after exposure to air and annealing. These changes were attributed to oxidation of the Pc semiconductor caused by the interpenetration of oxygen into the active layer. The same group established the research on thin-film transistors based on nickel phthalocyanine (NiPc) and ZnPc.^[41] By varying the film thickness they obtained μ_p values between 10⁻⁴ and 10⁻³ cm² V⁻¹ s⁻¹.

Bao and co-workers studied and optimized TFTs with copper phthalocyanine, CuPc,^[42] and other metal phthalocyanines with zinc, iron, tin, nickel, platinum, as well as the metal-free one.^[42b] By varying the substrate temperature during vacuum deposition, they were able to control the morphology of the semiconductor thin-films. It was shown by X-Ray diffraction that high temperature improves the order and crystallinity of the active layer. This trend was accompanied by an increased charge carrier mobility of the respective devices. However, for most phthalocyanine derivatives a maximum value was reached at some point followed by a decrease in μ upon further raising the temperature. This was explained by transmission electron micrographs of the respective films. For example, the crystallites of a CuPc layer (Figure 11; $\mu_p = 0.0006$ cm² V⁻¹ s⁻¹ at 30 °C) grew in size up to 125 °C (0.02 cm² V⁻¹ s⁻¹), while higher temperatures afforded thin-films with even larger crystals but showing discontinuities and gaps (0.0067 cm² V⁻¹ s⁻¹).^[42a]

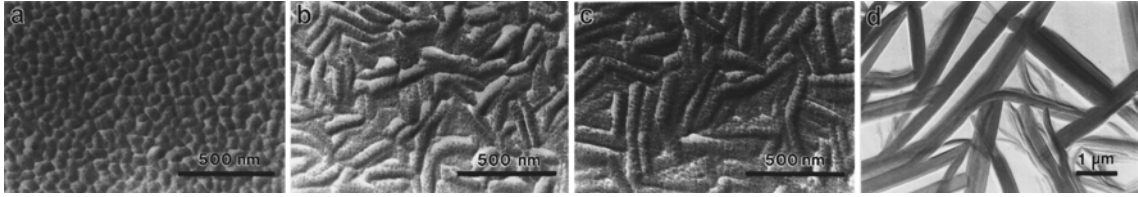


Figure 11. Transmission electron micrographs of CuPc films deposited at different substrate temperatures (a) 85 °C; (b) 125 °C; (c) 150 °C; (d) 200 °C. Reprinted with permission from ref. 42a. Copyright 1996, American Institute of Physics.

Similar observations were made for the other phthalocyanine derivatives, though the performance of the respective devices (Table 1) was depending on the nature of the metal ion and none of these compounds exceeded CuPc.^[42b] Extended storage in air didn't affect the mobility, but a slight decrease of the former I_{on}/I_{off} ratio of 4×10^5 was found.^[42a] The crystal structure of NiPc (Figure 12a) exemplifies the herringbone-like packing of the metastable α -phase in phthalocyanine thin-films,^[37a,42b] which limits the percolation pathway of the charge carriers to one dimension. Further, an edge-on orientation of the molecular planes could be proven by X-ray diffraction analysis of the semiconducting layers.^[42]

Yan and co-workers were able to improve the hole transport ability of ZnPc ($0.32 \text{ cm}^2 \text{ V}^{-1} \text{ s}^{-1}$) and CuPc films ($0.15 \text{ cm}^2 \text{ V}^{-1} \text{ s}^{-1}$) by using a weak epitaxial growth technique based on a monodomain layer of rod-like para-hexaphenyl.^[43] It is noteworthy, that these vacuum deposited devices readily reach the mobility values of single crystalline CuPc transistors (0.1 up to $1.0 \text{ cm}^2 \text{ V}^{-1} \text{ s}^{-1}$).^[44] A similar enhancement ($\mu_p = 0.11 \text{ cm}^2 \text{ V}^{-1} \text{ s}^{-1}$) was observed for a device in sandwich configuration, whose active layer consists of consecutively evaporated CuPc and CoPc films.^[45]

In recent years, remarkable improvements have been achieved in the performance of OTFTs based on titanyl (TiOPc)^[46] and vanadyl phthalocyanine (VOPc),^[47] respectively. Tada *et al.* measured under vacuum an electron mobility of $9 \times 10^{-6} \text{ cm}^2 \text{ V}^{-1} \text{ s}^{-1}$ for TiOPc devices.^[46a] After exposure to air the device switched to *p*-type operation with a μ_p value

Table 1. FET mobilities for *p*-type charge carriers in devices, whose phthalocyanine layers were vacuum-deposited at elevated substrate temperatures T_D .^[42b]

Compound	$\mu_p / 10^{-3} \text{ cm}^2 \text{ V}^{-1} \text{ s}^{-1}$		
	$T_D = 30 \text{ }^\circ\text{C}$	$T_D = 125 \text{ }^\circ\text{C}$	$T_D = 200 \text{ }^\circ\text{C}$
CuPc	0.60	20	6.7
SnPc	0.073	3.4	no field-effect
H ₂ Pc	1.3	2.6	0.00056
ZnPc	0.23	2.4	2.8
FePc	0.036	0.069	0.011
PtPc	0.15	0.15	0.090
NiPc	0.0070	0.030	0.054

of similar magnitude. Later, Hu and co-workers were able to explain the poor OFET characteristics of such devices by the amorphous and mixed-phases states of vacuum-deposited thin-films on Si/SiO₂ substrates.^[46b] They improved μ_p up to $3.31 \text{ cm}^2 \text{ V}^{-1} \text{ s}^{-1}$ by introduction of a self-assembled monolayer of octadecyltrichlorosilane (OTS), with on/off current ratios in the range of 10^7 – 10^8 . In addition, the respective devices functioned under ambient conditions for months. XRD patterns of respective thin-films revealed an edge-on orientation of the molecules. Furthermore, the excellent performance could be ascribed to a packing of the molecules similar to that in the α -phase of TiOPc single-crystals (Figure 12b).^[48] A slipped face to face packing with short intermolecular distances is representative for such non-planar phthalocyanine derivatives, which opens up the possibility for two-dimensional percolation pathways of the charge carriers. Ohta *et al.* were the first to process VOPc, which is also non-planar, in OTFTs and determined a charge carrier mobility of $\sim 5 \times 10^{-3} \text{ cm}^2 \text{ V}^{-1} \text{ s}^{-1}$.^[47a] Weak epitaxy growth of VOPc films on a highly ordered *para*-sexiphenyl layer afforded devices with μ_p values of $1.23 \text{ cm}^2 \text{ V}^{-1} \text{ s}^{-1}$.^[47b]

Similar OFET characteristics were achieved by Li, Hu and co-workers when they used OTS-modified Si/SiO₂ substrates instead of pure Si/SiO₂ substrates. The improvements were again attributed to an α -phase like growth of the thin-films.^[47c] While these *p*-channel devices exhibited long-term stability under ambient conditions, ambipolar conduction with low mobility values in the range of only 10^{-5} – $10^{-4} \text{ cm}^2 \text{ V}^{-1} \text{ s}^{-1}$ was observed under reduced pressure. Huang *et al.* perpetuated the concept of growing the VOPc layer by weak epitaxy on highly ordered crystal films, which were prepared by co-deposition from two rod-like molecules.^[47d] The quality of the VOPc thin-film as well as the OTFT behavior were shown to be dependent on the mixing ratio of the inducing layer. Respective transfer characteristics

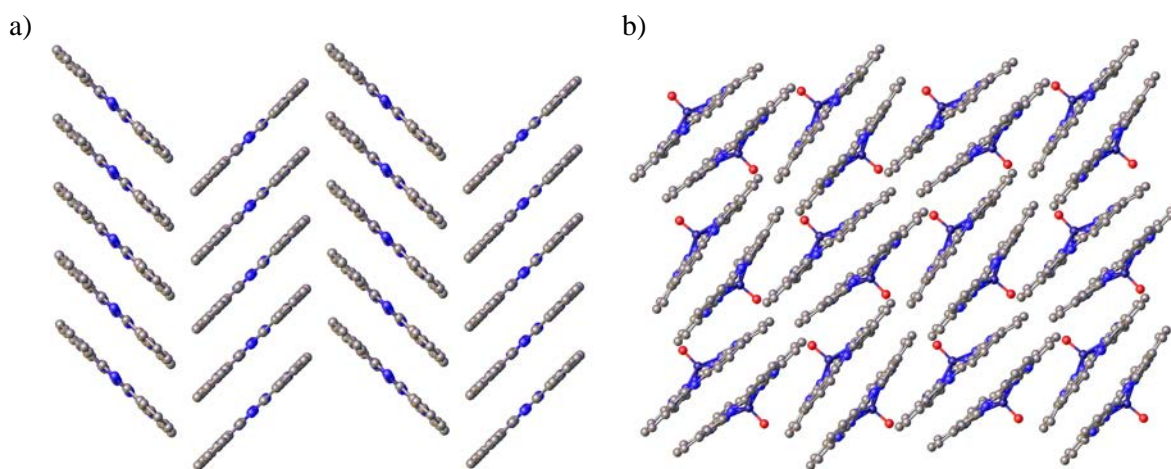


Figure 12. a) Herringbone-like packing of NiPc molecules in an α -phase single crystal^[37a] and b) slipped face to face packing of TiOPc molecules in an α -phase single crystal.^[48]

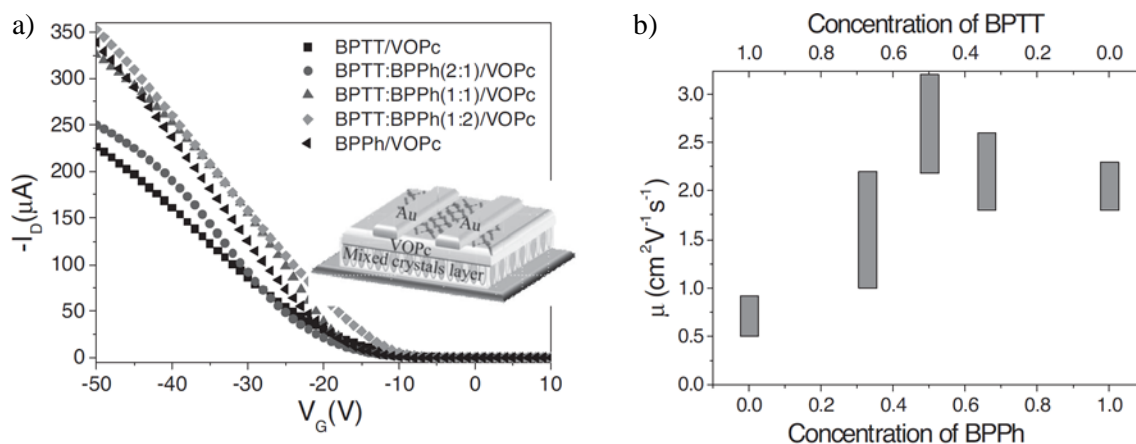
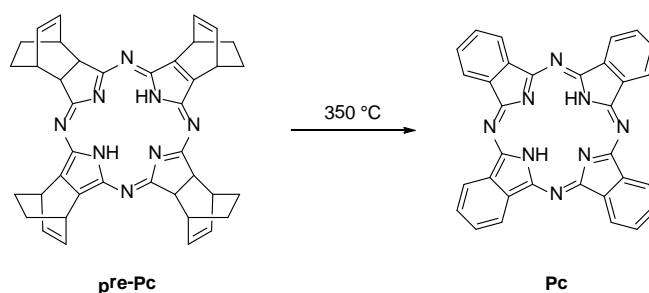


Figure 13. a) Transfer characteristics of VOPc-based transistors, which were grown by weak epitaxy on inducing layers with different mixing ratios of BPTT and BPPh. b) Dependence of the hole mobilities on the concentrations of the two molecules in the mixed crystal film. Reprinted with permission from ref. 47d. Copyright 2011, WILEY-VCH Verlag GmbH & Co. KGaA, Weinheim.

and mobility values are visualized in Figure 13, and show that the maximum performance ($\mu_{\text{h}} = 3.2 \text{ cm}^2 \text{ V}^{-1} \text{ s}^{-1}$) is reached for a 1:1 mixture.

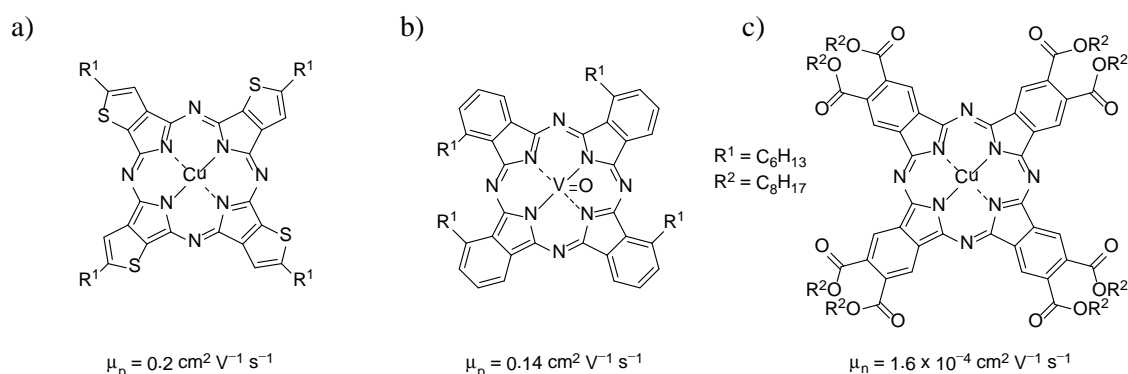
Besides this excellent *p*-channel performance, several electron deficient phthalocyanines are currently known, which provide the possibility for devices with *n*-type behavior. Bao *et al.* elucidated OTFTs based on F_{16}CuPc , F_{16}ZnPc , F_{19}CoPc , F_{16}FePc , $\text{Cl}_{16}\text{FePc}$, $(\text{CN})_8\text{CuPc}$, and PyCuPc . While the latter two could not be sublimed, the vacuum-deposited devices of the other compounds exhibited electron mobilities of up to $0.03 \text{ cm}^2 \text{ V}^{-1} \text{ s}^{-1}$ (for F_{16}CuPc), with remarkable stability after storing in air for more than half a year.^[49] Perchlorinated CuPc , $\text{Cl}_{16}\text{CuPc}$, performed even better ($0.12 \text{ cm}^2 \text{ V}^{-1} \text{ s}^{-1}$).^[50] Yan, Geng and co-workers found, that introduction of either a monolayer of OTS or *para*-sexiphenyl yields SnCl_2Pc -based, air-stable transistor devices with μ_{e} values of up to $0.30 \text{ cm}^2 \text{ V}^{-1} \text{ s}^{-1}$.^[51a] An electron mobility of $0.44 \text{ cm}^2 \text{ V}^{-1} \text{ s}^{-1}$ could be reached on using SnOPc instead of SnCl_2Pc .^[51b]

Finally, several approaches have been made over the past years to process phthalocyanine-based transistors not only by vapor deposition but also from solution. Hirao *et al.* used soluble phthalocyanine precursors for spin-coating of the semiconductor layer on Si/SiO_2 substrates.^[52a] The respective thin-films were subsequently heated at $350 \text{ }^\circ\text{C}$ for 5 min, which initiated a retro Diels-Alder reaction yielding the phthalocyanine form as active species (Scheme 2). For such devices a maximum hole mobility of $0.06 \text{ cm}^2 \text{ V}^{-1} \text{ s}^{-1}$ was determined. Fourfold substitution at the benzo-sites improves the solubility of phthalocyanines, but leads to a reduced order in the films and to four structural isomers, which hardly could be separated. Such isomeric mixtures of liquid crystalline tetraoctyl-substituted VOPc or tetraalkoxy-substituted ZnPc were applied in solution-processed OFET



Scheme 2. Retro Diels-Alder reaction, which converts the well soluble **pre-Pc** into **Pc**, which can act as the active layer in an OTFT device after thermal conversion.^[52a]

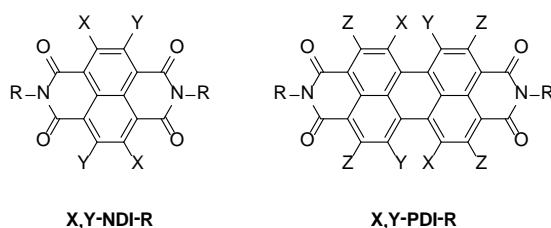
devices by Dong *et al.*^[52b] and Chaure *et al.*,^[52c] respectively. They obtained highly ordered films via thermal annealing in the liquid crystalline state, which exhibited moderate performance ($\mu_{\text{h}} = 0.017 \text{ cm}^2 \text{ V}^{-1} \text{ s}^{-1}$ for the VOPc derivative). Although the isomers of 5-hexylthiophene-fused porphyrazines (see Scheme 3a) could also not be separated, μ_{h} for TFTs based on the isomeric mixture rose to a value of $0.2 \text{ cm}^2 \text{ V}^{-1} \text{ s}^{-1}$.^[52d] In contrast, for non-peripheral tetrahexyl-substituted VOPc (see Scheme 3b) four structural isomers were easily separated by column chromatography.^[52e] The molecules in a thin-film of the isomer with the highest mobility ($0.13 \text{ cm}^2 \text{ V}^{-1} \text{ s}^{-1}$) adopt a similar packing arrangement as was found for films of unsubstituted VOPc. Ma *et al.* recently reported the first solution-processable n-type CuPc-based transistor devices.^[53] The attachment of electron-withdrawing octyloxycarbonyl groups to the phthalocyanine periphery (see Scheme 3c) causes self-assembly into one-dimensional nanostructures in binary solvent mixtures. TFTs prepared from such solutions exhibited low electron mobilities of $1.6 \times 10^{-4} \text{ cm}^2 \text{ V}^{-1} \text{ s}^{-1}$ under a dry nitrogen atmosphere.



Scheme 3. Phthalocyanine derivatives, which were used for OFET fabrication from solution (the mobility is denoted beyond the structures): a) One out of four structural isomers of a 5-hexylthiophene-fused porphyrazine;^[52d] b) a tetrahexyl-substituted VOPc isomer;^[52e] c) Solution-processable CuPc derivative with n-type behavior.^[53]

2.4.2 Arylene Diimides

Similar to phthalocyanines, the large π -systems of arylene diimides are an encouraging feature for efficient charge transport due to the possibility for π - π -stacking. In addition, low-lying LUMO levels and their reversible redox behavior make them promising candidates for application as n-type semiconductors in OTFT devices with enhanced ambient stability. Already in 1995 the group of Dodabalapur *et al.*^[54a] published electron mobilities up to $0.001 \text{ cm}^2 \text{ V}^{-1} \text{ s}^{-1}$ for 3,4,9,10-perylenetetracarboxylic dianhydride (PDA) and one year later Horowitz *et al.*^[54b] reported on the first 3,4,9,10-perylenetetracarboxylic diimide (PDI)-based devices (for the general structure of PDI see Scheme 4). At the same time, Katz, Dodabalapur and co-workers found n-type behavior for the smaller homologue 1,4:5,8-naphthalenetetracarboxylic dianhydride (NDA) with μ_e values up to $0.003 \text{ cm}^2 \text{ V}^{-1} \text{ s}^{-1}$. For **H,H-NDI-H** they observed one order of magnitude lower values ($\sim 10^{-4} \text{ cm}^2 \text{ V}^{-1} \text{ s}^{-1}$) (for the general structure of 1,4:5,8-naphthalenetetracarboxylic diimides (NDIs) see Scheme 4).^[55]



Scheme 4. General structures of naphthalene (**X,Y-NDI-R**) and perylene tetracarboxylic diimide (**X,Y-PDI-R**), where X, Y and Z represent the substituents at the aromatic scaffold and R those attached at the N,N' -positions.

Ambient operational stability of NDI and PDI based transistor devices was achieved by two principal concepts: One is to create closely packed transistor films by attaching (per)fluorinated substituents at the N,N' -positions, while the second concerns the lowering of the LUMO energies by incorporation of electron-withdrawing groups at the aromatic core. To test the former concept, Katz *et al.* varied the degree of fluorination at the imide substituents of H,H-NDI. While an *n*-octyl group gave almost no field effect in air,^[56a] devices based on **H,H-NDI-CH₂C₇F₁₅** led to improved air stability with an electron mobility of 0.05 – $0.1 \text{ cm}^2 \text{ V}^{-1} \text{ s}^{-1}$ under ambient conditions.^[56a-c] One possible explanation for the enhanced stability of such transistor materials is the denser packing of fluorinated alkyl chains compared to that of non-fluorinated ones, which prevents water and oxygen from penetrating into the central NDI core.^[57] Similar results were found for a series of H,H-NDIs with *p*-alkylbenzyl substituents at the N,N' -positions.^[56a,d] Devices based on the methyl derivative exhibited a mobility of only $10^{-6} \text{ cm}^2 \text{ V}^{-1} \text{ s}^{-1}$ in air, while replacement with a CF₃ group led to

a maximum value of $0.12 \text{ cm}^2 \text{ V}^{-1} \text{ s}^{-1}$.^[56a] Finally, substitution with $\text{CH}_2\text{CH}_2\text{C}_8\text{F}_{17}$ further enhanced performance at ambient conditions ($\mu_e = 0.57 \text{ cm}^2 \text{ V}^{-1} \text{ s}^{-1}$).^[56d]

Following the second concept, the attachment of electron-withdrawing groups helps to adjust the LUMO levels of NDIs (Figure 14, right), so that their radical anions and also the respective OTFTs are no longer susceptible to reaction with water (below $E_{1/2} = -1.14 \text{ V}$; vs. Fc/Fc^+).^[58] In 2007 Jones *et al.* reported on the dicyanated derivative **CN,H-NDI-C₈H₁₇**.^[59] Application in vacuum-processed OTFTs yielded ambient-stable electron mobilities of $0.11 \text{ cm}^2 \text{ V}^{-1} \text{ s}^{-1}$. Both concepts were combined by Bao, Würthner and co-workers, when they carried out the synthesis of core-chlorinated NDIs with fluoroalkyl substituents at the *N,N'*-positions.^[27c,27d,60] Dichlorinated **Cl,H-NDIs** exhibited better air-stability than the tetrachlorinated counterparts, despite the lower LUMO energies of **Cl,Cl-NDIs**. This fact was explained by a higher packing density of the fluoroalkyl chains for the former. Eventually, OTFTs of **Cl,H-NDI-CH₂C₃F₇** with maximum $\mu_e = 1.43 \text{ cm}^2 \text{ V}^{-1} \text{ s}^{-1}$ were obtained after surface treatment with SAM.

Similar progress for ambient stable OTFTs based on PDI derivatives has been made in the last decade. In 2002, Malenfant *et al.* reported on core-unsubstituted **H,H-PDI-C₈H₁₇** as organic semiconductor material.^[61a] While n-type transistor operation ceased rapidly on exposure to air, under ambient conditions $\mu_e = 0.6 \text{ cm}^2 \text{ V}^{-1} \text{ s}^{-1}$ was measured. By optimization of the processing conditions for this derivative^[61b] and switching to **H,H-PDI-C₁₃H₂₇** with an even longer alkyl chain^[61c] the performance could be raised to $2.1 \text{ cm}^2 \text{ V}^{-1} \text{ s}^{-1}$, but only under

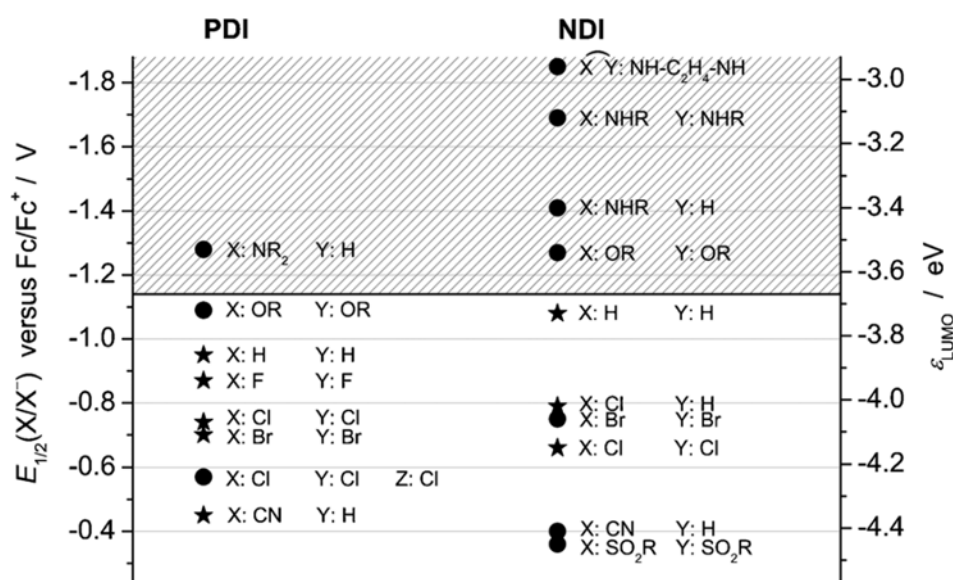


Figure 14. First reduction potentials $E_{1/2}(X/X^-)$ and respective LUMO energies for known PDI and NDI derivatives. Water reduction can occur in the hatched area.^[58] Reproduced by permission of The Royal Society of Chemistry.

non-ambient conditions. The groups of Bao and Würthner showed in 2009, that introduction of fluoroalkyl chains at the N,N' -positions of the parent core-unsubstituted PDI yields air-stable devices with mobilities of up to $1.18 \text{ cm}^2 \text{ V}^{-1} \text{ s}^{-1}$ in air and $1.42 \text{ cm}^2 \text{ V}^{-1} \text{ s}^{-1}$ in N_2 atmosphere (both for **H,H-PDI-CH₂C₃F₇**).^[62]

While core-cyanation and non-fluorinated imide substituents resulted in OTFTs with poor operation at ambient conditions (μ_e up to $0.12 \text{ cm}^2 \text{ V}^{-1} \text{ s}^{-1}$),^[63a] an improved value of up to $0.64 \text{ cm}^2 \text{ V}^{-1} \text{ s}^{-1}$ could be achieved for **CN,H-PDI-C₈F₁₇** by the Northwestern group.^[63a,b] Besides lowering the LUMO energy, electron-withdrawing groups at the PDI bay positions affect the packing in the crystal structure due to their bulkiness. The trade-off between these two effects was studied by Schmidt *et al.* for a series of core-halogenated PDI derivatives with fluorinated alkyl chains at the N,N' -positions.^[62] Analysis of the crystal packing of **H,H-PDI-CH₂C₃F₇** revealed an intermolecular π - π overlap of about 50 % for the nearly planar π -cores in a slip-stacked arrangement (see Figure 15), whereas the difluorinated derivative exhibited a herringbone like pattern along with a slightly twisted perylene core ($\sim 3.0^\circ$). Thereby, the face-to-face overlap of **F,H-PDI-CH₂C₃F₇** was found to be less than 5 %. Further substitution with two additional fluorine atoms increased the torsion angles (19.8° and 25.1° , respectively) resulting in negligible π - π contacts. These findings were also reflected by the results of respective OTFT devices: While the perfect packing of **H,H-PDI-CH₂C₃F₇** gives ambient-stable charge carrier mobilities of up to $1.18 \text{ cm}^2 \text{ V}^{-1} \text{ s}^{-1}$, a dramatic decrease is found by increasing number and size of the electron-withdrawing substituents (**F,H-PDI-CH₂C₃F₇**: $0.58 \text{ cm}^2 \text{ V}^{-1} \text{ s}^{-1}$; **F,F-PDI-CH₂C₃F₇**: $0.05 \text{ cm}^2 \text{ V}^{-1} \text{ s}^{-1}$), which compromise the solid state packing. For tetrachlorinated and tetrabrominated PDI derivatives

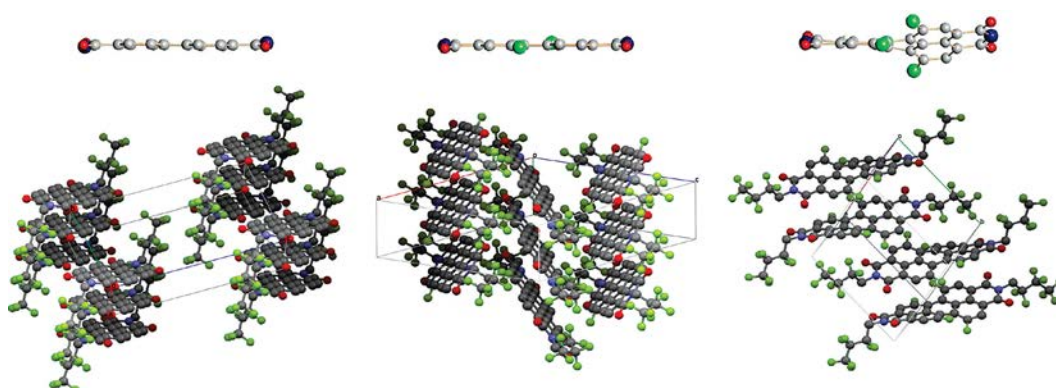


Figure 15. Side view on the perylene core of **H,H-PDI-CH₂C₃F₇**, **F,H-PDI-CH₂C₃F₇**, and **F,F-PDI-CH₂C₃F₇** (top, from left to right), which clarifies the increase of the twist-angle with the number of substituents in the bay-region. Slip-stacked face-to-face packing in the crystal structure of **H,H-PDI-CH₂C₃F₇**, herringbone structure of **F,H-PDI-CH₂C₃F₇** and packing motif of the twisted **F,F-PDI-CH₂C₃F₇** are depicted at the bottom (from left to right). Reprinted with permission from ref. 62. Copyright 2009, American Chemical Society.

with an even higher degree of twisting (torsion angles $\sim 35\text{--}37^\circ$) only poor transistor performances were observed ($\mu_e \sim 10^{-5} \text{ cm}^2 \text{ V}^{-1} \text{ s}^{-1}$). In 2010, the same authors managed to overcome the packing problems associated with core-distortion by a crystal engineering strategy.^[64] Full core-chlorination accounted for a quite low LUMO level of -4.23 eV and for a strongly twisted perylene core. However, free NH imide groups enable formation of hydrogen bonds, which lead together with close $\pi\text{-}\pi$ contacts to a brick stone arrangement. Thus, the possibility for two-dimensional charge transport is given and an electron mobility of $0.82 \text{ cm}^2 \text{ V}^{-1} \text{ s}^{-1}$ in air was measured. The so far known highest mobility for PDI transistors in air (up to $3 \text{ cm}^2 \text{ V}^{-1} \text{ s}^{-1}$) was reported by Molinari *et al.* for devices from single-crystals of **CN,H-PDI-CH₂C₃F₇**.^[65]

Whilst the performances obtained for devices based on vacuum deposited thin-films and single-crystals are of high importance from the scientific point of view, solution processing of NDI and PDI materials is of great interest for cheap and large scale manufacturing. Facchetti and co-workers were able to obtain an ambient stable mobility of up to $0.01\text{--}0.06 \text{ cm}^2 \text{ V}^{-1} \text{ s}^{-1}$ for **CN,H-PDI-C₈H₁₇** using inkjet printing^[66a,c] and drop casting methods,^[66b] respectively. It was shown by the same groups in 2009, that again introduction of fluorinated alkyl chains at the *N,N'*-positions was an effective remedy for enhanced performance of solution-processed OTFTs in air.^[23,67] Spin-coating of **CN,H-PDI-CH₂C₃F₇** from CHCl_3 solution and subsequent thermal annealing of the thin-film gave rise to an electron mobility of $0.133 \text{ cm}^2 \text{ V}^{-1} \text{ s}^{-1}$. Recently, even higher values were presented for NDI-derivatives: Gao *et al.* introduced a new concept for π -core expansion and thereby achieved mobilities of up to $0.51 \text{ cm}^2 \text{ V}^{-1} \text{ s}^{-1}$ in air by spin-coating of a NDI fused with 2-(1,3-dithiol-2-ylidene)malonitrile,^[21] while Bao, Würthner and co-workers used the method of solution shearing to obtain large arrays of **Cl,H-NDI-CH₂C₃F₇** (see Figure 16a).^[27c,68] When processed on PTS-treated Si/SiO₂ substrates, a maximum μ_e of 0.22 and $0.57 \text{ cm}^2 \text{ V}^{-1} \text{ s}^{-1}$ could be recorded for devices oriented parallel and perpendicular, respectively, with regard to the shearing direction.^[27c] Besides an improvement of the ambient OFET characteristics (up to $0.95 \text{ cm}^2 \text{ V}^{-1} \text{ s}^{-1}$ for perpendicular orientation), Stolte *et al.* observed a rather unprecedented behavior under bias stress, namely an unexpected increase of the electron mobility up to $4.26 \text{ cm}^2 \text{ V}^{-1} \text{ s}^{-1}$ on continuous recording of the transfer characteristics on bare Si/SiO₂ substrates (see Figure 16b).^[68]

Recently, Würthner and Klauk reported the first NDI derivative, which acts as a p-channel semiconductor.^[69] Lateral extension of the NDI core by electron-rich carbazole rings and bulky imide substituents result in a p-type semiconducting axis, which is orthogonal to

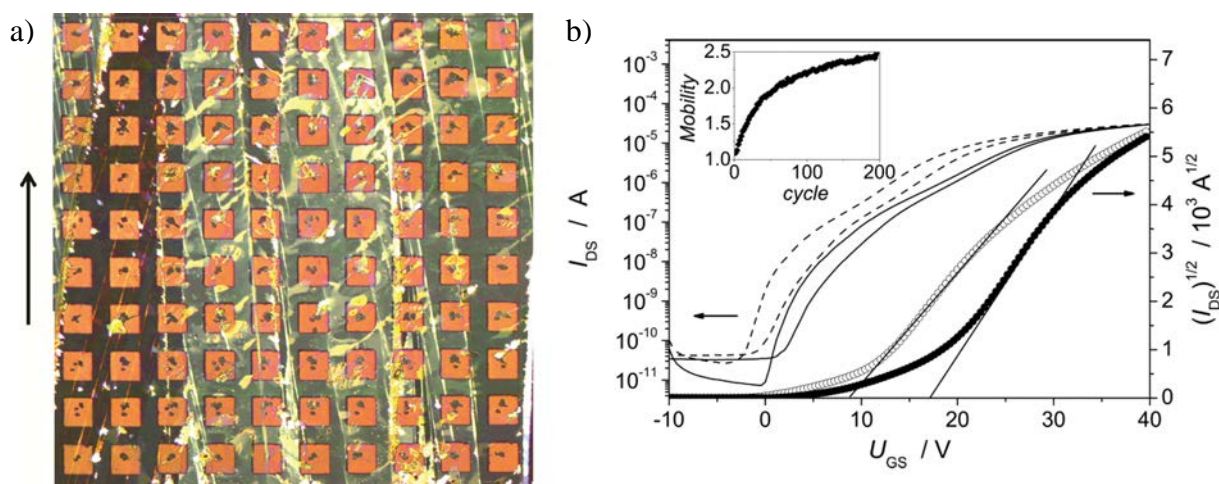


Figure 16. a) Optical microscopic image of a thin-film with source and drain gold contacts. The film was processed by solution shearing of **Cl,H-NDI-CH₂C₃F₇** from o-DCB. The direction of shearing is indicated by the arrow, whose lengths equals to 1 mm. Charge carrier mobility of individual devices is color coded in the area of the OTFT channel b) Transfer characteristics of a solution-sheared NDI transistor in perpendicular orientation with respect to the shearing direction before (open circles, dotted lines) and after (filled circles, solid lines) 200 times of measuring the transfer characteristics. The inset displays the evolution of the electron mobility during this measurement.^[68b] Reproduced by permission of the PCCP Owner Societies.

the electron deficient N-N axis (see Figure 17). Localization of the HOMO along the expanded π -cores (Figure 17c) accompanied by stacking in this direction facilitates transport of holes and hence a large mobility of $0.56 \text{ cm}^2 \text{ V}^{-1} \text{ s}^{-1}$ was measured for this NDI-derivative in air.

By using terrylene and quaterrylene diimides n-type OFET performance under ambient conditions was not improved despite their further enlarged π -systems. The former are known to show charge carrier mobilities of $0.07 \text{ cm}^2 \text{ V}^{-1} \text{ s}^{-1}$ under inert atmosphere,^[70a,b] whereupon for the latter a solution processable derivative with reasonable air-stability ($\mu_e = 0.088 \text{ cm}^2 \text{ V}^{-1} \text{ s}^{-1}$) has been reported by Bao and co-workers recently.^[70c]

Significant advances in the application of NDI and PDI in OTFT devices has been

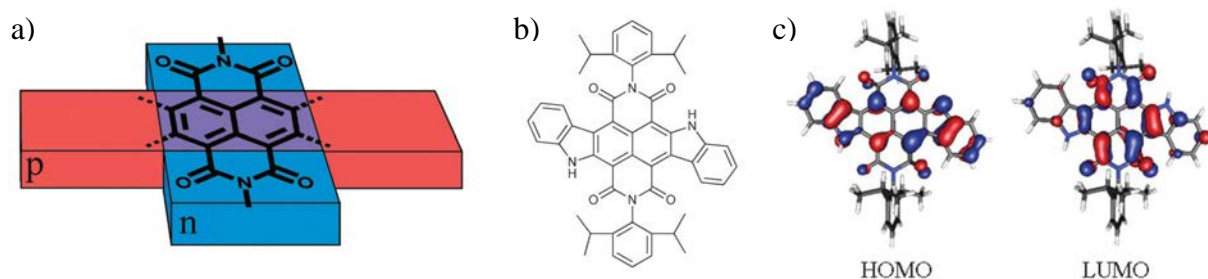


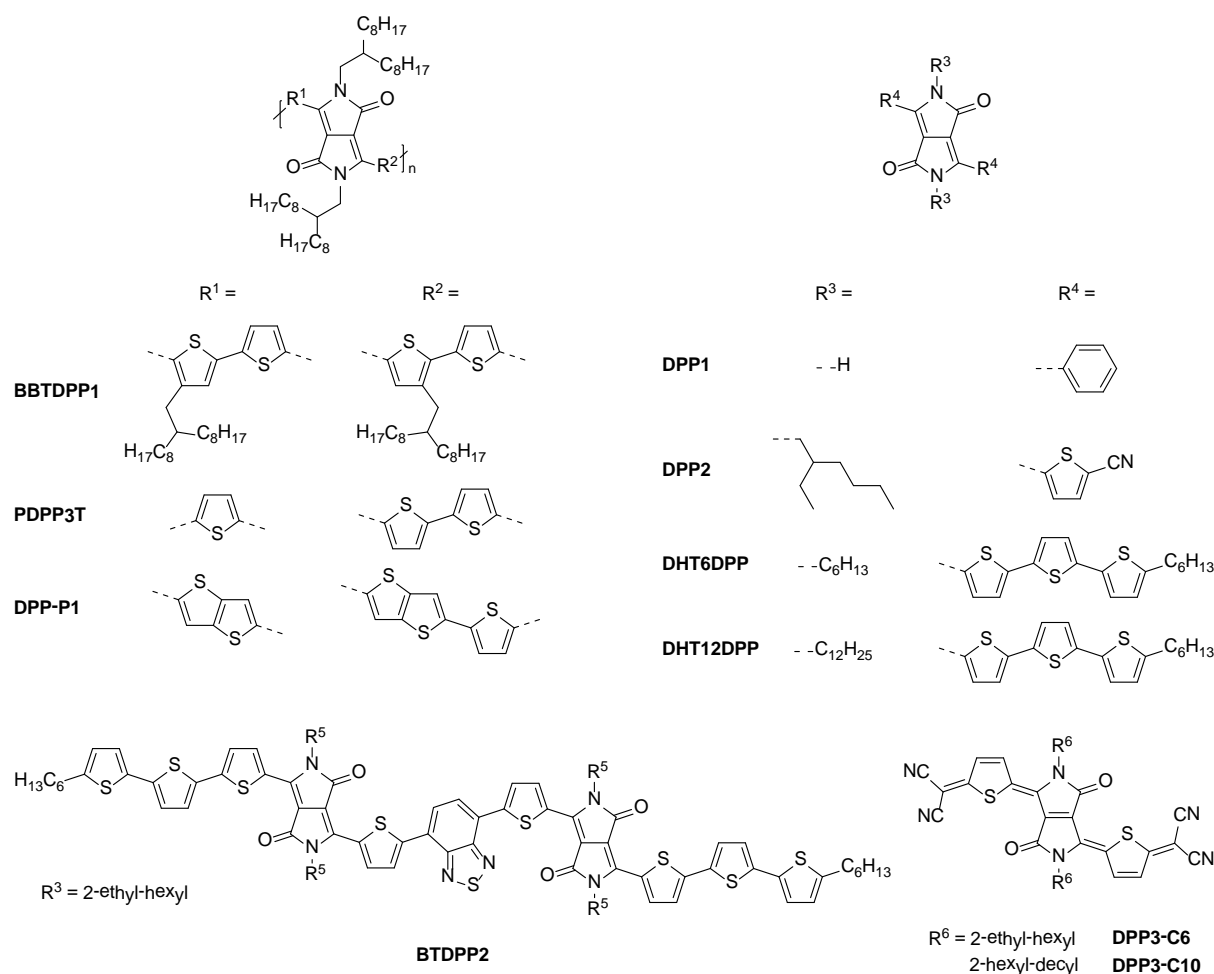
Figure 17. a) Schematic depiction of the p- and n-type semiconducting axis of the π -expanded NDI. b) Structural formula of this NDI. c) HOMO (left) and LUMO (right) of this NDI, which were obtained by DFT (B3-LYP) calculations.^[69] Reproduced by permission of The Royal Society of Chemistry.

achieved over the last few years. Ambient stable electron mobilities of $1.0 \text{ cm}^2 \text{ V}^{-1} \text{ s}^{-1}$ and higher have been obtained for solution- as well as vacuum-deposited devices based on NDI and PDI semiconductors. Unexpectedly, recent work has also shown that NDIs may be tuned to exhibit p-type charge transport.

2.4.3 Diketopyrrolopyrroles

Polymers based on diketopyrrolopyrrole (DPP) have been known since the early 1990s^[71] and monomeric DPPs represent a class of organic colorants that has been established for more than 30 years. Although they are employed in large scale commercial application (e.g. Pigment Red 254),^[72] until recently little effort has been spent on their application in organic electronics.

In 2008, Turbiez, Winnewisser and co-workers reported the first DPP-containing polymer **BBTDPP1** for OTFTs (see Scheme 5).^[73] They observed ambipolar charge transport with hole mobilities of up to $0.1 \text{ cm}^2 \text{ V}^{-1} \text{ s}^{-1}$ and electron mobilities of up to $0.09 \text{ cm}^2 \text{ V}^{-1} \text{ s}^{-1}$ for thin-films on OTS-modified Si/SiO₂ substrates with barium top-contact electrodes. Operation



Scheme 5. Structures of polymeric and small molecule DPP dyes used in organic electronics.

of these transistors under appropriate bias conditions led to emission of near-infrared light.^[73] Bijleveld *et al.* developed the polymer **PDPP3T** (see Scheme 5), which exhibited slightly lower mobilities for both types of charge carriers, and was additionally applied in photovoltaic cells as a donor, reaching a power conversion efficiency of 4.7 %.^[74] During the last two years, several new solution-processable DPP polymers, which mainly differ in the kind of linkage, have been developed. Ambipolar charge carrier mobilities between 0.3 and $1.0 \text{ cm}^2 \text{ V}^{-1} \text{ s}^{-1}$ (inert conditions) were measured for these derivatives, some of which were also successfully used as donor materials in organic solar cells with quite high power conversion efficiencies of up to ~5 %.^[75] Bronstein and co-workers spin-coated thin-films of their polymer **DPP-P1** (see Scheme 5) from solutions in chlorobenzene and observed a maximum hole mobility of $1.95 \text{ cm}^2 \text{ V}^{-1} \text{ s}^{-1}$ for transistors in top-gate, bottom-contact configuration.^[76] Despite this remarkable p-type performance, electron transport and therefore ambipolar operation was still present in these devices, although only a μ_e value of $0.03 \text{ cm}^2 \text{ V}^{-1} \text{ s}^{-1}$ was determined. Blends of this polymer and PC₇₁BM in a 1:2 ratio were shown to operate in organic photovoltaic devices with a power conversion efficiency of 5.4 %.

Compared with the significant recent activity in DPP polymers less activity has been devoted to small molecule DPP-based organic electronics. Yanagisawa *et al.* reported in 2008 on transistors with their active layer deposited by vacuum sublimation of unsubstituted **DPP1** and spin-coating of the *t*-Boc derivative of **DPP1** as a soluble precursor (see Scheme 5) with subsequent cleavage into the parent pigment on annealing at about 200 °C.^[77] Both ways of preparation yielded devices with hole mobilities in the range of $10^{-5} \text{ cm}^2 \text{ V}^{-1} \text{ s}^{-1}$. Functionalization of DPP with alkyl-substituted terthiophenes opened up the possibility for solution-processing of **DHT6DPP** (see Scheme 5) semiconductor films with decent field effect mobilities (up to $0.02 \text{ cm}^2 \text{ V}^{-1} \text{ s}^{-1}$ after annealing) superseding additional cleaving procedures.^[78] For these DPP derivatives it never has been clarified to what extent the hole transport is governed by the oligothiophene subunits, which are well-known building blocks for p-type semiconductors. However, Würthner, Klauk and co-workers presented in 2011 the pristine derivative **DPP2** (see Scheme 5).^[79] Vacuum-deposited devices on FOPA-modified Si/SiO₂/AlO_x substrates exhibited remarkable hole mobility of up to $0.7 \text{ cm}^2 \text{ V}^{-1} \text{ s}^{-1}$ despite the small size of the conjugated π -system, a huge coverage of space by the electronically inactive alkyl chains, and the mixture of **DPP2** diastereomers being present in the active

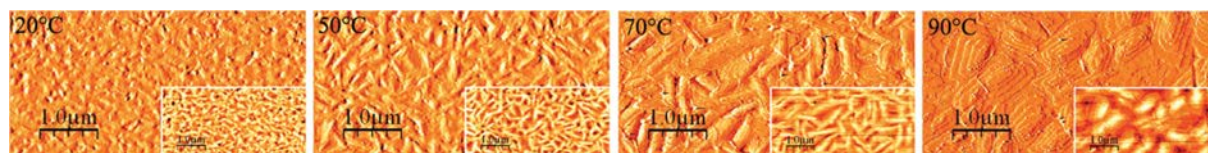


Figure 18. AFM amplitude and topography (inset) images of **DPP2** thin-films, which were deposited by vacuum sublimation at different substrate temperatures.^[79] Reproduced by permission of The Royal Society of Chemistry.

layer. The optimum in OFET performance at a substrate temperature of 70 °C was found by variation from 20 °C up to 90 °C and subsequent study of the film morphology by AFM. Increasing mobility could be explained by the formation of larger grains accompanied by a decrease of the number of grain boundaries (see Figure 18).

Very recently, Nguyen and co-workers reported balanced field-effect mobilities of up to $0.01 \text{ cm}^2 \text{ V}^{-1} \text{ s}^{-1}$ for ambipolar transistors, which were fabricated from solutions of **BTDP2** (see Scheme 5) by spin-coating.^[80] Qiao *et al.* managed to obtain the DPP derivatives **DPP3-C6** and **DPP3-C10** (see Scheme 5) exhibiting quite low LUMO levels at about -4.51 eV .^[81] Ambient stable n-type OTFTs with electron mobilities of up to $0.55 \text{ cm}^2 \text{ V}^{-1} \text{ s}^{-1}$ for **DPP3-C6** and $0.35 \text{ cm}^2 \text{ V}^{-1} \text{ s}^{-1}$ for **DPP3-C10** could be processed by vacuum deposition and spin-coating, respectively. While the air-stability of these devices may be explained by the energetically low LUMO, the efficient charge transport was attributed to a favorable packing in the crystal structure of **DPP3-C6** (see Figure 19). The interdigitation of the alkyl chains, a columnar π -stacking structure in a slipped face-to-face arrangement, and intermolecular hydrogen bonds seem to favor the formation of percolation pathways for the charge carriers.

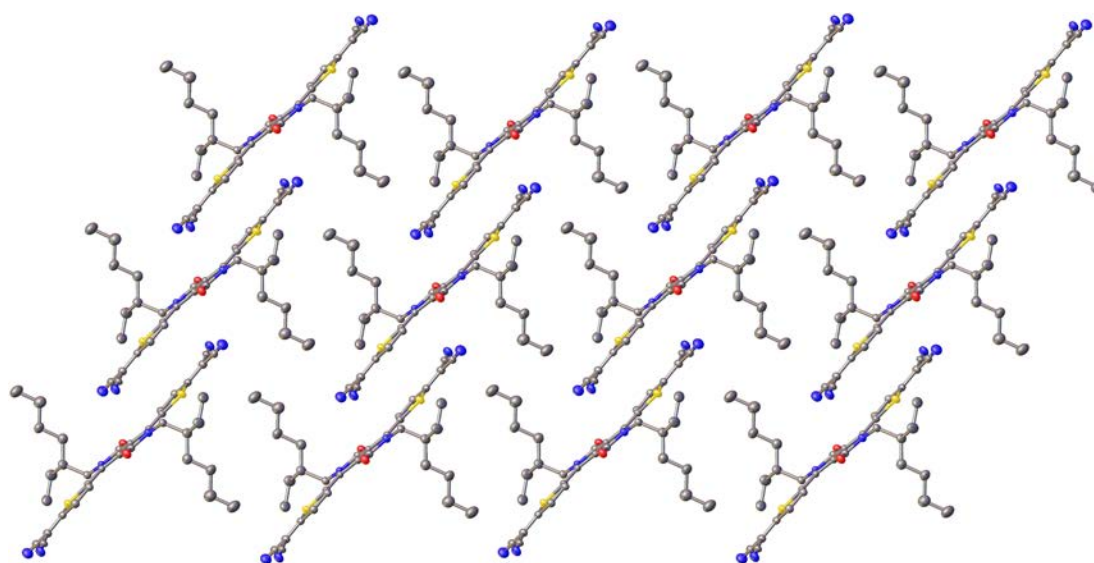
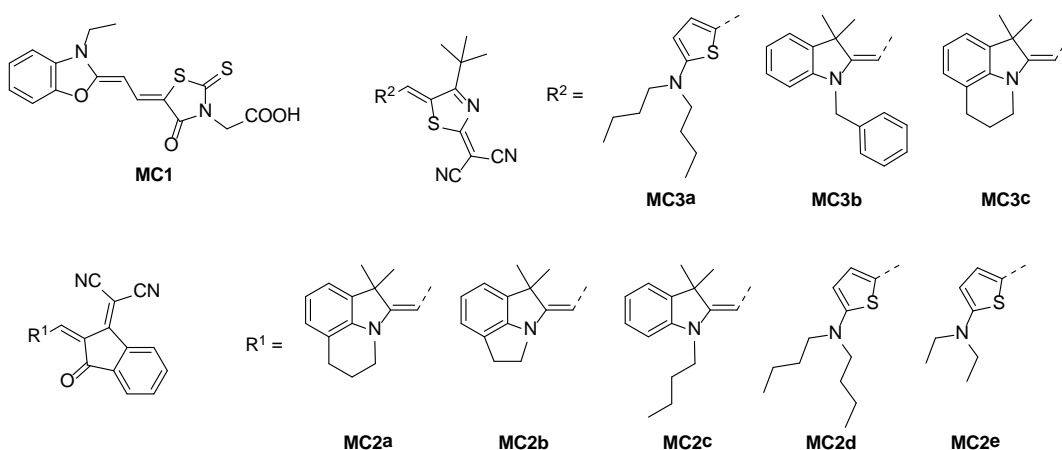


Figure 19. Packing motif of molecules in the crystal structure of **DPP3-C6**.^[81]

2.4.4 Merocyanines

Merocyanine (MC) dyes are composed of an electron-donor and electron-acceptor unit interlinked by a π -conjugated polymethine chain and therefore belong to the class of polymethine dyes. Their optical properties can be tuned by changing the number of “-CH=” units in the methine bridge as well as by varying the strength of the donor and acceptor groups.^[82] These well-established donor-acceptor colorants were successfully applied in the field of nonlinear optics more than a decade ago. In addition, they have been used as spectral sensitizers in photography and as markers in biological and medicinal applications.^[83] More recently, merocyanines have been proven to be a potent alternative to the ruthenium sensitizers used in dye-sensitized solar cells.^[84]

Already in 1984, Kudo and co-workers reported on merocyanine-based organic transistor devices. However, the mobilities were quite low with a highest value for vacuum-deposited TFTs of **MC1** (see Scheme 6) of $5.0 \times 10^{-5} \text{ cm}^2 \text{ V}^{-1} \text{ s}^{-1}$ (p-type).^[85] The groups of Meerholz and Würthner introduced merocyanines as p-type hole-conducting components in bulk heterojunction (BHJ) solar cells in 2008.^[86,87a] Besides the characteristic power-conversion efficiencies (PCE) of respective organic photovoltaic devices (up to 6.1 % for vacuum-deposited **MC2a** in combination with C_{60} fullerene,^[87d] see Scheme 6), only poor charge carrier mobilities were determined for the dyes with the highest PCEs from solution-processed OTFTs of the pristine colorants.^[87] Table 2 highlights the performance of transistors and solar cells based on various merocyanines and shows maximum hole mobilities of up to $4 \times 10^{-4} \text{ cm}^2 \text{ V}^{-1} \text{ s}^{-1}$ (for **MC3a**,^[87e] see Scheme 6). These data acquired for amorphous films suggest, contrary to conventional knowledge,^[12d,16] that large ground-state dipole moments do not necessarily impede the charge transport in organic semiconductor materials.



Scheme 6. Structures of merocyanine dyes used in organic electronics.

Table 2. Hole mobilities of TFTs based on spin-coated films of the pristine merocyanine and power conversion efficiencies of BHJ solar cells consisting of merocyanine:PCBM blends.

Compound	$\mu_p / 10^{-5} \text{ cm}^2 \text{ V}^{-1} \text{ s}^{-1}$	PCE / %	Literature
MC2a	5	2.6 / 6.1 ^[a]	[87b] / [87d]
MC2b	3	1.4	[87b]
MC2c	1	1.5	[87b]
MC2d	1	2.3	[87e]
MC2e	0.7	3.0	[87e]
MC3a	40	1.1	[87e]
MC3b	~0.1	2.7	[87c]

^[a] Determined for a merocyanine:C₆₀ blend.

Further evidence for charge transport through highly dipolar molecules was provided by the just published results of the Würthner group.^[88] They reported transistor devices of the highly dipolar ($\mu_g = 13.6 \text{ D}$) merocyanine dye **MC3c** (see Scheme 6) by vacuum deposition with hole mobilities up to $0.18 \text{ cm}^2 \text{ V}^{-1} \text{ s}^{-1}$ on TPA-modified substrate. Investigation of the film morphology by AFM revealed quite large ($0.5 - 1 \mu\text{m}$), random stripe-like crystals on SAM-modified substrates (see Figure 20). In contrast, amorphous disordered films were observed after deposition on bare Si/SiO₂ substrates leading to lower mobilities. X-ray diffraction of the thin-films on TPA substrates as well as SAED experiments indicated the formation of highly crystalline films. Taking into account the *d*-spacing values from the XRD measurements as well as the J-type excitonic coupling derived from UV/Vis data, extended π -stacks with a slipped packing arrangement can be assumed. With the additional information that highly dipolar merocyanines adopt an antiparallel packing arrangement, the authors derived a structural model which is depicted in Figure 20. As the merocyanine exhibits molecular layers that lack bipolarity, the drawbacks of highly polar molecules are overcome

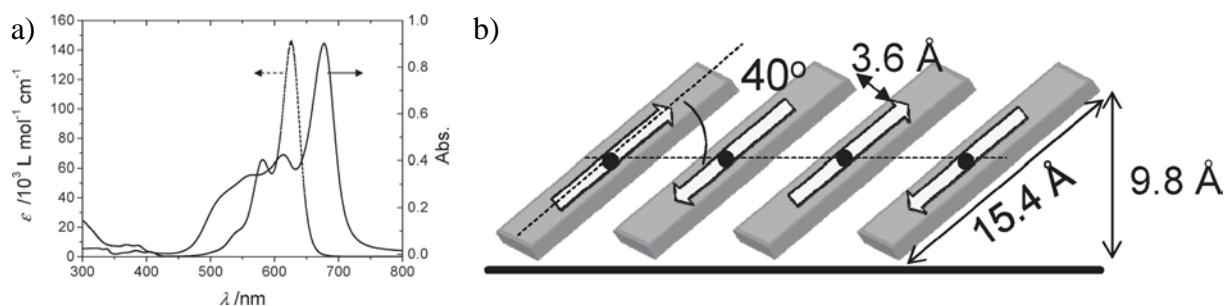
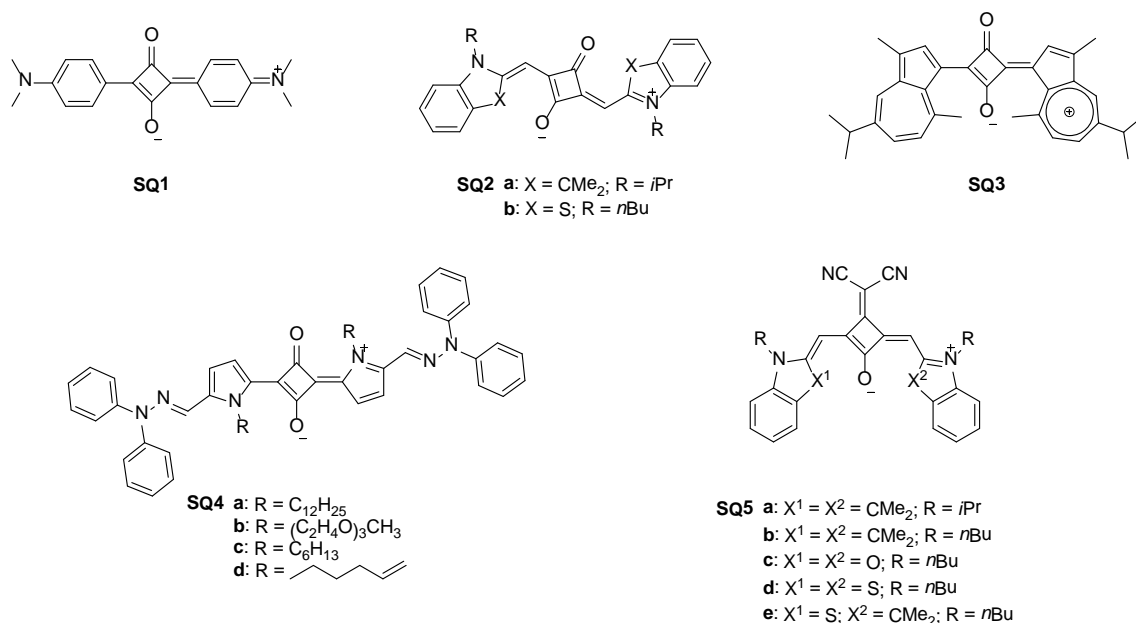


Figure 20. a) UV/Vis spectra of merocyanine **MC3c** in methylene chloride solution (dashed line) and thin-films on TPA substrate (solid line). b) Structural model for the packing arrangement in these films, where the arrows depict the orientation of the dipole moment. Reprinted with permission from ref. 88. Copyright 2012, WILEY-VCH Verlag GmbH & Co. KGaA, Weinheim.

on a supramolecular level,^[86] and one can assume that the dipole moment may even be the driving force for the desirable dense packing. Therefore, efficient charge transport may even be facilitated by such dipoles in centrosymmetric crystalline packing arrangements.

2.4.5 Squaraines

Currently, very little is known about squaraine dyes and their application in OFETs, although this class of colorants has been widely studied for a range of applications, for instance in bio-imaging probes, for photo dynamic therapy, in nonlinear optics and as photoconductors in recent years.^[89] Moreover, Thompson, Forrest and co-workers successfully applied squaraines in organic photovoltaics and could achieve PCEs up to 5.9 %, but did not study the charge carrier mobilities of these dyes.^[90] Pagani, Marks, Facchetti and co-workers reported also on organic solar cells based on squaraine derivatives (**SQ4c-d**, see Scheme 7) with PCEs up to 2 %. They also studied TFT devices of these compounds and found moderate hole mobilities in the range of $10^{-4} \text{ cm}^2 \text{ V}^{-1} \text{ s}^{-1}$.^[91] Similar values were reported earlier for squaraines, which were designed for NIR light-emitting ambipolar organic field-effect transistors (**SQ3**),^[92] near infrared (NIR) detectors (**SQ4a-b**)^[93] and nanowire transistors (**SQ1**).^[94] OTFTs with hole mobilities in the region of $10^{-3} \text{ cm}^2 \text{ V}^{-1} \text{ s}^{-1}$ were obtained for the first two cases by spin-coating, while in the latter, well-aligned and single crystalline squaraine nanowires (for SEM and TEM images see Figure 21) were used as the active layer of transistor devices ($\mu_h = 2.8 \times 10^{-4} \text{ cm}^2 \text{ V}^{-1} \text{ s}^{-1}$).



Scheme 7. Structures of squaraine dyes used in organic electronics.

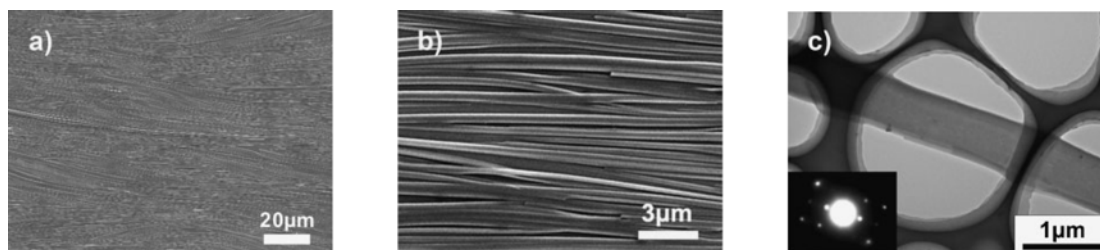


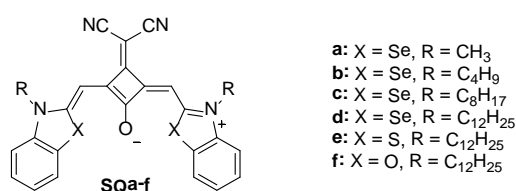
Figure 21. a), b) SEM images of a **SQ1** nanowire film at different magnifications. c) TEM image of one squaraine nanowire with the respective electron-diffraction pattern (inset). Reprinted with permission from ref. 94. Copyright 2009, WILEY-VCH Verlag GmbH & Co. KGaA, Weinheim.

Finally, the groups of Würthner and Meerholz studied the application of squaraine dyes as donor materials for bulk heterojunction solar cells and reported power conversion efficiencies up to 1.8 % for a series of squaraine derivatives (**SQ2a-b** and **SQ5a-e**).^[7,95] Additionally, they used solutions of these dyes for spin-coating the active layer of OTFTs. These devices exhibited p-type behaviour with charge carrier mobilities between $5.5 \times 10^{-6} \text{ cm}^2 \text{ V}^{-1} \text{ s}^{-1}$ for **SQ5a** and $1.3 \times 10^{-3} \text{ cm}^2 \text{ V}^{-1} \text{ s}^{-1}$ for **SQ5d**, which was also the squaraine with the highest PCE in BHJ solar cells (1.8 %).^[7]

CHAPTER 3

RESULTS AND DISCUSSION

As it can be seen from the overview in Chapter 2.4.5, squaraine dyes may be an auspicious class of dyes for organic electronic applications. Hence this thesis focussed on studying the charge transport behaviour of a series of squaraines **SQa-f** (see Scheme 8), which were synthesized within the Würthner group by Dr. Ulrich Mayerhöffer (**SQb**, **SQd-f**) and Eva Kirchner (**SQa**, **SQc**). Squaraines **SQb-f** feature good solubility in common organic solvents with rising solubility from short to long alkyl chains, where concentrations of about 4 mg mL^{-1} in chloroform were determined for the dodecyl derivatives **SQd-f**.



Scheme 8. Chemical structures of the squaraine dyes used for TFT fabrication within this thesis.

Therefore transistor devices of those compounds were easy to process by spin coating from chloroform solutions, while the low solubility of **SQa** prevented processing of adequate films of this compound.

3.1 Squaraine-Based Thin-Film Transistors – Deposition by Spin Coating

3.1.1 Performance of the Transistor Devices

The OTFT devices were prepared by spin coating thin-films of **SQb-f** onto Si/SiO₂ substrates and subsequent vacuum deposition of gold through shadow masks texturing the

source and drain contacts. A second set of devices was prepared using the same procedure but with annealing of the thin-films for 10 minutes at 130 °C under Argon atmosphere prior to deposition of the gold contacts. Thermal annealing has been shown before to influence the film morphology of the active layer in a beneficial manner leading to improved transistor performance (see Chapter 2.3). The performance of the as spun as well as of thermally annealed p-type OTFTs is summarized in Table 3. It was found that the as spun films of the butyl-substituted selenium squaraine **SQb** showed no field effect, but elongation of the alkyl chains to octyl (**SQc**) and dodecyl (**SQd**) induced an increased transistor performance. For as spun OTFTs, the highest hole mobility (up to $0.017 \text{ cm}^2 \text{ V}^{-1} \text{ s}^{-1}$) was obtained for **SQd**. Improvement of the transistor characteristics could be achieved by annealing prior to contact deposition. In comparison to the as spun films, the mobility values for annealed devices were up to one order of magnitude higher. Within the series from methyl- to dodecyl-substituted selenium squaraines a maximum value of $0.037 \text{ cm}^2 \text{ V}^{-1} \text{ s}^{-1}$ was measured for the longest alkyl chain (**SQd**). The output and transfer characteristics of this device are depicted in Figure 22. Even for **SQb**, where no field effect for as cast films was detected, annealing led to mobility values higher than $1 \times 10^{-3} \text{ cm}^2 \text{ V}^{-1} \text{ s}^{-1}$. Comparing as cast and annealed devices reveals for both cases an increasing transistor performance with rising length of the alkyl substituents. Thermal treatment of the thin-films not only affects the charge carrier mobilities

Table 3. Summary of mean electrical properties for OTFTs of squaraine dyes **SQb-f** (averaged over three randomly picked devices), which were prepared by spin coating from solutions in chloroform on Si/SiO₂ substrates and measured in air.

Compound (X, R) ^[a]	Annealing ^[b]	μ_p [$10^{-2} \text{ cm}^2 \text{ V}^{-1} \text{ s}^{-1}$]	$I_{\text{on}}/I_{\text{off}}$	V_{th} [V]
SQb (Se, C ₄ H ₉)	✗ ✓	0.16±0.01	no field effect 10 ¹	24±1
SQc (Se, C ₈ H ₁₇)	✗ ✓	0.42±0.03 1.1±0.1	10 ¹ 10 ²	22±5 16±2
SQd (Se, C ₁₂ H ₂₅)	✗ ✓	1.7±0.1 3.7±0.1	10 ² 10 ⁴	16±5 6±1
SQe (S, C ₁₂ H ₂₅)	✗ ✓	0.054±0.004 7.3±0.5	10 ¹ 10 ²	58±4 11±1
SQf (O, C ₁₂ H ₂₅)	✗ ✓		no field effect no field effect	

^[a] See Scheme 8. ^[b] Annealing of the thin-film under Argon for 10 min at 130 °C.

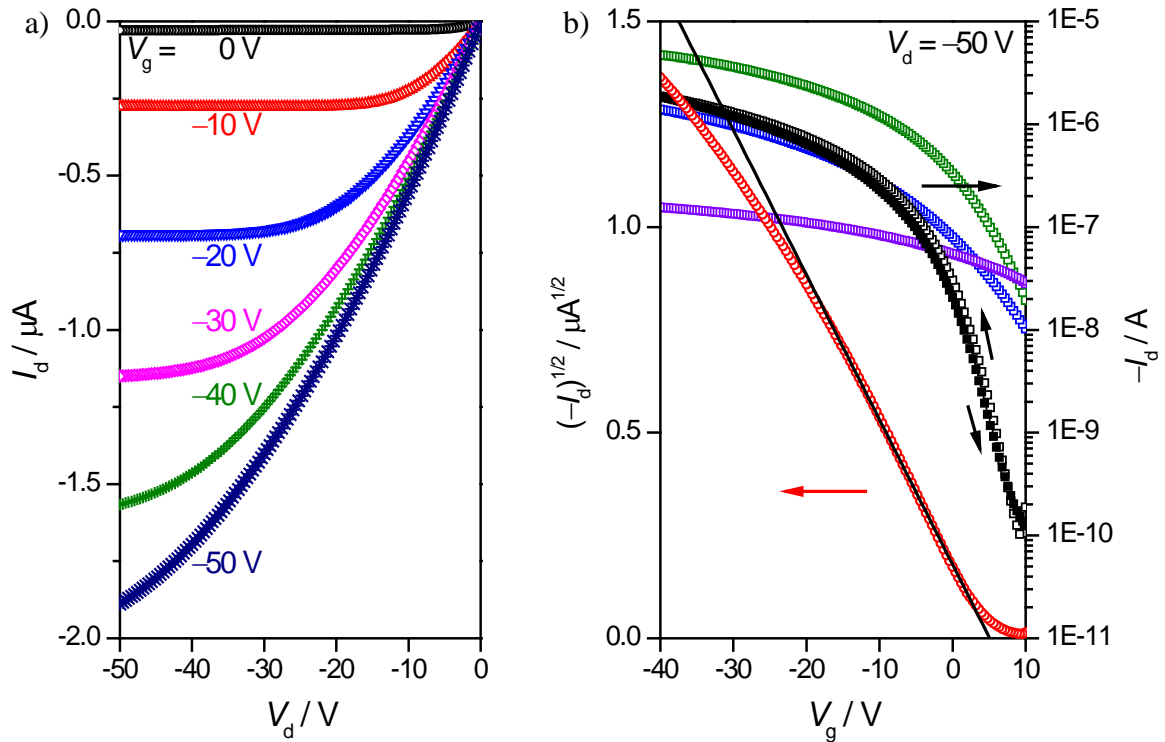


Figure 22. Output (a) and transfer (b) characteristics of a bottom-gate, top-contact OTFT based on an annealed thin-film of **SQd** deposited by spin coating. The respective transfer curves of such a device are colored black and red in b), while the forward measured transfer-characteristics of an as spun device of **SQd** (blue), of an as spun (purple) and of an annealed (green) **SQe**-based TFT are also shown.

but also leads to enhanced device performance with regard to the on/off ratios (up to two magnitudes of order higher) and the threshold voltages (reduction to at most one third). However, with threshold voltages in the positive regime and relatively high off-currents of about 10^{-8} A the transistor devices are not found to reach the ‘off’-state ($10^{-10} - 10^{-12}$ A). The transistor built from an annealed thin-film of **SQd** is the only exception within this series and approaches the ‘off’-state with an off-current of about 10^{-10} A (Figure 22b, black squares). In comparison to the as spun device (Figure 22b, blue squares), a decrease of the off-current is found for the annealed device, whereas the on-current is just about the same value for both devices and thus not affected by annealing. Neither for as cast nor for annealed devices based on oxygen squaraine **SQf** a field effect could be determined, while as cast films of sulfur squaraine **SQe** showed modest transistor performance with $\mu_{th} = 5.4 \times 10^{-4} \text{ cm}^2 \text{ V}^{-1} \text{ s}^{-1}$ and an on/off ratio of 10 (Figure 22b, purple squares). Again, annealing of the thin-film improved the OTFT characteristics (Figure 22b, green squares) and thus hole mobilities in the order of **SQd** were measured. The on/off ratios of the **SQe** devices rose to 10^2 because of an increase of the on-current with nearly constant current of the ‘off’-state (Figure 22b, green curve), but still lag two orders of magnitude behind those of the selenium squaraine **SQd**. Additionally, the threshold voltage of **SQe**-based OTFTs is twice as high as for **SQd**-based ones.

Considering all these results, one can conclude that selenium squaraine **SQd** features the best transistor performance amongst this series of compounds. Despite the relatively low mobilities (0.01 to $0.1 \text{ cm}^2 \text{ V}^{-1} \text{ s}^{-1}$) these TFTs exhibit the highest values reported so far for solution-deposited devices of squaraine dyes (see Chapter 2.4.5).

3.1.2 Spectroscopic and AFM Studies

Spin-coated thin-films of squaraines **SQb-d** were studied by AFM topography imaging before and after annealing (see Figure 23) to gain insight into the morphology of the films and the influence on transistor performance. The root-mean-square deviations of the surfaces of the as spun films were found to be between $\sim 1.0 \text{ nm}$ (**SQc** and **SQd**, Figure 23c and e) and $\sim 4.0 \text{ nm}$ (**SQb**, Figure 23a), where no significantly different values were determined upon annealing. The high roughness stemming from the grain boundaries within the as spun films of squaraine **SQb** (Figure 23a) appears to be responsible for the inappreciable field effect of this dye. While the RMS deviation is not affected by annealing, the number of holes diminishes (Figure 23b) and a field effect can be observed. Films of **SQc** and **SQd**, on the other hand, are much smoother (Figure 23c and e, respectively). Some larger domains indicating a higher degree of crystallinity can already be recognized in the as spun active layers of the latter squaraine. Thermal treatment increases the size of the domains and therewith the degree of crystallinity for both compounds (Figure 23d and f, respectively), where for **SQd** even larger crystallites are apparent. With these observations in mind, the increase of the transistor

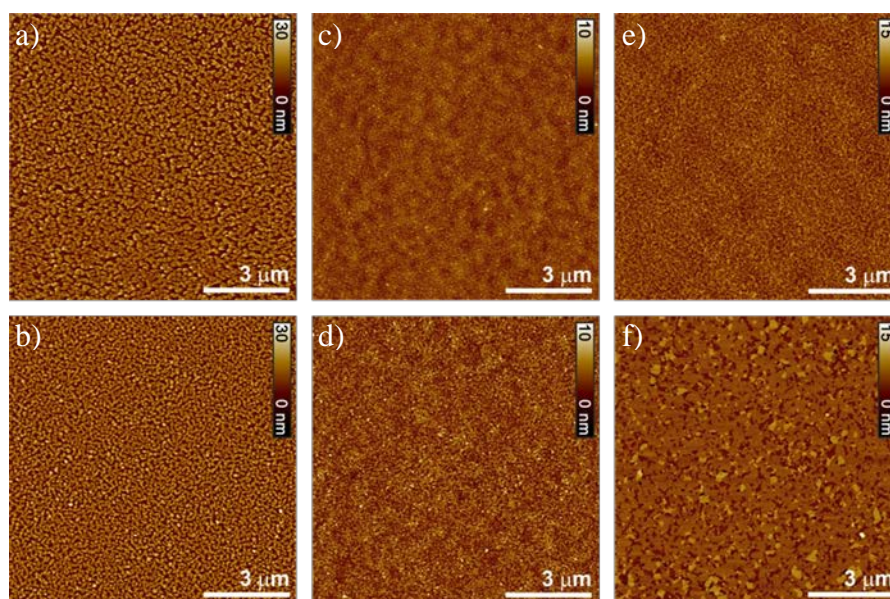


Figure 23. AFM topography images of thin-films prepared by spin coating of squaraine dyes **SQb** (a,b), **SQc** (c,d) and **SQd** (e,f) in CHCl_3 on SiO_2 . Images a), c) and e) show the morphology of the cast films, while b), d) and f) were recorded after annealing of the films for 10 minutes at $130 \text{ }^\circ\text{C}$ under argon atmosphere.

performance from **SQb** through to **SQd** and from as cast to annealed films seem to be related to the crystallinity and homogeneity of the thin-films. Beyond that, the AFM images allowed the determination of the film thickness and revealed for all three compounds similar values around 9 to 11 nm. Thus, it could be excluded that the differences in the OTFT behaviour originate from varying film thicknesses.

Spectroscopic studies were performed to exclude aggregation of the squaraine dyes in the solutions used for spin coating of the semiconductor thin-films. Additionally, the optical properties of thin-films can shed some light onto the packing arrangement of the active layers of OTFTs. UV/Vis/NIR absorption and fluorescence properties of squaraine dyes **SQa-f** were studied in methylene chloride, and the data are summarized in Table 4. Narrow absorption bands and small Stokes' shifts are observed, which decrease for the selenium squaraines **SQa-d** with increasing length of the alkyl chain (from 361 cm^{-1} to 302 cm^{-1}). The small bathochromic shift from **SQa** to **SQd** may be explained by the donor strength of the benzoselenazol group, which increases along with the +I-effect of the attached alkyl chain. This means that the donor-acceptor-donor structure of the squaraines slightly increases with the length of the alkyl substituent. Within the series of dodecyl-substituted squaraines **SQd-f** rising Stokes' shifts are calculated from the selenium over the sulfur to the oxygen derivative (302 cm^{-1} to 471 cm^{-1}). This effect may be accounted for by the decreasing electronegativity

Table 4. Summary of optical and redox properties of squaraines **SQa-f** in methylene chloride.

Compound (X, R) ^[a]	λ_{max} [nm]	ϵ [$\text{M}^{-1} \text{cm}^{-1}$]	λ_{em} [nm]	ϕ_{fl} [%]	$\Delta\nu$ [cm^{-1}]	E_{HOMO} [eV] ^[b]	E_{LUMO} [eV] ^[c]
SQa (Se, CH ₃)	716 382	163 000 36 200	735	71	361	— ^[d]	— ^[d]
SQb (Se, C ₄ H ₉)	718 382	168 000 37 600	736	89	340	-4.8	-3.1
SQc (Se, C ₈ H ₁₇)	719 382	167 000 36 300	736	89	321	-4.8	-3.1
SQd (Se, C ₁₂ H ₂₅)	720 382	173 000 37 900	736	91	302	-4.8	-3.1
SQe (S, C ₁₂ H ₂₅)	703 379	179 000 35 700	722	80	374	-4.8	-3.1
SQf (O, C ₁₂ H ₂₅)	626 383	151 000 63 800	645	98	471	-4.8	-2.8

^[a] See Scheme 1. ^[b] Calculated from CV measurements ($E_{1/2}^{\text{ox}}$) in methylene chloride calibrated against the ferrocene/ferrocenium couple (Fc/Fc⁺, -4.8 eV) as internal standard. ^[c] $E_{\text{LUMO}} = E_{\text{HOMO}} + (hc / \lambda_{\text{max}})$. ^[d] Solubility of **SQa** is too low for CV measurements.

and the increasing polarizability from oxygen (**SQd**) over sulfur (**SQe**) to selenium (**SQf**). With regard to classical squaraines such as **SQ2a** (see Chapter 2.4.5, $\Delta\nu = 219 \text{ cm}^{-1}$),^[95] these values are still rather small, what can be ascribed to only small changes of the geometry as well as the surrounding shell of solvent molecules upon excitation from the ground into the excited state. Squaraines **SQa-f** altogether exhibit in methylene chloride similar absorption and fluorescence properties with emission maxima in the region above 700 nm and high quantum yields (up to 98 % for **SQf**). Solvent dependent UV/Vis/NIR and fluorescence studies have been carried out exemplarily for squaraine **SQd** (see Figure 24). Small negative solvatochromism is observed in the range of the used solvents (methylene chloride, $\epsilon_r = 8.93$; chloroform, $\epsilon_r = 4.81$; 1,4-dioxane, $\epsilon_r = 2.21$; toluene, $\epsilon_r = 2.38$). One can extract from these studies that the energy levels of both ground and excited state are lowered in polar solvents but show a higher degree of stabilization for the former. This means higher polarity for the ground state than for the excited state and is indicative of the bipolarity of squaraines, which has been suggested before to be the driving force for packing arrangement in the solid state (cf. the highly dipolar merocyanine dye **MC3c** in Chapter 2.4.4).^[88] Furthermore, it can be seen from Figure 24 that absorption and emission spectra are mirror images, which suggests the presence of monomeric species in all these solvents. Additional support comes both from the comparable extinction coefficients at λ_{max} and fluorescence properties^[96] and the lack of appreciable spectral changes at high concentrations (up to 10^{-3} M in chloroform).

Thin-films of squaraine dyes **SQb-f** were prepared by spin coating from chloroform solutions on quartz substrates to get an insight into the active layers of squaraine OTFTs before and after annealing using optical spectroscopy. A similar morphology to that of the spin-coated OTFTs can be assumed because the surface of a dielectric layer consisting of

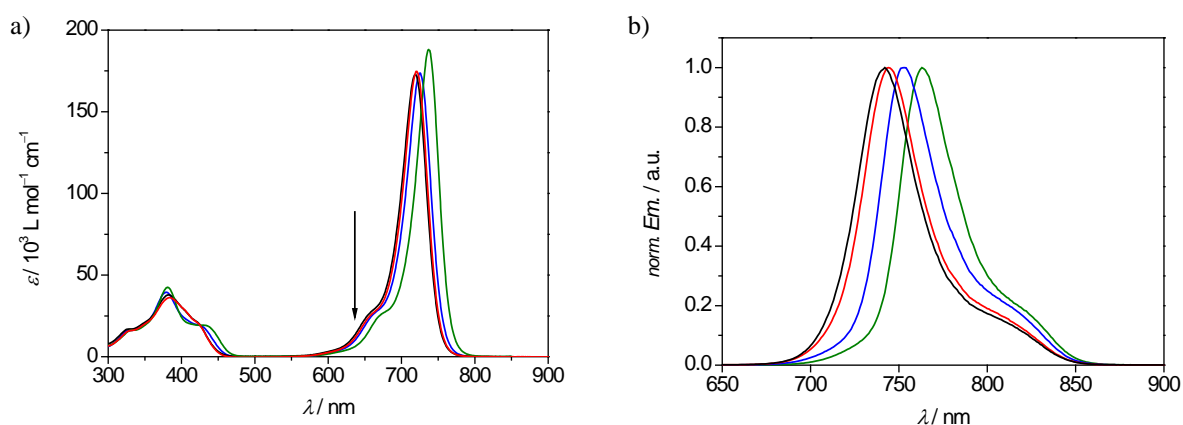


Figure 24. a) UV/Vis absorption spectra of 10^{-5} M solutions of squaraine dye **SQd** in methylene chloride (black), chloroform (red), 1,4-dioxane (blue) and toluene (green) and b) respective fluorescence spectra for **SQd** in these solvents which were recorded at an excitation wavelength of 640 nm (black arrow in (a)).

SiO₂ (RMS ~ 1.0 nm) is comparable to that of a quartz substrate (RMS ~ 3.8 nm). While no aggregation was observed even for highly concentrated solutions in chloroform, red-shifted absorption bands were found for the as cast films of all studied squaraines (see Figure 25), indicating J-type excitonic coupling in the thin-films. The broadened bands may be explained by either disorder or the presence of several allowed exciton transitions (Davydov splitting) in the solid state.^[97] Annealing of the as spun films under the same conditions used for the transistor devices caused changes such as sharpening (**SQb-e**) or broadening (**SQf**) of the red-shifted absorption band (Figure 25). Decomposition could be excluded by DSC analysis which also revealed the absence of phase transitions up to 130 °C for **SQb**, **SQc** and **SQe**. For **SQd** a transition to a liquid-crystalline phase is found at 25 °C. This does not affect the arrangement of the molecules in the thin-film, as indicated by the almost identical shape of both as cast and annealed thin-films as compared with the spectra of non liquid-crystalline squaraines with shorter alkyl chains, **SQb** and **SQc**. Due to exclusion of decomposition, the spectral changes can be attributed to a reorganization of the molecules on the quartz surface upon thermal treatment. The changes are most prominent for thin-films of **SQe** and **SQf**, in which a sharpening of the J-type band is accompanied by an increase of the intensity (**SQe**), whilst the band broadens and loses intensity for **SQf**. In addition, **SQe** shows the largest increase of the transition dipole moment for the J-type band upon annealing. As mentioned before, a comparable packing can be assumed for thin-films both on quartz substrates and on SiO₂ dielectric due to similar surface roughness. Hence, the improvement of the transistor

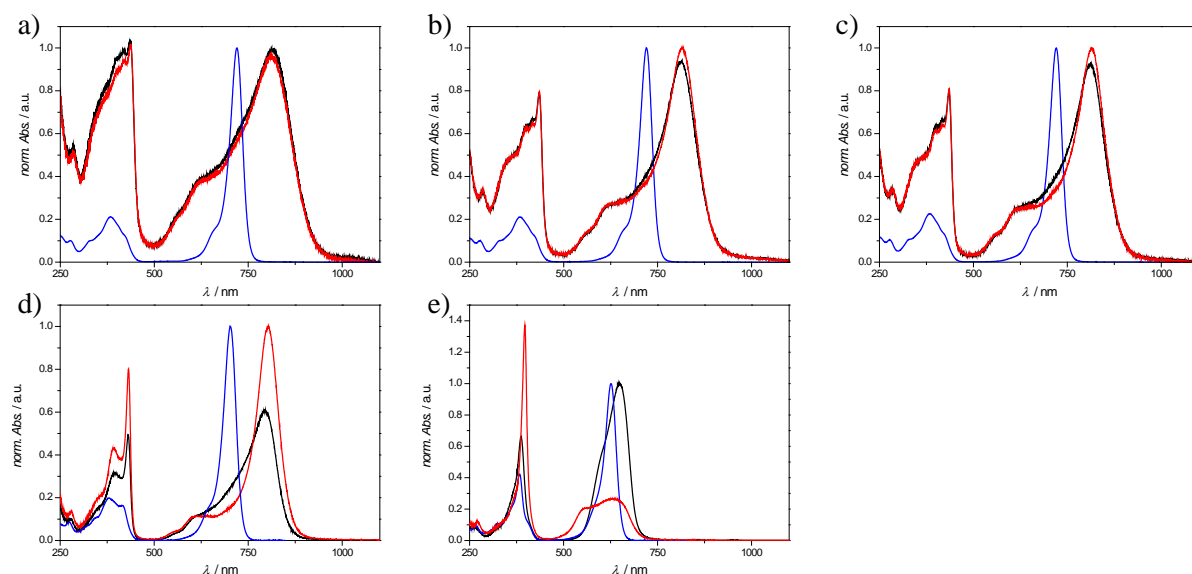


Figure 25. UV/Vis/NIR absorption spectra of thin-films on quartz substrates prepared by spin coating from a 10⁻³ M solution of squaraine dye **SQb** (a), **SQc** (b), **SQd** (c), **SQe** (d), and **SQf** (e) in chloroform. The spectra of the respective 10⁻⁵ M solutions in chloroform are shown in blue, the spectra of the as cast films in black, and those in red were recorded after annealing of the spin-coated films for 10 minutes at 130 °C under Argon.

performance for thin-films of **SQb-e** upon annealing can be correlated with the rearrangement of the molecules leading to J-type excitonic coupling, which seems to force the molecules to adopt an arrangement with transition dipole moments shifted clearly against each other.^[98]

In contrast to the other molecules, a phase transition is observed in the region around 100 °C for **SQf**. However, already the shape of the thin-film spectrum of **SQf**-based as cast film (see Figure 25e) is different from those of the other squaraine dyes. This indicates that the molecules might have another orientation with respect to the surface of the dielectric, e.g. they might be more tilted than in the case of **SQb-e**, leading to a dramatic decrease of the intensity accompanied by a band broadening upon annealing. These findings indicate that the interaction of the transition dipole moment with the incident light is less effective. Further tilting of the molecules due to the phase transition may be a reason for this observation. Since no field effect was determined for spin-coated devices of **SQf**, it seems that it adopts for as cast as well as for annealed thin-films a packing arrangement that is unfavorable for charge transport.

The HOMO and LUMO levels of all squaraines (see Table 4) were extracted from UV/Vis/NIR absorption and CV data to judge whether the different ability for charge transport comes from variation of these levels. The energies were found to be identical ($E_{\text{HOMO}} = -4.8$ eV, $E_{\text{LUMO}} = -3.1$ eV) for all squaraines studied in this thesis with the exception of the slightly higher LUMO level of **SQf** ($E_{\text{LUMO}} = -2.8$ eV). Consequently the HOMO levels cannot be the origin of the variations in the performance of p-type OTFTs based on the squaraine dyes **SQb-f**.

The low ionization potential of these squaraines, which is even lower than that of anthracene (-5.7 eV)^[99a], tetracene (-5.2 eV)^[99b] or pentacene (-5.0 eV)^[99c], results in a high sensitivity for oxidation of the molecules in the thin-films. This effect was systematically studied for pentacene-based TFTs, where freshly prepared devices were found to operate under inert conditions with on/off ratios of up to 10^6 .^[100] Rapid degradation by up to four orders of magnitude with finally almost failing transistor operation was observed for these devices upon exposure to ambient conditions. Because of their high-lying HOMO level, oxidation of the squaraine molecules in the thin-films is easier as compared to pentacene and, thus, gives an explanation for the only moderate on/off ratios obtained by preparation and characterization of the devices at ambient conditions.

Within this chapter it has been shown that the increase of OTFT performance upon thermal treatment can be attributed to changes of the film morphology, namely an increase of the crystallinity, and to molecular rearrangement leading to packing motifs more favourable

for hole transport. Hence, charge carrier mobilities of up to $0.1 \text{ cm}^2\text{V}^{-1}\text{s}^{-1}$ were measured under ambient conditions, which are the highest values known so far for solution-deposited squaraine-based TFT devices (cf. Chapter 2.4.5).

3.2 Squaraine-Based Thin-Film Transistors – Deposition by Solution Shearing

3.2.1 The Solution Shearing Method

In 2008, Bao and co-workers reported for the first time on the deposition of small-molecule organic semiconductors by solution shearing to obtain large-scale high quality thin-films.^[27e] Since then, only little interest has been spent on this method of solution processing (for a few examples see Chapter 2.4.2). Herein the basics of this method were adopted to build a shearing apparatus^[101], which facilitates preparation of solution-sheared OTFTs of squaraine dyes **SQd-f**. The setup of the apparatus is depicted in Figure 26b, whereas the principle of this method is schematically depicted in Figure 26a. The substrate is fixed on a basis built from copper, which can be heated by a precision heating stage to enable homogeneous distribution of the heat. Preheated blocks of copper act as carriers for the shearing tool which consists of a piece of substrate with dewetting surface (here: Si/SiO₂/OTES substrate). Due to different shapes of the holder for the shearing tool, the angle θ between the substrate and the shearing tool can be adjusted to certain values. The contact of the shearing tool with the substrate was controlled with the aid of a laser beam being reflected by a piece of Si/SiO₂ substrate glued to the backside. The beam projection along the axis of

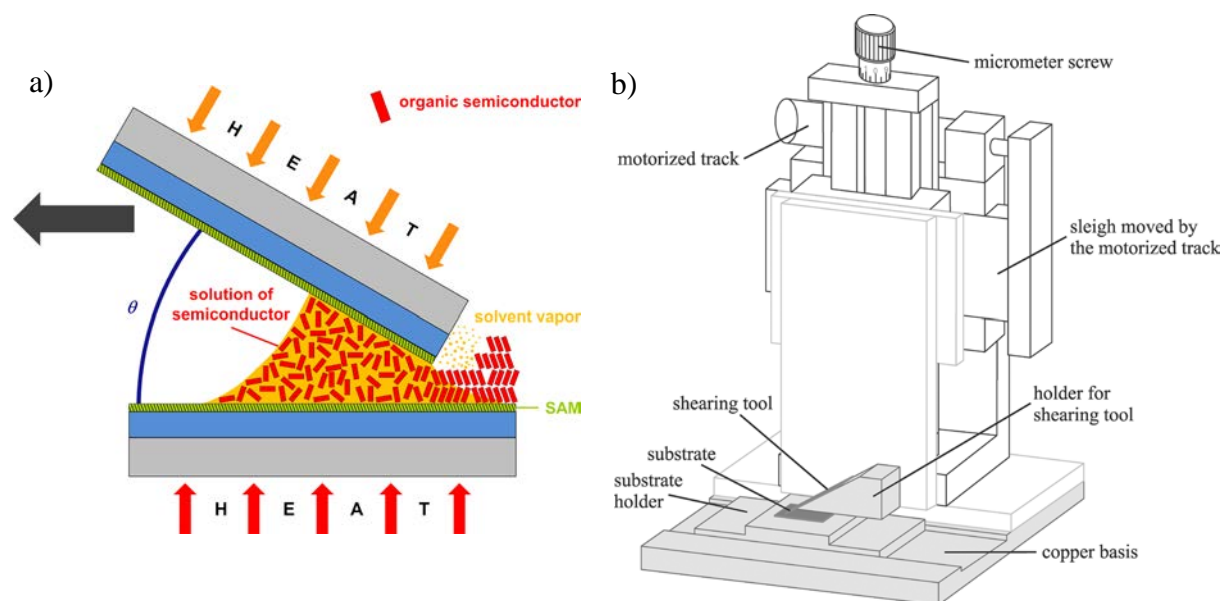


Figure 26. a) Schematic depiction of the solution-shearing method. b) Design drawing of the developed solution shearing apparatus, where the essential parts are labeled.^[102]

the micrometer screw is used for approaching the shearing tool to the substrate surface. As soon as the shearing tool touches the substrate, it bends slightly and hence the reflected laser beam reverses direction of movement. After adjusting the shearing tool, the heated semiconductor solution (~40 μL) is deposited into the remaining gap and the shearing tool subsequently is moved by a motorized track at a slow, adjustable velocity. Evaporation of the solvent from the thin solution film on the substrate surface starts at the edge of the shearing tool, which induces a continuously rising concentration gradient along the direction of shearing. The result is the formation of thin-films, which exhibit large, crystalline domains oriented along the moving direction of the shearing tool.^[68]

Herein, solutions of squaraine dyes **SQd-f** in *o*-DCB were used to fabricate solution-sheared thin-films of these compounds, which have been proven before by spin-coating to be the most promising candidates regarding OFET performance (see Chapter 3.1). *o*-DCB has been chosen as solvent both for the good solubility of the squaraines therein and its high boiling point, which allows processing at elevated temperatures. An OTES-functionalized wafer was used as the shearing tool, while all the other conditions such as the substrate, shearing angle, shearing velocity, concentration, etc. were optimized (see Chapter 3.2.2). Finally, all the OFETs were completed by deposition of source and drain contacts by evaporation of gold through shadow masks onto the thin-films. The orientation of the devices is termed in this thesis as follows: they are called parallel, if the transistor channel is aligned along the shearing direction, whereas perpendicular orientation means that this direction and the channel form a right angle.

3.2.2 Optimization of the Processing Conditions

Optimization of the conditions used for solution shearing is needed prior to the investigation of the three squaraines with the best solubility (**SQd-f**). In Chapter 3.1 spin-coated transistor devices based on squaraines were studied, from which **SQd** was shown to exhibit the best transistor characteristics. Hence, this compound was chosen for the optimization of the processing conditions, while these were later applied for a comparative study of OTFTs based on **SQd-f** deposition (see Chapter 3.2.3).

The conditions applied by our group for the preparation of thin-films of NDI **Cl,H-NDI-CH₂C₃F₇** (see Chapter 2.4.2) were taken as a starting point for the processing of squaraine **SQd** by solution shearing.^[68] The angle between the substrate and the shearing tool was adjusted to a value of 30°, the shearing velocity was set to 0.083 mm s⁻¹, and the solutions had a concentration of 2 mg mL⁻¹. However, a first variation was made for the temperatures

Table 5. Ambient-stable hole mobilities (μ_p) and on/off ratios (I_{on}/I_{off}) of **SQd**-based OTFTs, which were prepared on Si/SiO₂ substrates by solution shearing ($\theta=30^\circ$) from an *o*-DCB solution with a concentration of 2 mg mL⁻¹. The temperature T of the shearing tool and of the substrate as well as the number n of the measured devices are also given. The orientation of TFTs with respect to the direction of shearing is symbolized by \parallel and \perp .

	$T = 100\text{ }^\circ\text{C}$				$T = 130\text{ }^\circ\text{C}$			
	$\bar{\mu}_p^{[a]}$	$\mu_{p,max}^{[a]}$	I_{on}^-/I_{off}^-	n	$\bar{\mu}_p^{[a]}$	$\mu_{p,max}^{[a]}$	I_{on}^-/I_{off}^-	n
\parallel	1.4±1.8	6.3	10 ²	9	7.4±5.5	19	10 ³	12
\perp	0.37±0.31	1.2	10 ²	9	3.0±1.4	5.1	10 ³	12

^[a] in 10⁻² cm² V⁻¹ s⁻¹

of the shearing tool and substrate. Two sets of transistor devices were obtained, one by films was obtained at higher temperatures, which is reflected by the up to one order of magnitude higher charge carrier mobilities and on/off current ratios. As a result, the temperature of substrate and shearing tool was fixed to 130 °C for the following studies. It is also evident from the data in Table 5 that the charge transport within the films is anisotropic with respect to the direction of shearing. Devices with parallel orientation show higher hole mobilities than those oriented perpendicularly, which will be discussed in detail for devices obtained after optimization of the processing conditions.

Shearing speeds slower than 0.083 mm s⁻¹ failed to give a closed covering of thin-film. Processing of closed films was possible only when the velocity is equal or higher than 0.083 mm s⁻¹. It was fixed to this lowest possible value for further optimization of the solution shearing process to keep the evaporation of the solvent and the subsequent growth of the semiconductor film at low rates. The studies of **Cl,H-NDI-CH₂C₃F₇** (see Chapter 2.4.2) already have shown the importance of the shearing angle θ for the quality of the thin-films. Thus, OTFTs based on **SQd** were processed at five different angles between 0° and 60° (in steps of 15°) and additionally at an angle of 90°. Solely for a value of 45° it was not possible to deposit a thin-film onto the Si/SiO₂ substrate, whereas at all the other angles a closed covering was obtained. Up to an angle of 30° large-area and homogeneous films were

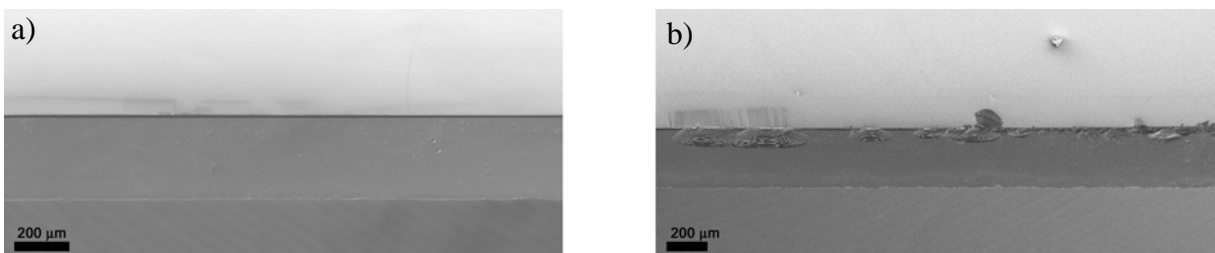


Figure 27. SEM images of the edge of the shearing tool taken at different positions.

Table 6. Maximum ambient hole mobilities of **SQd**-based OTFTs, which were prepared on Si/SiO₂ substrates by solution shearing from an *o*-DCB solution with a concentration of 2 mg mL⁻¹. The shearing angle θ was varied from 0° up to 90°. The orientation of TFTs with respect to the direction of shearing is symbolized by \parallel and \perp .

	$\mu_{p,max} / 10^{-2} \text{ cm}^2 \text{ V}^{-1} \text{ s}^{-1}$					
θ	0°	15°	30°	45°	60°	90°
\parallel	13	23	1.8	--- [a]	6.2 [b]	4.1 [b]
\perp	3.7	9.9	0.21	--- [a]	0.49 [b]	0.21 [b]

[a] No closed film obtained. [b] Only small area covered with closed film.

observed, but for $\theta = 60^\circ$ and higher angles only small regions of the substrate were covered with a semiconductor film. Deposition was achieved for all angles by using the same piece of OTES-modified substrate as shearing tool to exclude variations in the film morphology caused by different tools. This had to be considered, because preparation of the shearing tool by breaking whole wafers into small pieces never leads to identical edges of the substrates. The structure of the edge of the used shearing tool was investigated by scanning electron microscopy (SEM). The images show regions nearly without any defects but also ranges with outbreaks at the edge (Figure 27). This may be one of the impediments for the formation of completely homogeneous films all over the width of the substrate. The highest hole mobility of $0.23 \text{ cm}^2 \text{ V}^{-1} \text{ s}^{-1}$ at ambient conditions was determined for a transistor device prepared at an angle of 15° . This angle seems to promote the formation of thin-films with a packing arrangement favoring the charge transport. The other angles led to lower transistor performance, the values of which are summarized in Table 6. Once more, the anisotropy for devices oriented parallel and perpendicularly to the shearing direction is evident, where the former are up to one order of magnitude higher.

With the results of Table 6 in mind, the shearing angle was fixed to an optimum value of 15° followed by a study of the influence of the concentration. For this purpose, a dilution

Table 7. Maximal values for the ambient hole mobility of **SQd**-based OTFTs, which were prepared on Si/SiO₂ substrates by solution shearing ($\theta = 15^\circ$) from *o*-DCB solutions with various concentrations c . The orientation of TFTs with respect to the direction of shearing is symbolized by \parallel and \perp .

	$\mu_{p,max} / 10^{-2} \text{ cm}^2 \text{ V}^{-1} \text{ s}^{-1}$						
$c^{[a]}$	20	10	5.0	2.5	1.3	0.65	0.33
\parallel	2.9	7.8	1.1	4.5	2.1	4.1	2.2
\perp	0.54	3.1	1.2	0.17	0.14	1.2	0.62

[a] in mg mL⁻¹.

series of **SQd** in *o*-DCB ranging from 20 to 0.33 mg mL⁻¹ was prepared and the solutions were used for solution shearing on Si/SiO₂ substrates. As can be seen from Table 7, no significant differences in the transistor performance were found for the various concentrations. Those devices oriented parallel to the direction of shearing predominantly exhibit charge carrier mobilities within the narrow range from 0.01 up to 0.08 cm² V⁻¹ s⁻¹. As no clear trend can be extracted from the data summarized in Table 7, it appears that the concentration of the solution has a negligible influence on the formation and quality of the films. This suggests that the crystallization process does not take place directly beyond the shearing tool. Instead, a thin solution film with a concentration gradient due to continuous evaporation of the solvent is formed behind the shearing tool (see Figure 26a). After the concentration within this film has reached a critical value due to solvent evaporation, a crystallization zone that propagates in the direction of shearing can be observed. This region will be near to the edge of the shearing tool for highly concentrated solutions. For less concentrated solutions, a larger amount of solvent has to evaporate, which results in the formation of a larger region with concentration gradient and hence the crystallization zone being further apart from the shearing tool. However, the mechanism of film formation by solution shearing has not been studied in detail within this work. Due to the observed concentration independence, the concentration was set to the initially used value of 2 mg mL⁻¹ for further investigations.

Finally it was shown in this chapter, that heating the shearing tool and the substrate to 130 °C in combination with a shearing angle of 15° and a shearing velocity of 0.086 mm⁻¹ can be used as a good starting point for comparing studies of solution-sheared OTFTs from heated solutions of the squaraines **SQd-f** (*c* = 2 mg mL⁻¹) in *o*-DCB.

3.2.3 Performance and Long Term Stability of Transistor Devices Prepared under Optimized Conditions

Large-scale (~2.25 cm²), high quality thin-films of the squaraine dyes **SQd-f** were obtained on Si/SiO₂ substrates using the previously optimized shearing conditions. The transistor performance of the devices is summarized in Table 8. It is found that ambient transistor performance increases from the oxygen squaraine **SQf** over sulfur squaraine **SQe** to the selenium squaraine **SQd**, where the hole mobility (0.15 cm² V⁻¹ s⁻¹) for the latter is more than three orders of magnitude higher than that for the former. It is remarkable that spin-coated devices of **SQf** did not show a field effect (see Chapter 3.1), but processing thin-films by solution shearing leads to charge carrier mobility in the range of 10⁻⁴ cm² V⁻¹ s⁻¹. In

Table 8. Summary of ambient electrical properties for OTFTs of squaraine dyes **SQd-f** prepared by solution shearing (SS) from *o*-DCB on Si/SiO₂ ($\theta = 15^\circ$) and with HMDS-SAM ($\theta = 0^\circ$), respectively.

Compound (X, R) ^[a]	SAM	Orientation ^[b]	$\mu_{p,max} /$ $10^{-2} \text{ cm}^2 \text{ V}^{-1} \text{ s}^{-1}$	$\bar{\mu}_p /$ $10^{-2} \text{ cm}^2 \text{ V}^{-1} \text{ s}^{-1}$	I_{on}/I_{off}	$V_{th} /$ V
SQf (O, C ₁₂ H ₂₅)	---	∥	0.015	0.012±0.004	10 ²	7±3
		⊥	0.011	0.010±0.001	10 ²	6±4
SQe (S, C ₁₂ H ₂₅)	---	∥	5.0	1.7±2	10 ¹	54±19
		⊥	0.63	0.25±0.2	10 ¹	57±20
SQd (Se, C ₁₂ H ₂₅)	---	∥	21	15±5	10 ³	11±8
		⊥	2.0	0.66±0.81	10 ²	16±3
SQd (Se, C ₁₂ H ₂₅)	HMDS	∥	45	37±6	10 ³	5±1
	HMDS	⊥	12	11±1	10 ³	5±1

^[a] See Scheme 8. ^[b] The orientation of TFTs with respect to the direction of shearing is symbolized by ∥ and ⊥.

general, the mobilities obtained for solution-sheared devices are at least one order of magnitude higher than those of the respective spin-coated devices (see Chapter 3.1). This can be seen as a first indication for the better film quality enabled by the directed deposition of the thin-film. As observed already during the optimization of the shearing conditions, an anisotropy in the charge carrier mobility in dependence of the orientation of the measured devices with respect to the direction of shearing was observed for thin-films deposited by this method.

OTFTs of **SQd-f**, which are oriented parallel to the direction of shearing, exhibit mobility values that are three to four times higher than those found for devices with perpendicular orientation. Finally, the optimized processing conditions for the deposition on Si/SiO₂ substrates led to a maximum mobility of $0.21 \text{ cm}^2 \text{ V}^{-1} \text{ s}^{-1}$ and an average mobility of $0.15 \pm 5 \text{ cm}^2 \text{ V}^{-1} \text{ s}^{-1}$ for devices of **SQd** with parallel orientation to the shearing direction, while devices with perpendicular orientation exhibited an average mobility of only $0.0066 \pm 0.008 \text{ cm}^2 \text{ V}^{-1} \text{ s}^{-1}$.

Self-assembled monolayers are known to be useful for the optimization of the interface between the semiconductor and dielectric, leading to reduced surface energies, less charge trapping and improved film morphology.^[8e] Thus, a monolayer of HMDS was introduced onto the Si/SiO₂ substrates. Due to the dewetting properties of this SAM a deposition of the thin-film applying a shearing angle of 15° could not be accomplished. It was found, that switching to $\theta = 0^\circ$ helps to overcome this drawback by forcing the solution between the substrate and

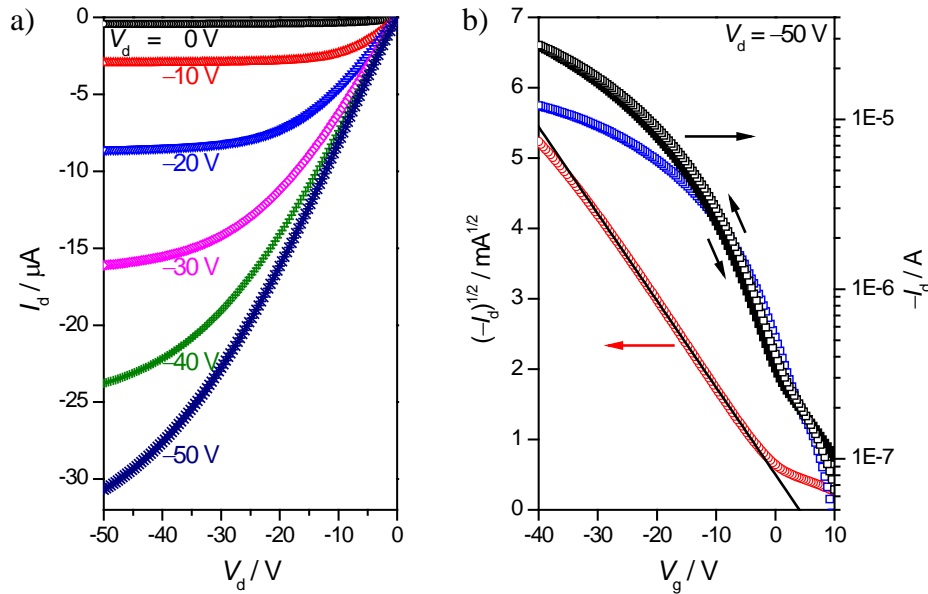


Figure 28. a) Output and b) transfer characteristics of a bottom-gate, top-contact OTFT of squaraine dye **SQd** on Si/SiO₂/HMDS measured under ambient conditions. The respective transfer curves of such a device are colored black and red in b), while the forward measured transfer-characteristic of a device on Si/SiO₂ substrate (blue) is also shown.

the shearing tool. This change in the deposition conditions also makes the fabrication of high quality and square centimeter-sized thin-films of **SQd** on SAM-modified substrates possible. The introduction of the HMDS monolayer increased the maximum mobility up to $0.45 \text{ cm}^2 \text{ V}^{-1} \text{ s}^{-1}$ (on/off ratio of 10^3 and threshold voltage of 5 V) and an average mobility of $0.37 \pm 0.06 \text{ cm}^2 \text{ V}^{-1} \text{ s}^{-1}$ for 20 devices oriented parallel to the shearing direction was found while devices with perpendicular orientation exhibited an average mobility of only $0.11 \pm 0.01 \text{ cm}^2 \text{ V}^{-1} \text{ s}^{-1}$. Output and transfer characteristics of the OTFT with the highest charge carrier mobility of $0.45 \text{ cm}^2 \text{ V}^{-1} \text{ s}^{-1}$ are shown in Figure 28. Furthermore, the transfer curve of a transistor built on Si/SiO₂ is plotted in Figure 28b showing the more curved appearance representing the lower hole mobility of this device. It also makes clear that there is not much difference in the on/off ratios for Si/SiO₂ and Si/SiO₂/HMDS substrates. Representative optical polarizing microscopy pictures of such devices taken at different angles between crossed polarizers are depicted in Figure 29, where for 32 transistor devices (20 with parallel and 12 with perpendicular orientation with respect to the shearing direction) the field effect mobilities are visualized by a color code in Figure 29a. The anisotropy in the OFET performance is evident from this illustration, as all devices perpendicular to the shearing direction show considerable lower mobility values than those oriented in a parallel fashion. The OPM pictures also provide clear evidence for the good orientation and crystallinity of the **SQd** thin-films, as they show extended ribbon-like structures along the direction of shearing.

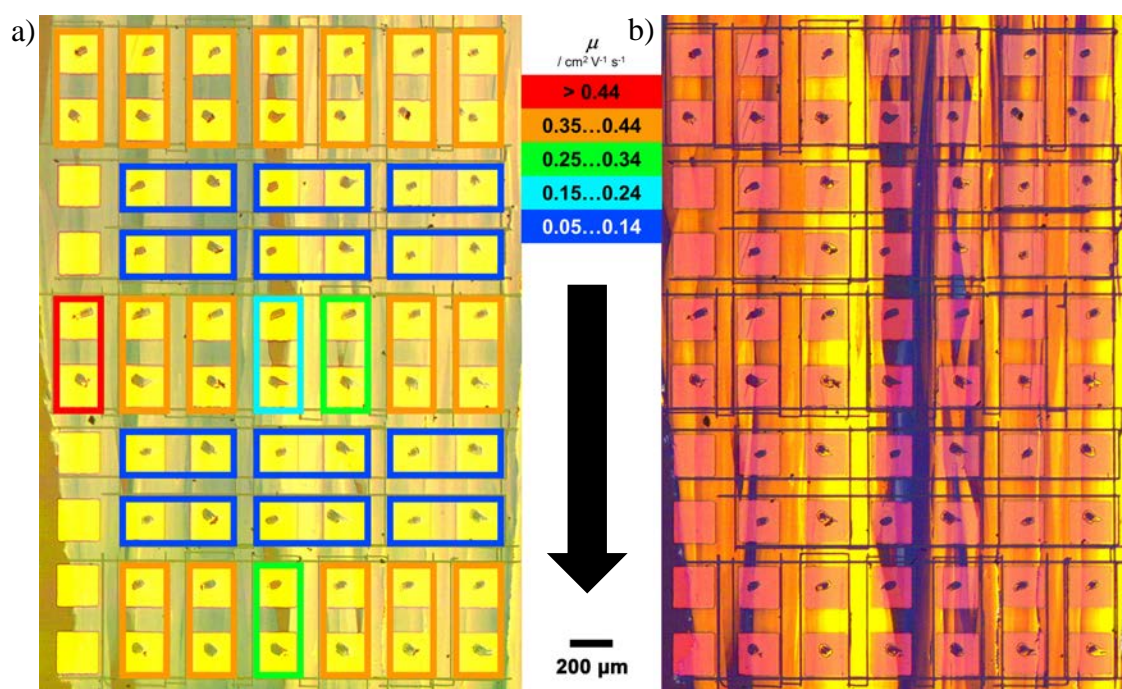


Figure 29. a) and b) OPM pictures of thin-films prepared by solution shearing of squaraine dye **SQd** on Si/SiO₂/HMDS taken at different angles between crossed polarizers, with an overlay for a), which represents the field effect mobilities of 32 TFTs (20 parallel and 12 perpendicular with respect to the shearing direction). The direction of shearing is indicated by the arrow.

Introduction of the HMDS SAM also shifts V_{th} to lower values (5 V), but still the transistors exhibit low on/off ratios in the magnitude of 10^3 and never reach the ‘off’-state similar to the spin-coated devices (see Chapter 3.1). This again can be attributed to the high-lying HOMO level of the squaraine dyes ($E_{HOMO} = -4.8$ eV) meaning generation of oxidized species in the semiconductor thin-film upon preparation and characterization at ambient conditions comparable to the effects reported for pentacene-based devices.^[100] Therefore, charge transport is already possible without a gate-source voltage applied due to the charges generated by oxidation, and V_{th} is consequently shifted to more positive values. For comparison, OTFT devices with a mean mobility value of only 0.030 ± 0.004 cm² V⁻¹ s⁻¹ (on/off ratio of 10^2 and threshold voltage of 6 V) were obtained by spin coating of **SQd** in CHCl₃ onto the same HMDS-modified substrates. Annealing of these thin-films for 10 minutes at 130 °C under Argon atmosphere slightly raised the mean mobility to a value of 0.032 ± 0.001 cm² V⁻¹ s⁻¹ with these devices exhibiting a lower standard deviation compared to the as cast ones. While no change in the threshold voltage was observed, the thermal treatment induced a change in the thin-film morphology, which led to a dramatic increase of the on/off ratio ($\leq 10^4$) by two magnitudes of order and which is in the same order of magnitude of solution-sheared devices.

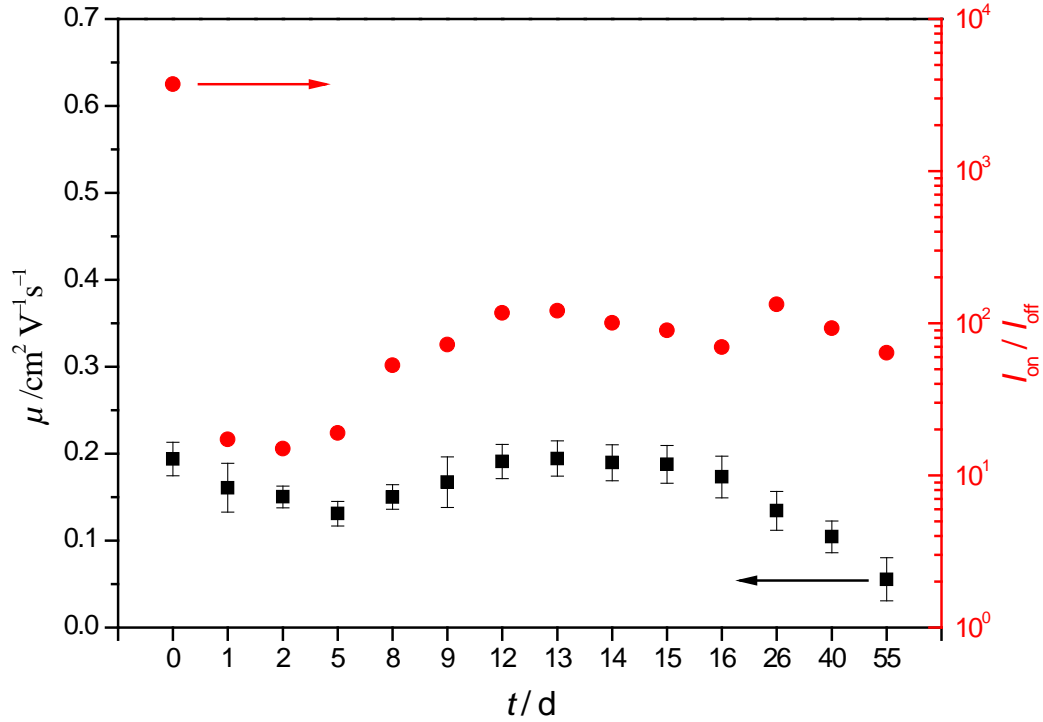


Figure 30. Averaged hole mobilities and $I_{\text{on}}/I_{\text{off}}$ ratios for five **SQd** OTFTs, which were processed by solution shearing onto Si/SiO₂ and stored for the time t at ambient conditions. The respective standard deviation for the charge carrier mobility is depicted by a bar.

Five solution-sheared **SQd** OTFTs on a Si/SiO₂ substrate, which are oriented along the direction of shearing, have been subjected to a long-term study at ambient conditions. For these devices, the output and transfer characteristics were both recorded once at specific days over a period of 55 days. The trend over time for the averaged hole mobility and the on/off ratio is depicted in Figure 30. The freshly prepared OTFTs exhibited a hole mobility of $0.19 \text{ cm}^2 \text{V}^{-1} \text{s}^{-1}$ with an on/off ratio of 10^3 (each averaged over the five transistors). A dramatic decrease of $I_{\text{on}}/I_{\text{off}}$ to 10^1 was already observed after one day of exposure to air, while the mobility values were almost constant within the range from 0.15 to $0.20 \text{ cm}^2 \text{V}^{-1} \text{s}^{-1}$ for the first 16 days. In the following period, a continuous decrease to $0.06 \text{ cm}^2 \text{V}^{-1} \text{s}^{-1}$ after 55 days was found. The on/off ratio recovers after eight days back to a value of 10^2 and remains constant until the end of the study. Threshold voltage is affected to a lesser extent by storage of the device under ambient conditions, which is indicated by only a slight increase of the threshold voltage from about 8 V up to 13 V (after 55 days). In summary, it can be stated that only moderate stability of **SQd** transistor devices upon exposure to air can be reported over a period of 55 days, where the mobility dropped finally to approximately 25 % of the initial value. This is in accordance to other p-type organic semiconductors with high-lying HOMO levels, such as pentacene, which, when used as active layer of OTFTs, exhibited rapid degradation upon exposure to ambient conditions.^[100] However, repeated contacting of the

electrodes leads to their destruction with the concomitant reduction of the induction area. This has also to be taken into account as an additional effect decreasing the transistor performance but is not the main reason for the dramatic decrease of the performance after one day of exposure to air. At this time the devices were just contacted for the second time with the electrodes still being virtually intact.

3.2.4 Spectroscopic and AFM Studies of the Thin-Films

AFM images were recorded to investigate the influence of the morphology on the charge transport properties of squaraine thin-films. To that end, films deposited on Si/SiO₂, Si/SiO₂/HMDS as well as quartz substrates were studied. Optical spectroscopy of these films will be discussed below with regard to the packing arrangement of the molecules. As already discussed in Chapter 3.1, film morphology on quartz can be seen as a good measure for the active layer on Si/SiO₂ substrates, which could not be studied itself by optical spectroscopy. All films exhibit a similar topography with extended ribbons oriented along the shearing direction (see Figure 31). Large-scale textures covering the whole channel of a single transistor device were found on Si/SiO₂ substrates, which indicate a quite homogenous alignment along the direction of shearing in dimensions greater than 100 μm (Figure 31a). An even higher degree of orientation with extended grain size and high crystallinity is found for the films on HMDS-modified Si/SiO₂ substrates (Figure 31b). The magnification shows the

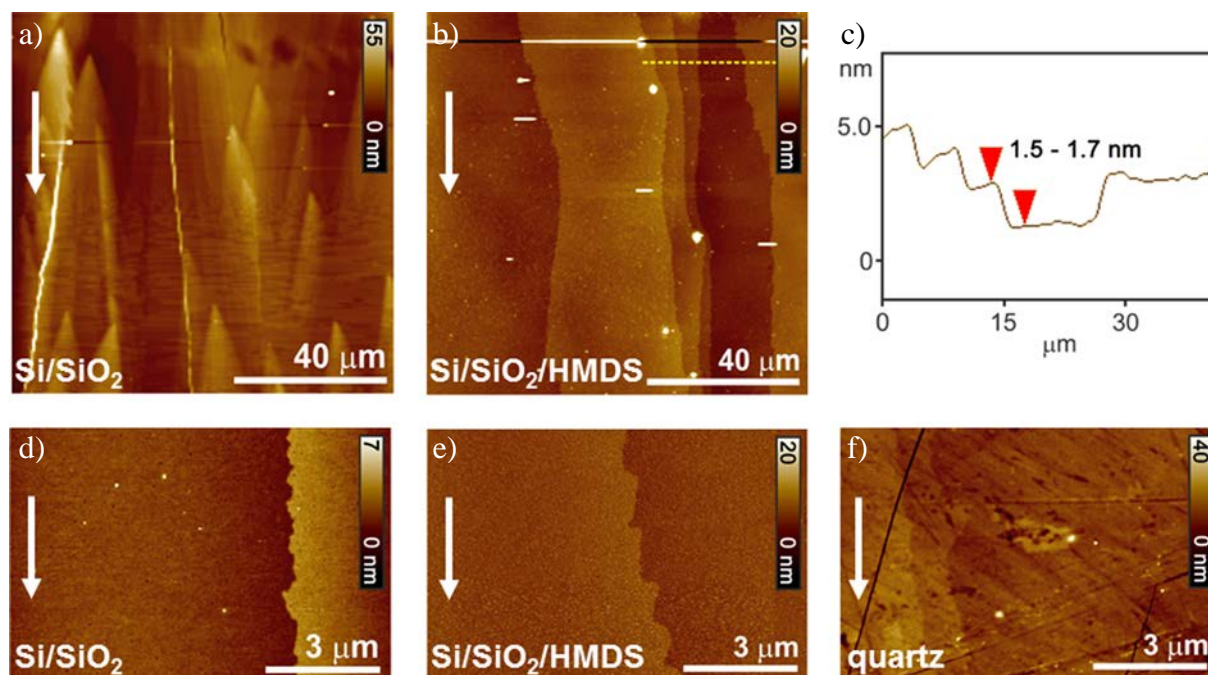


Figure 31. AFM topography images of thin-films prepared by solution shearing of squaraine dye SQd on Si/SiO₂ (a,d), on Si/SiO₂/HMDS (b,e), and on quartz (f). c) Cross section analysis along the yellow dashed line in b). The direction of shearing is indicated by the arrows.

high quality of the thin-films with a low roughness [$\text{RMS}(\mathbf{SQd}$ on Si/SiO_2) = 0.4 nm, Figure 31d; $\text{RMS}(\mathbf{SQd}$ on $\text{Si}/\text{SiO}_2/\text{HMDS}$) = 0.8–1.2 nm, Figure 31e], which equals the values determined for the uncoated substrates. Thin-films prepared on quartz substrates exhibited similar morphology with ribbon like structures and slightly higher roughness [$\text{RMS}(\mathbf{SQd}$ on quartz) = 1.6–2.0 nm, Figure 31f] in comparison to those films on Si/SiO_2 , which was expected due to bare quartz substrates being already rougher than bare Si/SiO_2 . This can be seen as a first indication for the packing arrangement on quartz being quite similar to that on Si/SiO_2 substrates. As a consequence, the results from the optical studies discussed below can be correlated to the transistor performance. By analyzing the AFM images it was possible to determine the thickness of the spin-coated thin-films. It was found to be in the range of about 30 nm for Si/SiO_2 substrates and about 20 nm for squaraine semiconductor films deposited on $\text{Si}/\text{SiO}_2/\text{HMDS}$ substrates. In addition, cross section analysis of a \mathbf{SQd} thin-film on a HMDS-modified Si/SiO_2 wafer reveals a layer-by-layer structure of the solution-sheared film with the height of each step in the range of 1.5 to 1.7 nm (Figure 31c). As this value matches the dimension of small molecules, it seems likely that solution shearing leads to deposition of stacked layers of the squaraine dyes.

UV/Vis/NIR absorption spectra of a solution-sheared and a spin-coated thin-film of \mathbf{SQd} on quartz substrates were recorded using linearly polarized light (Figure 32). Analogous to the spin-coated films (see Chapter 3.1), deposition of the semiconductor layer by solution shearing leads to a bathochromic shift of the absorption maximum ($\lambda_{\text{max}}(\text{thin-film}) = 801 \text{ nm}$) in comparison to the spectra in solution ($\lambda_{\text{max}}(\text{solution}) = 732 \text{ nm}$) due to J-type excitonic coupling of the molecules in the thin-film. Broadening of the band may be attributed either to

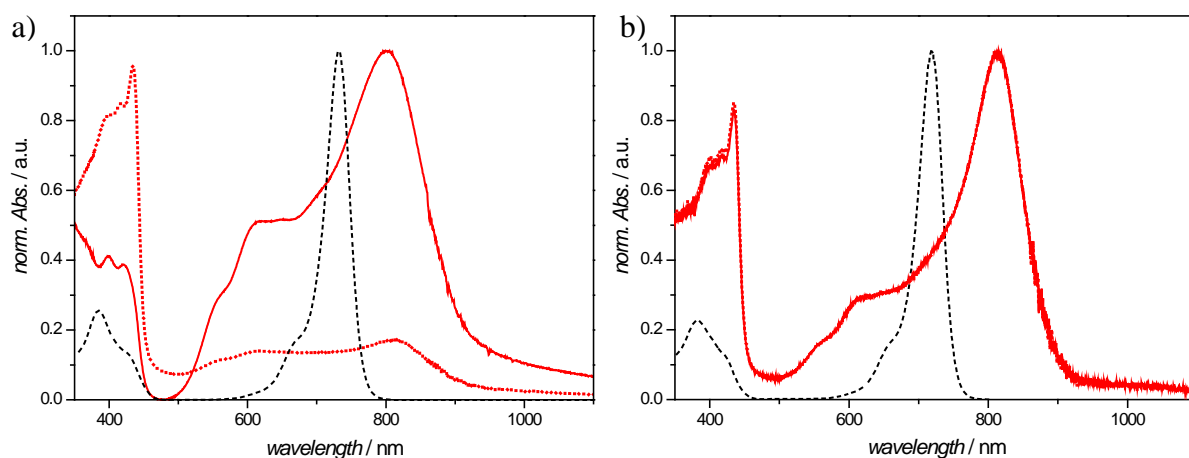


Figure 32. Normalized UV/Vis/NIR absorption spectra of squaraine dye \mathbf{SQd} in solution (black, dashed; a) *o*-DCB; b) CHCl_3) and of its solution sheared (a) and spin-coated (b) thin-films (red). The thin-film absorbance was measured with linearly polarized light oriented parallel (solid; $\alpha = 0^\circ$) and perpendicularly (dotted; $\alpha = 90^\circ$) with respect to the shearing direction.

disorder or the presence of several allowed exciton transitions (Davydov splitting) in the solid state.^[97] The spectra in Figure 32a exhibit a dramatic drop of the intensity of this band upon rotation of the axis of the polarized light from parallel ($\alpha = 0^\circ$) to perpendicular orientation ($\alpha = 90^\circ$) with respect to the shearing direction. This can be attributed to the fact that the transition dipole moment related to the broad band with the maximum at 732 nm has to be aligned parallel to the direction of shearing. Exactly the opposite behavior is observed for the second band at around 430 nm: maximal absorption is observed for perpendicularly polarized light, whereas the intensity drops on rotation of the axis of the polarized light to 0° . That implies that the transition from the ground to the excited state is polarized for this band at right angles with respect to the shearing direction and thus also perpendicular to the transition dipole moment of the long-wavelength band. It is evident from this data, that the molecules in a solution-sheared thin-film adopt an alignment in which the transition dipole of the band with a maximum at 801 nm is oriented mostly along this direction, while transition of the high energy absorption band is aligned perpendicularly. The degree of orientation in a thin-film can be estimated by the dichroic ratio D_λ and the therefrom derived order parameter S_λ

$$D_\lambda = \frac{A_{\lambda,\max}}{A_{\lambda,\min}}, \quad (3.2.1)$$

$$S_\lambda = \frac{A_{\lambda,\max} - A_{\lambda,\min}}{A_{\lambda,\max} + 2A_{\lambda,\min}} = \frac{D_\lambda - 1}{D_\lambda + 2}, \quad (3.2.2)$$

where $A_{\lambda,\max}$ and $A_{\lambda,\min}$ are the maximum and minimum absorption at a certain wavelength λ with the angle α being either 0° or 90° .^[104] A dichroic ratio D_{801} and an order parameter S_{801} are calculated for the absorption maximum of the solution-sheared film at 801 nm to a value of 5.9 and 0.62, respectively. Calculations for the maximum at 434 nm yield $D_{434} = 3.0$ and $S_{434} = 0.40$. For comparison, D -values of about 2.2 up to 15 ($S \sim 0.29$ up to 0.82) for liquid crystals^[104a,b] and of 41 ($S = 0.93$) for oligo(*p*-phenylenevinylene)s^[104c] were found after deposition onto rubbed polymer aligned layers. That implies that the solution-sheared thin-films of **SQd** exhibit a high degree of uniaxial alignment, which can be seen as an explanation for the anisotropy found in the transistor performance. The charge transport within these films seems to be favored along the direction of a J-type packing motif indicated by the red-shift of the absorption maximum. In contrast to this quite perfect alignment of the molecules within the active layer, spin-coated thin-films show no dependence of the UV/Vis/NIR absorption spectra upon variation of the polarization of the incident light (Figure 32b). This means a random orientation of the transition dipole moments indicating less order in the spin-coated

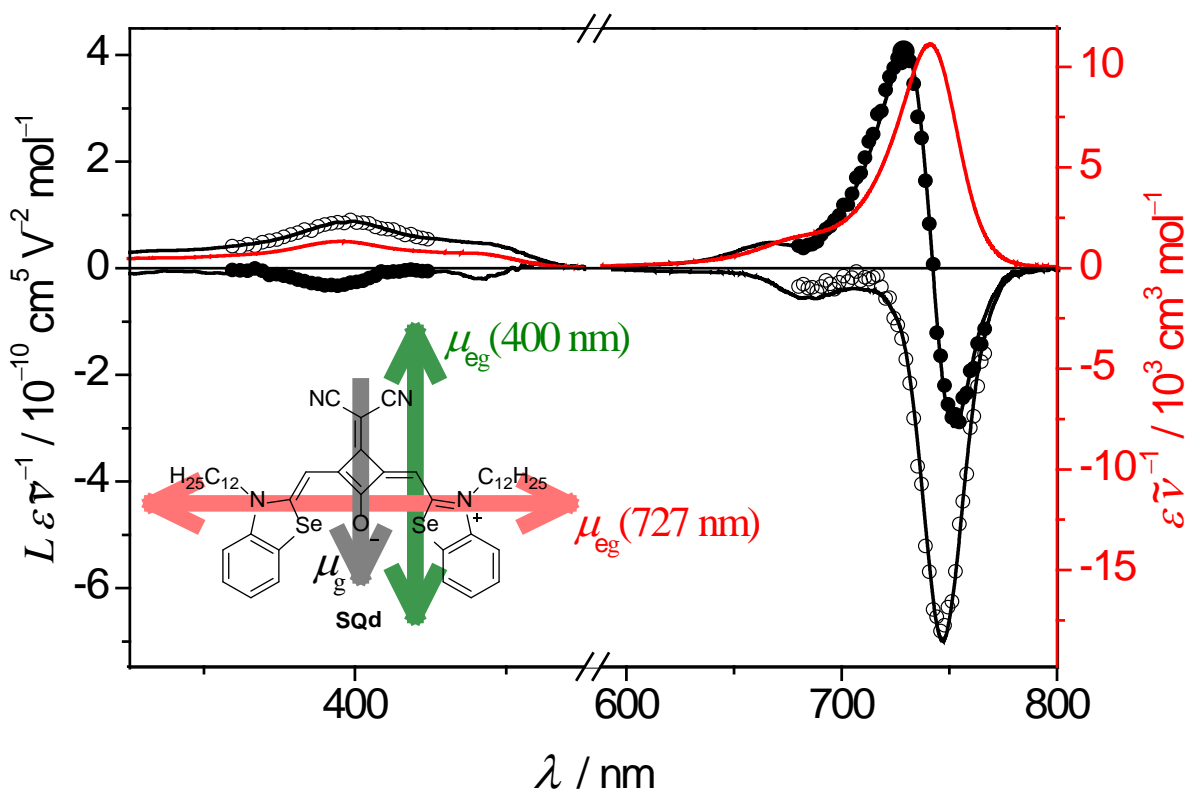


Figure 33. Optical ($\epsilon \tilde{\nu}^{-1}$, right scale, solid line in red) and electro-optical ($L \epsilon \tilde{\nu}^{-1}$, left scale; $\varphi = 0^\circ$, open symbols; $\varphi = 90^\circ$, solid symbols; multi-linear regression, solid black line) absorption spectra of squaraine dye **SQd**. Solvent: 1,4-dioxane, $T = 298$ K. The orientation of μ_g , $\mu_{eg}(400 \text{ nm})$ and $\mu_{eg}(727 \text{ nm})$ is depicted for the structure of the squaraine **SQd** by arrows.

films. Hence, lower transistor performance can be assumed due to the isotropic orientation of the molecules in the thin-film, which has indeed been observed (cf. Chapter 3.1).

A permanent dipole moment is given for acceptor-substituted squaraines (such as **SQa-f**) which is induced by the C_{2v} symmetry of the molecules. Electro-optical absorption measurements (EOAM)^[105] were performed in 1,4-dioxane to estimate the dipolar character of **SQd**. The results of the experiment are depicted in Figure 33.^[106] A decrease of the absorption ($L \epsilon = (\epsilon^E - \epsilon) \mathbf{E}^{-2}$) of light polarized parallel to the electric field ($\varphi = 0^\circ$; open symbols in Figure 33) is determined for the long wavelength band with a maximum at 727 nm. The opposite observation is made for the band located around 400 nm, where a positive signal is found for $\varphi = 0^\circ$. Additionally, this band shows a decrease in absorption in the case of perpendicular polarization of the incident light ($\varphi = 90^\circ$; solid symbols in Figure 33) and, thus, overall positive electrochromism. The sigmoidal shape for the long wavelength band for $\varphi = 90^\circ$ originates from the large negative dipole difference (-11.2 D) confirming positive electrochromism. Taking molecular symmetry into account, the transition dipole moments of the bands at around 400 nm and 727 nm must be perpendicular polarized with respect to each other. Furthermore, the transition dipole moment related to the short

wavelength band, $\mu_{eg}(400\text{ nm})$, has to be oriented along the C_2 -axis and this direction is coextensive with the ground state dipole moment μ_g pointing from the dicyano group to the oxygen atom of the squaric acid, as schematically depicted in Figure 33. Considering the C_{2v} symmetry of **SQd**, one can conclude that the transition dipole moment of the band with a maximum at 727 nm, $\mu_{eg}(727\text{ nm})$, has to be located in the σ_h mirror plane and oriented along the long molecular axis. As recently reported for a structural similar squaraine,^[107] the origin of the band with a maximum at 727 nm can be attributed to a transition from the HOMO to the LUMO level, whereas the band in the region around 400 nm relates to a higher energy transition from the HOMO–1 to the LUMO level. Moreover, the evaluation of the EOA data gives a ground state dipole moment of 6.0 D meaning that **SQd** is a molecule with medium dipolar character.

It has become clear from the absorption spectroscopy that the transition dipole moment of the long wavelength band has to be aligned parallel to the direction of shearing, whereas the one of the band in the region around 400 nm has to be oriented perpendicularly. Assuming that the transition dipole moments in the case of monomers in solution and of J-type excitonic coupled molecules in thin-films have the same alignment,^[98,108] it can be concluded that the orientation of the C_2 axis of **SQd** has to be perpendicular to the direction of shearing.

3.2.5 X-Ray Analysis of the Thin-Films and Crystal Structure of **SQc**

Single crystals could only be grown for squaraine dye **SQc**, while attempts to crystallize all the other squaraines were not successful. The single crystals of **SQc** were subjected to X-ray single crystal structure determination. The structure and the most prominent packing features are depicted in Figure 34. The packing parallel to the (301) plane (Figure 34a) involves intermolecular CN–Se interactions (N–Se-distance 3.07 Å) with alternating ribbons of molecules that are separated from one another by a distance of 14.3 Å due to self-segregation induced by the alkyl-chains (see Figure 34b). Such CN–Se interactions have been reported before by Davis *et al.*, who found N–Se-distances between 3.05 and 3.58 Å for diselenadiazolyl dimers.^[110] Analysis of the molecular packing reveals also that the direction of the ground state dipole moments (they are depicted by a black arrow in Figure 34a) is alternated from ribbon to ribbon and hence in total the dipole moment is cancelled. The view onto the (010) plane (Figure 34b) reveals furthermore an antiparallel slipped packing arrangement in π -stacks with a π – π -distance of 3.38 Å. In such arrangement, the transition dipole moments, which are parallel to the molecules' long axis (cf. Chapter 3.2.4), are oblique with respect to the (100) plane and show a slip angle θ of about 29°. According to the

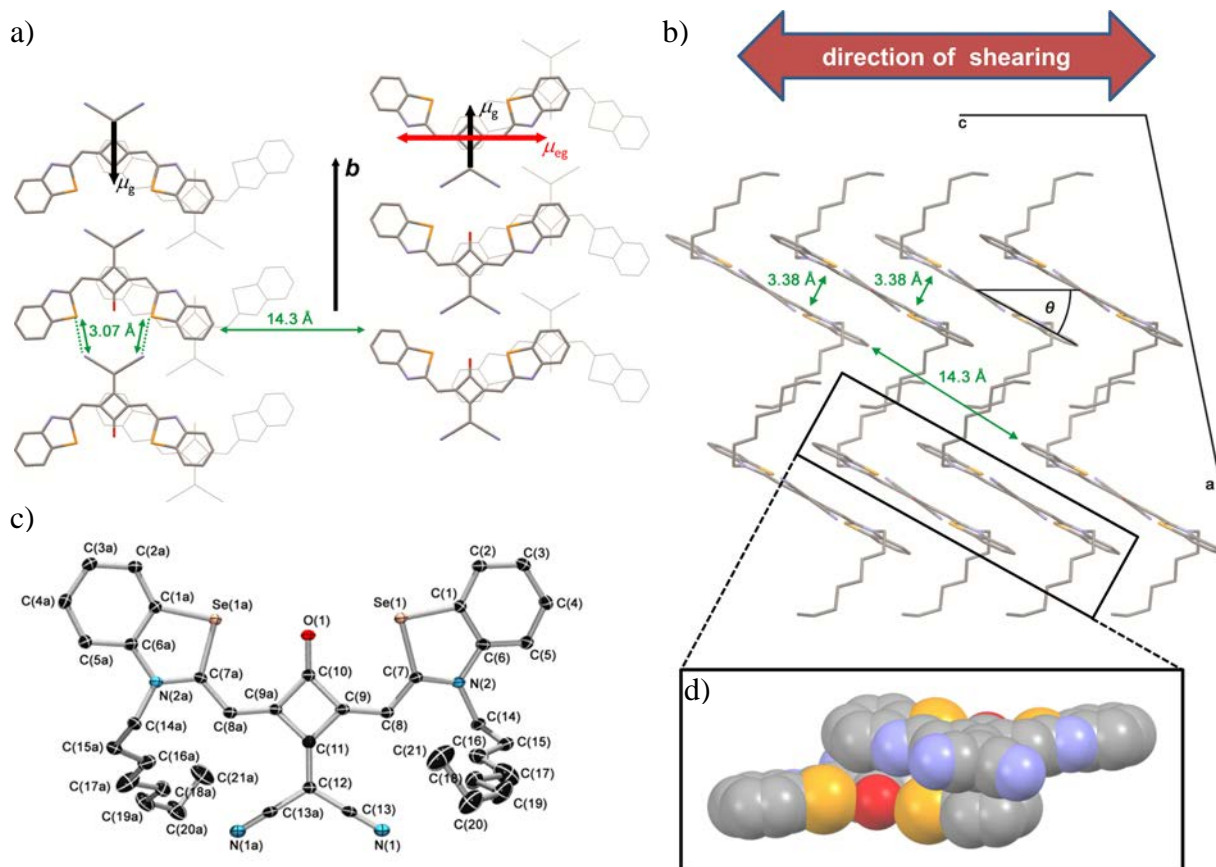


Figure 34. Packing arrangement parallel to the (301) plane with the ground state and transition dipole moments indicated by arrows (a), view onto the (010) plane with definition of the slip angle θ (b), molecular structure in the crystal with numbering of the atoms (c), and ball-and-stick-model of a centrosymmetric dimer (d) of squaraine dye **SQc**. Hydrogen atoms (a-d), the octyl chains (a,d) and their disorder (b,c) are omitted for clarity. Thermal ellipsoids are set at 50 % probability.

excitonic coupling theory of Kasha and co-workers,^[98,108] a displacement of the dyes with $\theta < 54.7^\circ$ induces a J-type excitonic coupling. In Figure 34d the packing of the two **SQc** molecules within a centrosymmetric dimeric unit is depicted. Because the dipole moments of the two molecules point to opposite directions efficient cancellation of the molecular ground state dipole moments is found. Another annihilation is found for the packing arrangement shown in Figure 34a. On the basis of these findings, one can conclude that the overall dipole moment within the crystal is cancelled.

XRD measurements were performed for solution-sheared films of **SQd**. The specular scans (2θ scans) for spin-coated and solution-sheared OFET devices on Si/SiO₂, Si/SiO₂/HMDS and quartz substrates as well as respective rocking curves (RCs) for the solution-sheared samples are shown in Figure 35.^[111] No Bragg reflexes were observed for an as cast sample of **SQd**, which was prepared by spin coating on Si/SiO₂/HMDS substrates (Figure 35a). For those films annealed prior to the X-ray diffraction experiment an increased crystallinity in comparison to the as cast films was indicated by sharp reflexes in the respective specular scan. Solution-sheared films exhibited an even higher degree of

crystallinity, which is evident from the observation of further reflexes at higher angles. Hence, the increase in OTFT-performance from as cast spin-coated films over annealed ones to thin-films deposited by solution shearing can be attributed to the crystallinity, which rises in the same order. That is, the highest degree of crystallinity and consequently the best transistor performance could be observed for transistor devices processed by solution shearing.

Assuming that the **SQd**-based thin-films crystallize in the same space group as determined for the single crystals of **SQc** ($C2/c$), the observed reflections could be indexed as those arising from the (200), (400), (600) and (800) planes according to the reflection conditions reported for this space group.^[112]

The (200) rocking curves of thin-films deposited on different substrates by solution shearing are depicted in Figure 35c. Their peak widths (full width at half-maximum) are a measure for the angular spread of the orientations of the crystallites. For films deposited by solution shearing on Si/SiO₂ and Si/SiO₂/HMDS substrates, values of 0.02° were determined, whereas peak width increases up to 0.4° for films on quartz substrates. This means that a quite narrow distribution in the molecular orientation exists for the thin-films of **SQd** on each of these substrates. Hence the large-scale crystallinity is quite high, where an increase was found from quartz to HMDS-modified Si/SiO₂ substrates.

The diffraction studies suggest that the crystallites on the quartz substrate are sufficiently well oriented and their spectroscopic studies are therefore a good measure for the semiconductor films on Si/SiO₂ substrates. Because specular XRD scans of films prepared on quartz and on Si/SiO₂ substrates show nearly identical diffraction pattern (Figure 35b), one can assume for OFET devices on Si/SiO₂ the same packing arrangement as on quartz as well as the same anisotropy, which was evidenced by polarized UV/Vis/NIR spectroscopy for thin-films on quartz substrates with a dichroic ratio D of 5.9 (Figure 32). Further support was provided by AFM studies of films prepared on quartz and Si/SiO₂ substrates (Figure 31b and f) revealing a similar morphology for both. It is known from the EOAM experiment associated with the optical spectroscopy with linearly polarized light, that the molecular axis connecting both benzoselenazol units is aligned parallel to the direction of the shearing. With the further assumption of a packing in the thin-films of **SQd**-based transistor devices similar to the arrangement of the molecules in the crystal structure of **SQc**, the crystallographic c -axis has to be oriented parallel to the direction of shearing, while the (100) plane is parallel and, thus, the a -axis is perpendicular to the substrate surface. The latter can be deduced from analysis of the (200) reflex of the solution-sheared thin-film of **SQd** on Si/SiO₂/HMDS (Figure 35a) yielding a layer spacing of 17.1 Å and, thus, a unit cell

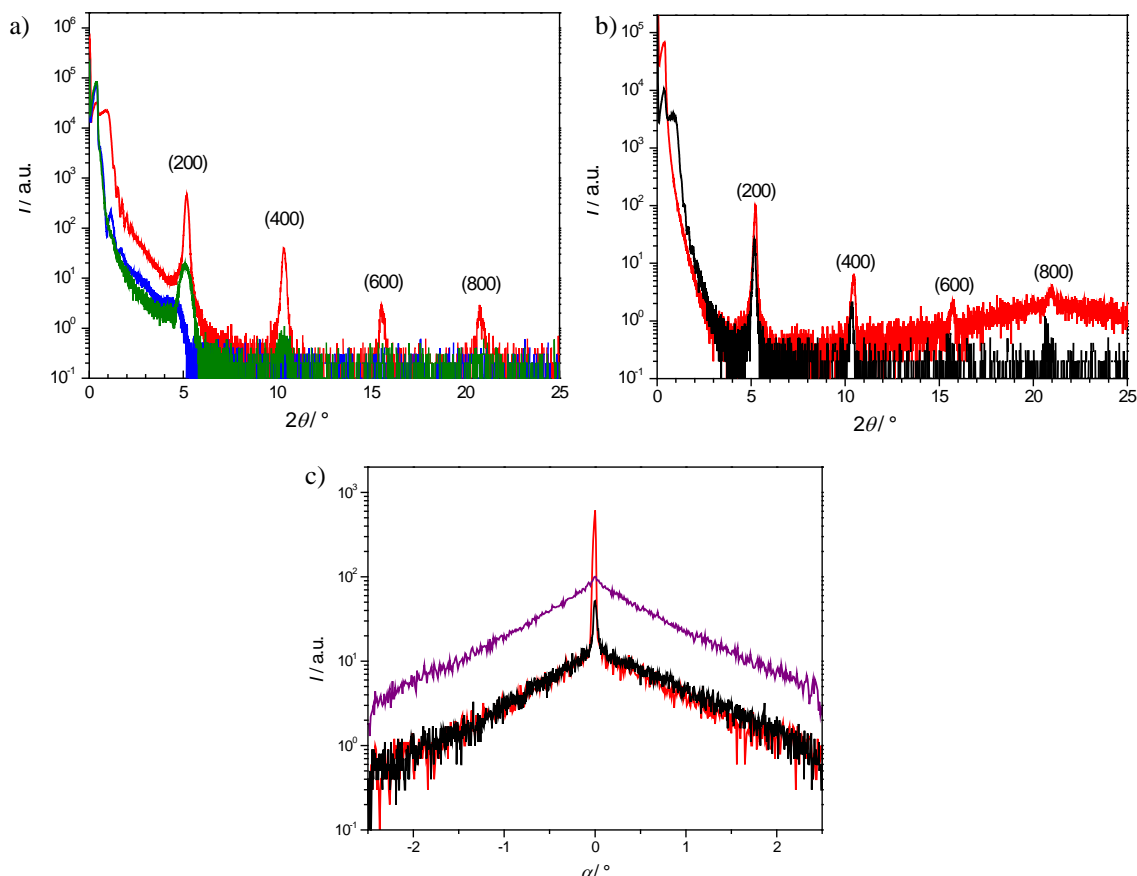


Figure 35. Specular XRD scans of thin-films of **SQd** prepared by a) solution shearing (red) and spin coating (blue: as cast, green: after annealing for 10 minutes at 130 °C) on Si/SiO₂/HMDS and b) solution shearing on Si/SiO₂ (black) and quartz substrates (purple). c) (200) RCs of solution-sheared thin-films of **SQd** on Si/SiO₂ (black), Si/SiO₂/HMDS (red) and quartz substrates (purple).

parameter a of 34.2 Å. This value is slightly higher as compared to the cell parameter a of the crystal structure of **SQc** (27.6 Å), which can be explained by the elongation of the alkyl chain from eight to twelve carbon atoms leading to an increase of the cell parameters with only minor influence on the packing arrangement. Additional support comes from the AFM cross section analysis of solution-sheared thin-films of **SQd** on Si/SiO₂/HMDS substrates, from which a layer height of 1.5 to 1.7 nm was calculated. This is about half the value of the unit cell parameter a determined by the XRD experiments, meaning two monomolecular layers per unit cell along the a -direction. That implies that after every second monomolecular layer the packing motif is repeated, which is in good accordance with the crystal data of **SQc**.^[113]

In conclusion, the XRD, AFM and UV/Vis/NIR data point to an orientation of the crystallographic c -axis parallel to the shearing direction and the (010) plane being perpendicular to the substrate surface. Accordingly, percolation pathways for charge carriers in the crystallographic c -direction are provided by J-type π -stacking, while packing arrangement driven by CN–Se interactions facilitates decent charge transport in the

b-direction. Hence, efficient two-dimensional charge-transport is possible parallel to the (100) plane and, consequently, parallel to the substrate surface, whereas the *c*-direction should be the more favored one. This is in good agreement with the observed anisotropy in OFET-performance with higher charge carrier mobilities parallel to the shearing direction (*c*-axis) as compared to lower but still remarkable values for devices with perpendicular orientation (*b*-axis).

With regard to the Bässler model (see Chapter 2.1), which predicts low charge carrier mobilities for molecules exhibiting dipole moments, the high transistor performance of the dipolar squaraines is surprising. However, the ground state dipole moments are annihilated due to an alternating packing arrangement (see Figure 34a, b and d) and hence the possibility for effective charge transport is facilitated. Support for this idea was recently given by Huang *et al.*^[88] They reported on hole mobilities of up to $0.18 \text{ cm}^2 \text{ V}^{-1} \text{ s}^{-1}$ for vacuum-deposited devices of a highly dipolar merocyanine, where also an antiparallel packing arrangement of the molecules leads to molecular layers that lack bipolarity.

3.3 Squaraine-Based Thin-Film Transistors – Deposition by Vacuum Sublimation

3.3.1 Performance of the Transistor Devices

Processing the active layers of OTFTs by solution-based methods (see Chapters 3.1 and 3.2) gave proof for the potential of squaraine dyes **SQa-f** in organic electronic applications. As vacuum deposition facilitates a much better control of the film morphology by adjusting the deposition conditions such as deposition rate and substrate temperature (see Chapter 2.3 and 2.4), it appeared promising to process squaraine semiconductor films also by sublimation. Unfortunately, compounds **SQa**, **SQc** and **SQd** decomposed during evaporation, while a stable deposition rate and the formation of a thin-film on the transistor substrates were only obtained for **SQb** bearing *n*-butyl chains. Thermogravimetric analysis (TGA, Figure 36) confirmed that the above results are consequence of low stability of **SQa**, **SQc** and **SQd**. It is evident from this data that decomposition of **SQa** already starts at around 200 °C, which is further supported by the results from differential scanning calorimetry, where no melting point but an exothermic decomposition from about 270 °C is observed (inset of Figure 36). All other squaraines exhibit transitions from solid to liquid phase with a thermal stability of the melt of up to 295 °C for octyl- and dodecyl-substituted derivatives **SQc** and **SQd**. The only sublimable compound **SQb** exhibits the best thermal stability within this series and does

not start to decompose up to an approximate temperature of 325 °C (see TGA plot in Figure 36), as confirmed by DSC analysis.

OTFTs of **SQb** were built by sublimation of 30 nm thick films onto Si/SiO₂ substrates under high vacuum. These substrates were modified by different SAMs prior to deposition of the active layer to vary the surface energy, which is one of the parameters directly influencing the arrangement of the molecules and transistor characteristics (see Chapters 2.3 and 2.4). The deposition rate was adjusted to approximately 1 nm min⁻¹ and the substrate temperature set to approximately 180 °C. Keeping the substrate during the evaporation process at an elevated temperature provides the opportunity for reorganization of the molecules, which drives them to adopt an optimum arrangement on the substrate and to establish large grains. Bottom-gate, top-contact configured transistor devices were accomplished by deposition of the gold source and drain electrodes through shadow masks. Such OTFT devices exhibited an average p-type charge carrier mobility of only 0.011 cm² V⁻¹ s⁻¹ with a poor on/off ratio of the drain current (10¹) and a high threshold voltage of nearly 20 V. In comparison to spin-coated and

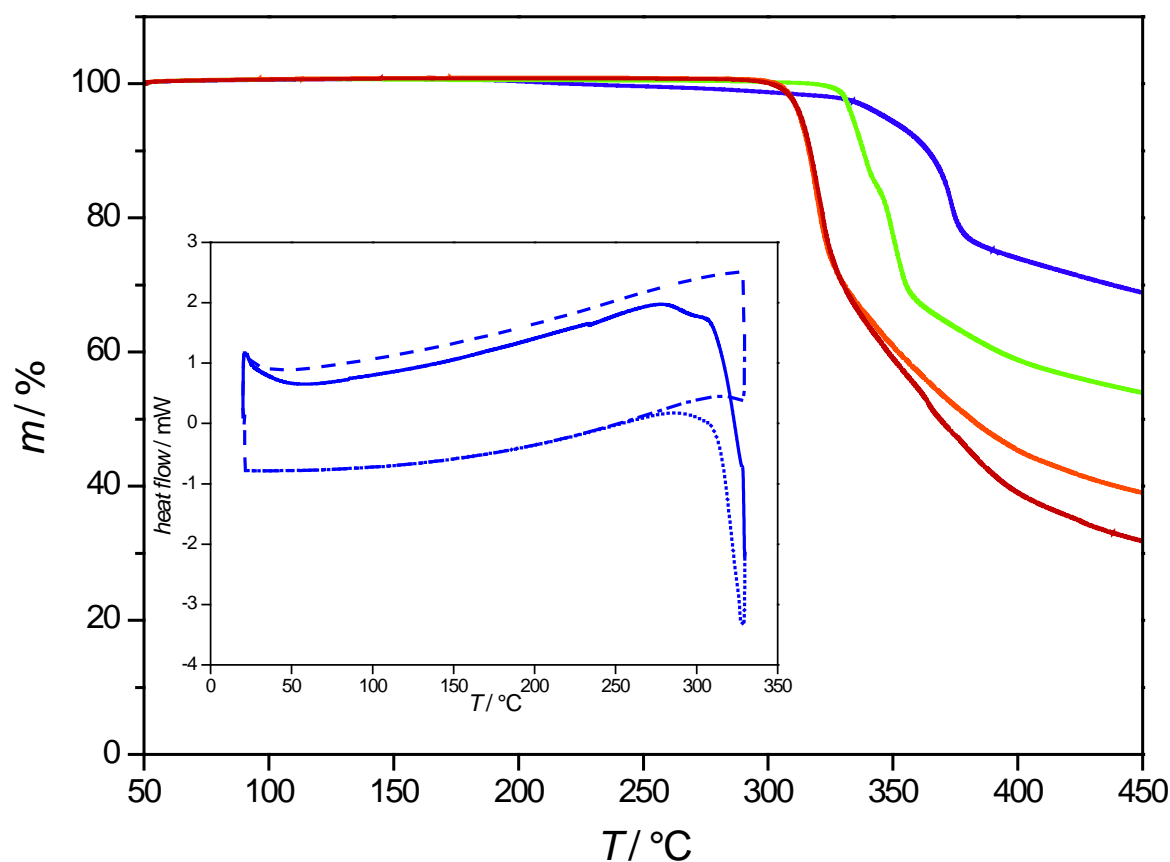


Figure 36. Comparison of the TGA traces of **SQa** (blue), **SQb** (green), **SQc** (orange) and **SQd** (red). The measurements were performed with ceramic pans under a flow of N₂. The inset shows the DSC thermogram of **SQa** (1st heating: solid; 1st cooling: dotted; 2nd heating: dashed; 2nd cooling: dash-dot).

Table 9. Summary of mean electrical properties (averaged over at least five devices) for OTFTs of squaraine dye **SQb** prepared by vapor deposition on different substrate/SAM combinations.

Substrate	SAM	$\bar{\mu}_p /$ $\text{cm}^2 \text{V}^{-1} \text{s}^{-1}$	$I_{\text{on}}^-/I_{\text{off}}^-$	$V_{\text{th}} /$ V
Si/SiO ₂	---	0.011±0.003	10 ¹	18±2
Si/SiO ₂	OTES	0.0036±0.0040	10 ²	8.2±0.9
Si/SiO ₂	HMDS	0.036±0.005	10 ²	14±2
Si/SiO ₂ /AlO _x	FOPA	0.23±0.02	10 ¹	30±1
Si/SiO ₂ /AlO _x	TPA	1.2±0.1	10 ³	-1.2±0.1

subsequently annealed thin-films, μ_p of the vacuum-deposited ones is an order of magnitude higher, while the on/off ratio and the threshold voltage are not affected.

The OTFT performance of vacuum-deposited **SQb** transistor devices is summarized in Table 9. As can be easily seen from this set of data, the introduction of a HMDS or OTES SAM did not affect the OFET performance in an essential way: deposition of **SQb** onto HMDS-modified substrates led to only a slightly higher mobility ($0.036 \text{ cm}^2 \text{ V}^{-1} \text{ s}^{-1}$), while for OTES even a decrease in the range of one order of magnitude was observed. However, these two substrate modifications had a positive impact on the on/off ratio, which rose up to a value of 10^2 . A dramatic increase to hole mobilities of $0.23 \text{ cm}^2 \text{ V}^{-1} \text{ s}^{-1}$ ($V_{\text{th}} = 30 \text{ V}$) and of $1.3 \text{ cm}^2 \text{ V}^{-1} \text{ s}^{-1}$ ($V_{\text{th}} = -1.2 \text{ V}$) could finally be reached by using FOPA and, respectively, TPA-modified Si/SiO₂/AlO_x substrates. It is noteworthy that the threshold voltage for transistors built on TPA SAM is low leading to a reduced power consumption in the ‘off’-state, which is desirable for operation of mobile devices. Representative output and transfer characteristics of an OFET exhibiting such high charge carrier mobility are depicted in Figure 37. As with the solution-processed squaraine-based devices, a quite high I_{off} ($\sim 10^{-8} \text{ A}$; for FOPA even $\sim 10^{-6} \text{ A}$; see Figure 37b) was measured for these OTFTs resulting also in low on/off ratios between 10^1 (for bare substrates) and 10^3 (for TPA-modified substrates). These devices never reach the ‘‘off’’-state, which may be ascribed to transistor operation at ambient conditions and therefore to oxidation of the electron-rich squaraine molecules as discussed before for the solution-processed thin-films (Chapters 3.1 and 3.2). Furthermore, the highly electronegative FOPA SAM may lead to an extraction of electrons

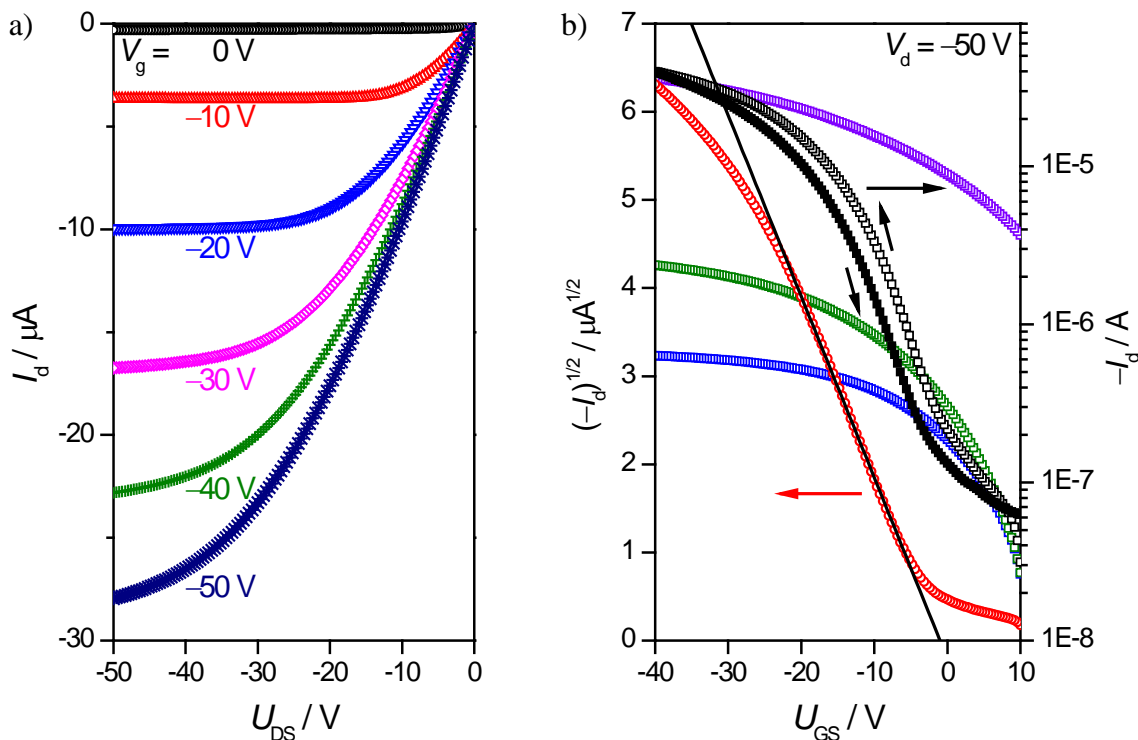


Figure 37. Output (a) and transfer (b) characteristics of a bottom-gate, top-contact OTFT of squaraine dye **SQb** on Si/SiO₂/AlO_x/TPA measured in air. The respective transfer curves of such a device are colored black and red in b), while the forward measured transfer-characteristics of devices on Si/SiO₂ substrates (blue), Si/SiO₂/HMDS substrates (green) and Si/SiO₂/AlO_x/FOPA substrates (purple) are also shown.

from the semiconductor film at the interface, which may account for the even higher off current of this substrate. Additionally, it is noteworthy that the transistor characteristics of the vacuum-deposited devices show low standard deviations, while for solution-deposited devices the determined values were more widespread.

3.3.2 Spectroscopic and AFM Studies of the Thin-Films

It is common knowledge that vacuum deposition can provide higher charge carrier mobilities than spin coating due to more ordered films with higher degree of crystallinity. The morphology of the vapor-deposited thin-films of **SQb** on all substrates used for transistor fabrication has been investigated by AFM and the resulting images are depicted in Figure 38. Large crystalline domains are observed for films on OTES-modified substrates, in which the crystallites are isolated from one another hindering the efficient charge transport (Figure 38b). As a result, only a moderate performance of devices based on such films was measured. Untreated Si/SiO₂ substrates (Figure 38a) and HMDS-modified ones (Figure 38c) show similar film morphologies, and the respective OTFTs exhibit almost identical charge carrier mobilities in the range of 0.01 cm² V⁻¹ s⁻¹. These films feature a rough surface with irregular structures distributed all over the substrate. The morphology of thin-films deposited on

Si/SiO₂/AlO_x/FOPA (Figure 38d) is much more homogeneous and large domains with few grain boundaries are observed leading to enhanced charge transport with approximately one order of magnitude higher hole mobilities. Finally, films on Si/SiO₂/AlO_x/TPA (Figure 38e and f) feature the largest domains of this series together with the highest charge carrier mobility of 1.3 cm² V⁻¹ s⁻¹. The surface of the domains features terrace-like structures of a height of 1.5 to 1.9 nm for each layer, which is in the range of the values found for solution-sheared films of **SQd** (1.5 to 1.7 nm, see Chapter 3.2.4). According to the discussion concerning the correlation of the results from X-ray diffraction, spectroscopic and AFM studies (see Chapter 3.2.5), the molecules in the vacuum-deposited film presumably adopt a packing arrangement similar to that assumed for solution-sheared thin-films giving rise to an excellent transistor performance.

Further support for this hypothesis was extracted from the comparative spectroscopic study of **SQb**-based thin-films on miscellaneous substrates and a solution in chloroform. UV/Vis/NIR spectra of a vacuum-deposited thin-film and a spin-coated and subsequently annealed one on quartz substrates are depicted in Figure 39. As discussed in Chapter 3.1, similar morphologies are quite likely for thin-films on Si/SiO₂ and quartz substrates, which

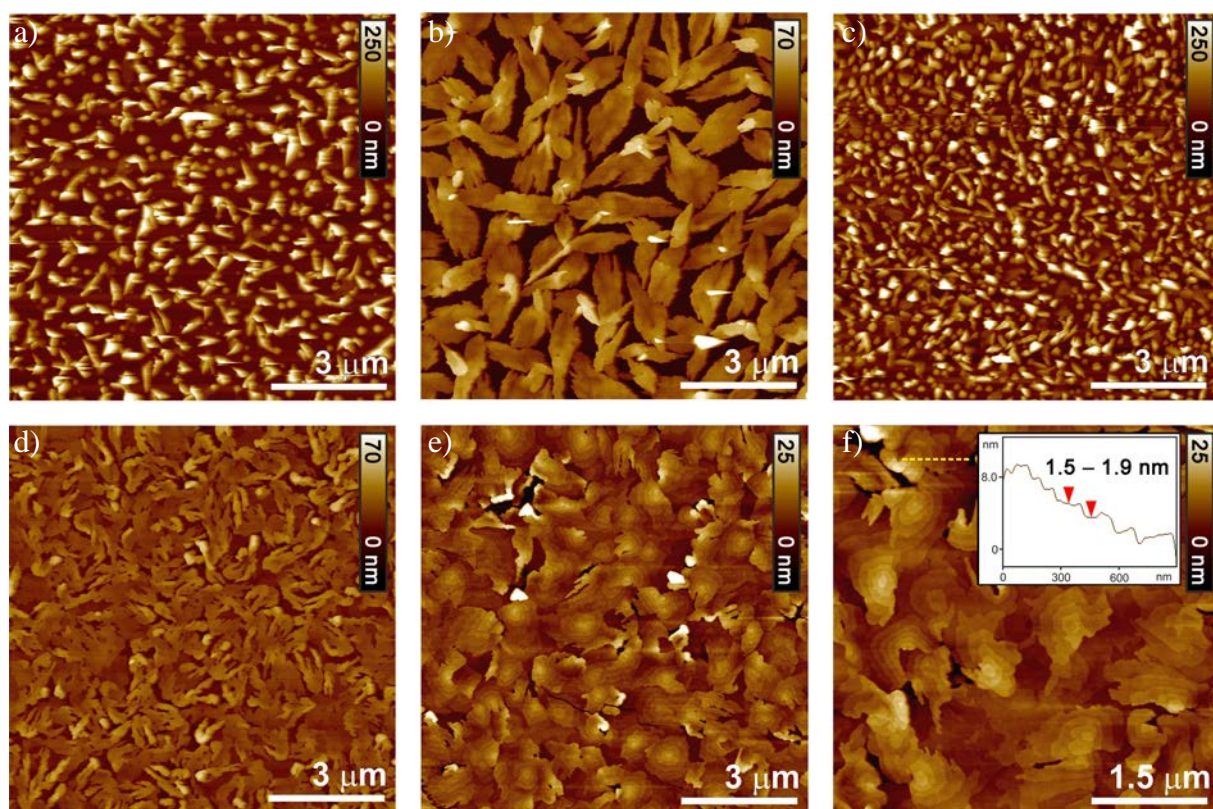


Figure 38. AFM topography images of a thin-film prepared by vapor deposition of squaraine dye **SQb** on Si/SiO₂ (a), Si/SiO₂/OTES (b), Si/SiO₂/HMDS (c), Si/SiO₂/AlO_x/FOPA (d), Si/SiO₂/AlO_x/TPA (e,f) substrates. The inset in f) shows the cross section analysis along the yellow dashed line.

makes spectroscopic studies of films on quartz a useful tool for gaining information about the packing arrangement of the semiconductor molecules in the active layer. Studying thin-films on quartz substrates was necessary by this devious route because direct measurement of the thin-film absorption spectra on Si/SiO₂ substrates using reflection mode was not possible due to the low reflectivity. With the introduction of a SAM at the interface between the semiconductor layer and the Si/SiO₂, the surface energy changes and the spectra are no longer comparable to those of thin-films on quartz. Even Si/SiO₂/AlO_x/TPA substrates suffer from this disadvantage, but upon deposition of the active layer on high reflective Si/Al/AlO_x/TPA, the thin-film spectra could be recorded. The only difference of these two substrates is the composition and thickness of the dielectric layer, where the AlO_x surface is in both cases covered by a self-assembled monolayer of TPA. Thus, identical surface energies can be assumed and similar film growth is quite likely. It was possible to calculate the absorption of such thin-films measured by applying the theory of Kubelka and Munk to the spectra recorded in reflection mode.^[114]

A bathochromic shift of the absorption maximum with respect to the spectrum in solution is accompanied by a band broadening and the appearance of a hypsochromic shoulder for all thin-film samples (Figure 39). Thin-films of **SQb** on Si/Al/AlO_x/TPA substrates exhibit a

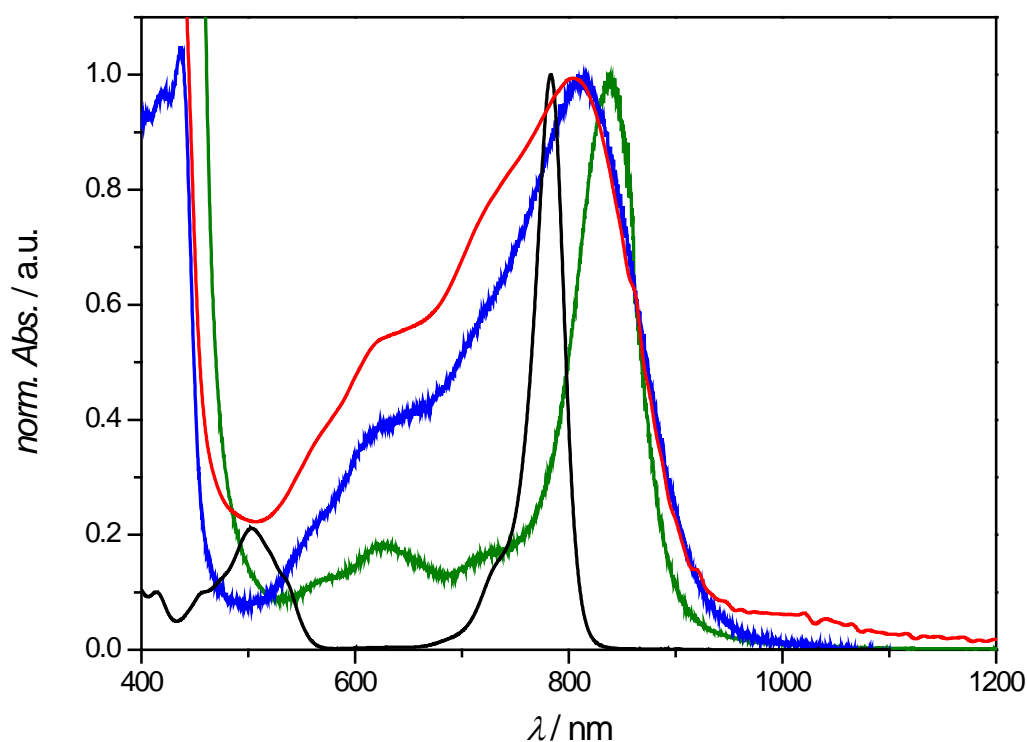


Figure 39. Normalized UV/Vis/NIR absorption spectra of squaraine dye **SQb** in chloroform (black), a spin-coated and annealed thin-film on quartz (blue) and vapor deposited thin-films on quartz (red) and Si/Al/AlO_x/TPA (green), respectively.

much sharper band with a larger bathochromic shift as it could be observed for the films on quartz. This red-shift indicates a J-type coupling of the transition dipole moments in these thin-films, which is similar to the spectroscopic behavior of the active layers of solution-deposited OTFTs (see Chapters 3.1 and 3.2). The much sharper and more red-shifted absorption maximum of the film on TPA SAM may originate from a stronger excitonic coupling with less disorder, while the excitonic states of films on quartz are less strongly coupled and exhibit a higher degree of disorder. The hypsochromic bands indicate that also the transitions from the ground to the energetically higher excitonic coupled states are allowed.^[97] These transitions appear to be much less allowed for films on TPA SAM, meaning a higher order within them. This is consistent with the observed charge carrier mobilities: the films on Si/SiO₂ with weaker excitonic coupling and higher degree of disorder give only moderate transistor performance with charge carrier mobilities between 10⁻³ and 10⁻² cm² V⁻¹ s⁻¹. As already supported by the layer height determined by AFM for the **SQb** films on a TPA-modified substrate, a packing arrangement similar to that discussed in Chapter 3.2 seems quite likely due to the spectroscopic results (a strong J-type excitonic coupling and high degree of order). This may be the reason why devices based on such vacuum-deposited films give the best OFET performance within this study, where charge carrier mobilities of up to 1.3 cm² V⁻¹ s⁻¹ have finally been realized. These results equal the performances found for common a-Si:H TFT devices.

CHAPTER 4

—

SUMMARY IN ENGLISH

Whilst the typical high performance organic semiconductor molecules are based on non-polar molecules such as acenes, oligothiophenes or triarylaminines, in this thesis the suitability of dipolar squaraine dyes for organic electronics has been evaluated.

The starting point of this project was the observation that acceptor-substituted squaraines exhibit decent hole transport in not optimized thin-films and quite good photo-currents in bulk heterojunction solar cells.^[7] Hence, the aim of this thesis was to perform a more in-depth investigation of the applicability of acceptor-substituted squaraine dyes for OTFTs. A general screening was first performed by spin coating a set of squaraines with variations in the molecular and electronic structure. A number of molecular structures were explored including variations of alkyl chain length and heteroatoms, where oxygen, sulfur or selenium atoms were introduced at the squaraine core. As expected, these spin-coated films exhibit a low degree of crystallinity accompanied by poor transistor characteristics. Subsequently, squaraines were also deposited by vacuum sublimation and solution shearing onto the substrates in an effort to access highly ordered and crystalline thin-films with adequate transistor characteristics. A setup for the latter method was constructed, optimized and then applied to the squaraines that exhibited the best solubility and performance by spin coating. For one sublimable squaraine derivative OTFT devices were also manufactured by vacuum deposition. Thereby it was additionally made possible to evaluate the OTFT performance of thin-films from solutions with respect to those from sublimation, where the transistor performance is known to be maximized. In the end, the morphology of the films was studied by several methods such as UV/Vis/NIR spectroscopy, AFM and X-Ray experiments and was

related to the observed transistor performance to yield a structure-property relationship for squaraine dyes in OTFT devices.

Chapter 2 first introduces the reader to the fundamentals of TFT operation followed by a brief summary regarding charge transport mechanisms in organic semiconductor materials. Additionally, methods for depositing the active layer of an OTFT are reviewed with the main focus on solution-based techniques. The chapter concludes with a comprehensive overview of small molecule organic semiconductor materials based on organic colorants. Therein, five classes of dyes are discussed in view of their application in the active layers of OTFT devices and the achieved transistor performance.

Chapter 3 deals with the fabrication and characterization of transistor devices based on thin-films of a series of acceptor-substituted squaraine dyes. First of all, thin-films of these dyes that vary in chain length and that bear oxygen, sulfur or selenium at the squaraine core were deposited by the common spin coating method. Thereby it was possible to identify the optimal electronic as well as molecular structure for achieving the highest transistor performance by applying this simple deposition method. It became clear that selenium and sulfur squaraines with dodecyl substituents (**SQd** and **SQe**, respectively) seem to be most promising for solution-processed transistor devices because as cast films of these molecules already yielded moderate charge carrier mobilities reaching values of around $0.01 \text{ cm}^2 \text{ V}^{-1} \text{ s}^{-1}$ at ambient conditions. These initially measured mobilities exceeded the previously reported values for **SQ5d** (see Figure 40) by already one magnitude of order.^[7] The performance could be further improved by annealing of the thin-films under inert atmosphere due to rearrangement of the molecules by thermal activation, with the hole mobilities for squaraines **SQd** and **SQe** approaching $0.1 \text{ cm}^2 \text{ V}^{-1} \text{ s}^{-1}$ (see Figure 40). With these results, the capability of acceptor-substituted squaraines to act as efficient p-type semiconductor materials in OTFT devices becomes clear.

A positive impact on the OTFT performance was expected by employing advanced processing methods such as the solution shearing method for deposition of the active layer, which is known to result in well-oriented and large-scale thin-films.^[27] A setup for this method was first constructed (see Figure 41a), followed by an optimization of the shearing conditions. The dodecyl-substituted selenium, sulfur and oxygen squaraines (**SQd-f**) were selected for deposition in this way due to their excellent solubility and the promising results obtained for spin-coated devices. Anisotropic hole transport behavior with respect to the shearing direction was observed for the transistors based on such thin-films. Three to four

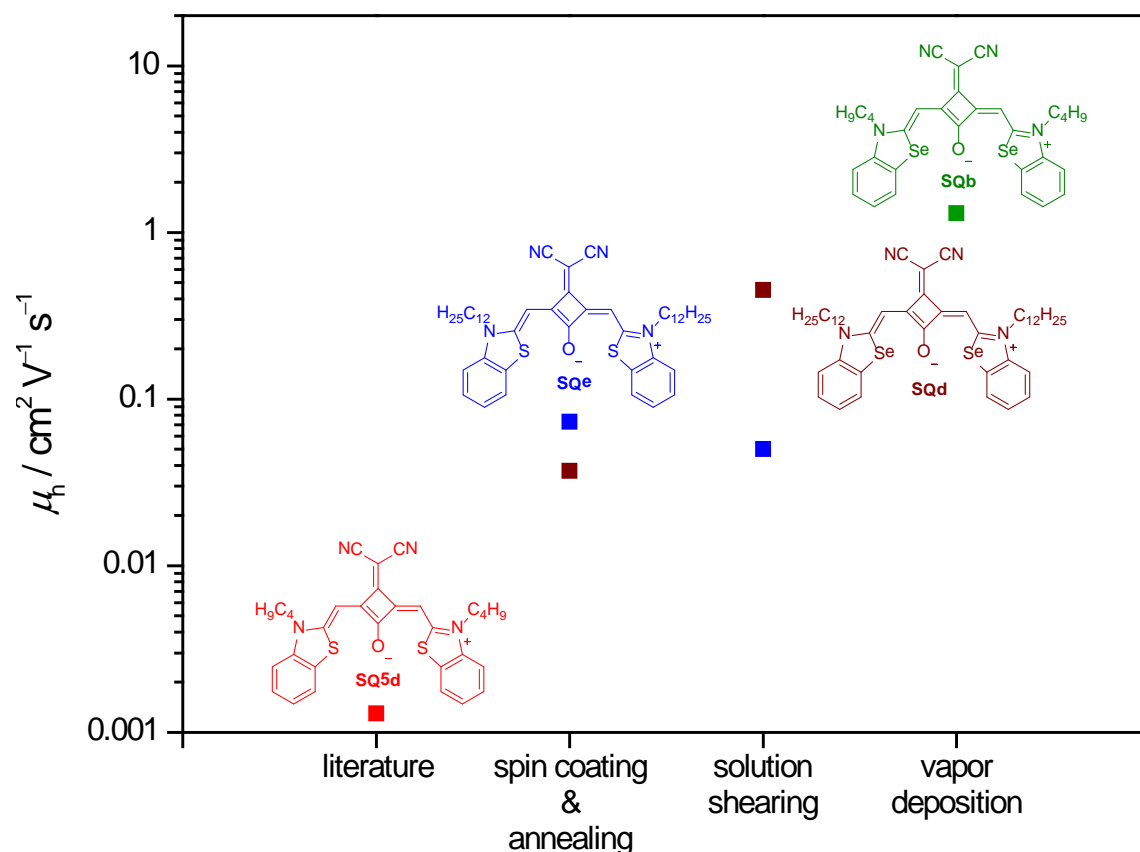


Figure 40. Hole mobilities of squaraine-based OTFT devices of same geometry ($W = 200 \mu\text{m}$, $L = 100 \mu\text{m}$) prepared by various deposition methods. The example for **SQ1d** from literature was spin-coated and annealed ($W = 1 \text{ cm}$, $L = 10 \mu\text{m}$).^[7]

times higher values for the charge carrier mobility were determined for devices with parallel orientation to the shearing direction than for those aligned perpendicularly. The highest average mobility of $0.15 \text{ cm}^2 \text{V}^{-1} \text{s}^{-1}$ could be extracted from the saturation regime of the transfer characteristics of a **SQd**-based transistor device with parallel alignment. Introduction of a self-assembled monolayer of HMDS onto the Si/SiO₂ substrates more than doubled the charge carrier mobility ending up with an average value of $0.37 \text{ cm}^2 \text{V}^{-1} \text{s}^{-1}$ and a peak at $0.45 \text{ cm}^2 \text{V}^{-1} \text{s}^{-1}$ (see Figure 40).

The transistor performance could even be driven to values beyond $1 \text{ cm}^2 \text{V}^{-1} \text{s}^{-1}$ by vacuum deposition of the active layer due to better control of the crystallinity as compared to those films processed from solution-based methods. The sublimable derivative of **SQd** with a shorter alkyl chain, **SQb** was sublimed onto various substrates, whereby a record hole mobility of $1.3 \text{ cm}^2 \text{V}^{-1} \text{s}^{-1}$ was achieved (see Figure 40). These well-performing devices impressively display that judicious selection of the deposition method gives rise to OTFTs based on acceptor-substituted squaraine dyes approaching the performance of those devices that are based on amorphous silicon or of high-performance acene- and oligothiophene-based OTFTs.

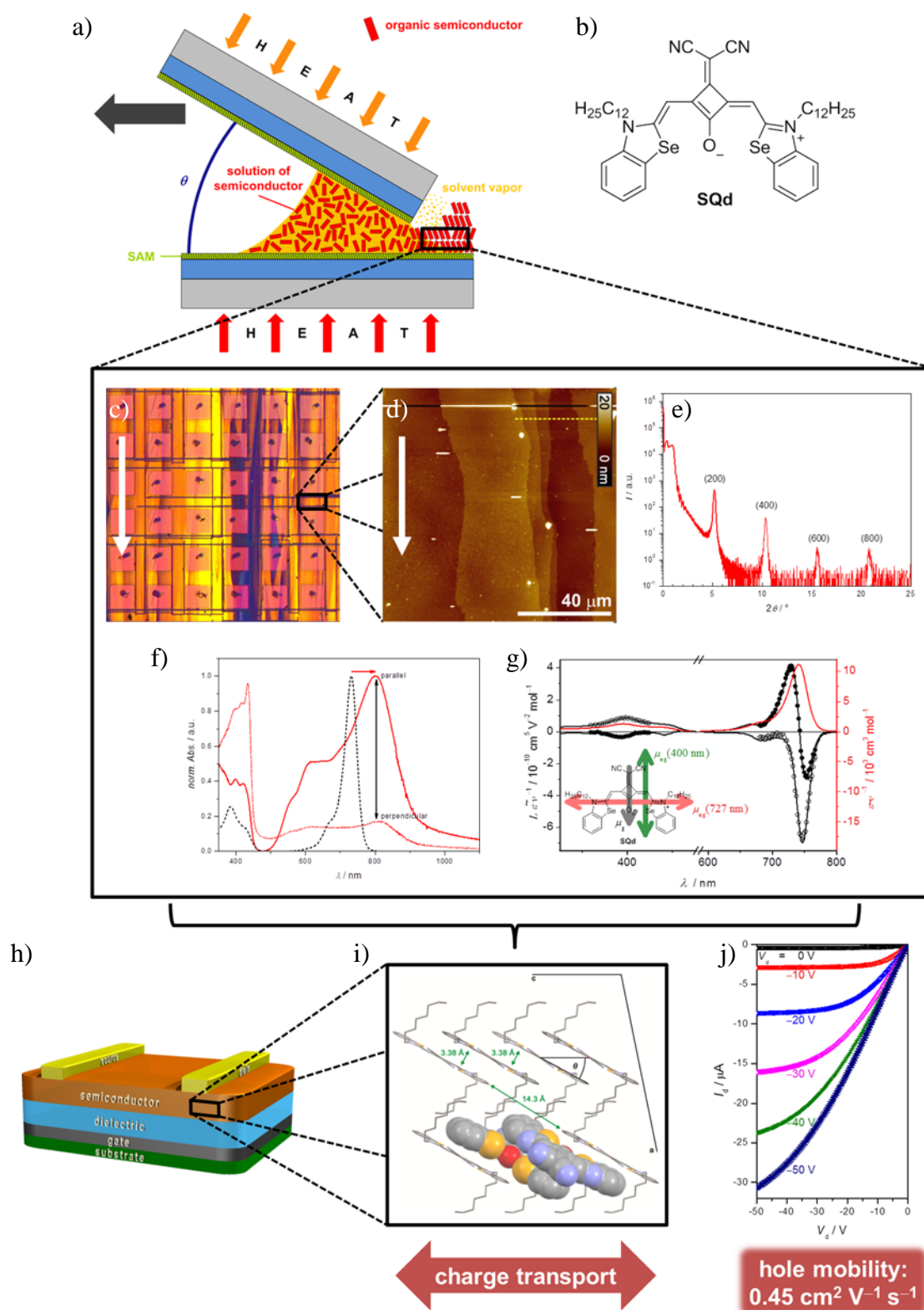


Figure 41. a) Schematic depiction of the solution shearing method. b) Molecular structure of the best-performing solution-processed squaraine **SQd**. c) OPM picture, d) AFM image, e) X-ray diffraction studies and f) UV/VIS/NIR absorption experiments with polarized light of a thin-film of this dye prepared by solution shearing. g) EOAM-experiment yielding the orientation of ground state and transition dipole moments. h) TFT configuration of the studied devices. i) Packing arrangement of **SQc** molecules in the single crystal, which was shown to also be applicable for solution-sheared films of **SQd**, whereas the a -axis is perpendicular to the substrate surface and the c -axis parallel to the direction of charge transport. The J-type packing arrangement is illustrated by two molecules drawn as CPK model. j) Output characteristics of the solution-sheared TFT with the best performance.

Additionally, the morphology of the active layers of these OTFTs and the packing of the molecules therein was investigated in great detail by optical spectroscopy, AFM studies and X-ray experiments. UV/Vis/NIR spectra of squaraine thin-films revealed red-shifted absorption bands compared to spectra recorded for solutions (see Figure 41f). This could be explained by a J-type excitonic-coupled packing arrangement of the molecules, which was found to be the standard motif of all films obtained by the herein studied deposition methods. It became clear from this study that the increase of the charge carrier mobility for spin-coated thin-films upon annealing can be – at least partially – attributed to changes in the molecular packing. Furthermore, AFM investigations for all films were a valuable tool to evaluate the morphology of the films. Upon thermal treatment of spin-coated films a rise of the crystallinity could be observed explaining also the rise in transistor performance as compared to as cast films.

Charge carrier mobility could be further increased and showed an anisotropic behavior with respect to the shearing direction, when depositing the active layer by solution shearing. This could be understood by the high degree of orientation and crystallinity that was evident from the large-scale domains observed not only by optical polarizing microscopy (see Figure 41b) but also by AFM (see Figure 41c). AFM images of vacuum-deposited devices revealed crystallites with terrace-like texture, which seemed to be the cause of the excellent transistor operation. A more detailed study of the packing arrangement of the molecules was carried out for solution-sheared thin-films. The orientation of the transition and ground state dipole moments with respect to the scaffold of the squaraine molecule was derived from EOAM experiments (see Figure 41g). Relating this to the optical anisotropy observed by optical spectroscopy of solution-sheared films with polarized light (see Figure 41f) led to the conclusion that the long molecular axis of the molecules has to be aligned along the direction of shearing. That implies that also the J-type packing motif is oriented parallel to this direction. Whilst taking into account all these results together with the layer spacing derived from X-ray diffraction experiments of the thin-films, it eventually could be concluded that the molecules in the solution-sheared thin-films adopt a packing arrangement similar to that of the crystal structure, where the long molecular axis is aligned parallel to the direction of shearing as depicted in Figure 41i. The determined anisotropy for the charge transport in solution-sheared films as well as the better performance as compared to spin-coated ones likewise can be well-explained by such a packing of the molecules.

In summary, it can be stated that the herein studied set of acceptor-substituted squaraine dyes can be seen as potent candidates for OTFTs. Furthermore, their transistor performance

can be easily tuned to obtain hole mobilities up to $0.45 \text{ cm}^2 \text{ V}^{-1} \text{ s}^{-1}$ from solution and $1.3 \text{ cm}^2 \text{ V}^{-1} \text{ s}^{-1}$ from sublimation by choosing adequate deposition techniques. In the end, a probable structural model derived from studies of the thin-film morphology by methods such as optical spectroscopy, AFM and X-ray even facilitated the clarification of the observed charge transport behavior.

CHAPTER 5

—

SUMMARY IN GERMAN

Nachdem typischerweise unpolare Moleküle wie Acene, Oligothiophene oder Triarylamine als leistungsfähige organische Halbleitermoleküle zum Einsatz kommen, wurden in der vorliegenden Arbeit dipolare Squarainfarbstoffe auf ihre Eignung für organische Elektronikbauteile untersucht.

Als Ausgangspunkt für dieses Projekt diente die Tatsache, dass akzeptorsubstituierte Squaraine bei der Verwendung in nicht optimierten Filmen bereits respektablem Lochtransport sowie in BHJ-Solarzellen recht hohe Fotoströme aufweisen.^[7] Infolgedessen zielte diese Arbeit auf eine tiefere Untersuchung der Eignung von akzeptorsubstituierten Squarainen für OTFT-Bauteile ab. Eine Vorauswahl wurde zunächst anhand einer Reihe von Squarainen getroffen, die sich in ihrer elektronischen und molekularen Struktur unterscheiden und welche mittels Rotationsbeschichtung prozessiert wurden. Durch Variation der Alkylkettenlänge sowie durch Einbringung von Heteroatomen wie Sauerstoff, Schwefel oder Selen in das Squaraingerüst konnte eine Vielzahl verschiedener Molekülstrukturen erhalten und untersucht werden. Erwartungsgemäß wiesen diese mittels Rotationsbeschichtung erhaltenen dünnen Filme einen geringen Grad an Kristallinität auf, was sich in Bauteilen mit geringer Leistung widerspiegelte. Daraufhin wurden die Squaraine durch Vakuumsublimation und durch Scheren aus Lösung auf die Substrate aufgebracht, um höher geordnete und kristalline Dünnschichten mit zufriedenstellender Leistung zu erhalten. Für die letztgenannte Methode wurde eine Apparatur entwickelt, optimiert und im Anschluss zur Prozessierung derjenigen Squaraine eingesetzt, welche die höchste Löslichkeit und nach Rotationsbeschichtung die beste Leistung besaßen. Darüber hinaus konnten OTFT-Bauteile

eines sublimierbaren Squarainderivats durch Abscheidung im Vakuum erhalten werden. Dies erlaubte eine Beurteilung der Transistorleistung von lösungsprozessierten Dünnschichten in Bezug auf die mittels Vakuumverdampfung erhaltenen Filme, welche bekanntermaßen zu OTFT-Bauteile mit der besten Leistung führen. Schließlich wurde die Morphologie der Filme mit Hilfe verschiedener Methoden wie UV/Vis/NIR-Spektroskopie sowie AFM- und Röntgenexperimenten untersucht. Diese Ergebnisse wurden in Relation zu den ermittelten Transistorleistungen gesetzt, womit eine Struktur-Wirkungs-Beziehung für die Anwendung von Squarainfarbstoffen in OTFT-Bauteilen hergestellt werden konnte.

Kapitel 2 führt den Leser zunächst in das Funktionsprinzip von TFTs ein, worauf eine kurze Zusammenfassung von Ladungstransportmechanismen in organischen Halbleitermaterialien folgt. Im Weiteren wird ein Überblick über Abscheidungstechniken für die aktiven Schichten von OTFTs gegeben, wobei der Schwerpunkt auf lösungsbasierten Methoden liegt. Eine umfassende Übersicht über organische Farbstoffe, die als niedermolekulare organische Halbleitermaterialien eingesetzt werden können, schließt dieses Kapitel ab. Dazu werden fünf Farbstoffklassen im Hinblick auf ihre Anwendung in der aktiven Schicht von OTFTs und die damit erzielbare Transistorleistung diskutiert.

Kapitel 3 behandelt die Prozessierung und Charakterisierung von Transistorbauteilen, die auf Dünnschichten einer Serie von akzeptorsubstituierten Squarainfarbstoffen beruhen. Diese Farbstoffe variieren in der Alkylkettenlänge und im Squaraingerüst, welches Heteroatome wie Sauerstoff, Schwefel oder Selen enthält. In einem ersten Schritt wurden Dünnschichten dieser Squaraine mittels der weitverbreiteten Rotationsbeschichtungsmethode auf die Substrate aufgebracht. Diese einfache Abscheidungsmethode erlaubte die Identifizierung der zur besten Transistorleistung führenden elektronischen und molekularen Struktur. Dabei stellte sich heraus, dass dodecylsubstituierte Selen- und Schwefelsquaraine (**SQd** bzw. **SQe**) am vielversprechendsten für lösungsprozessierte Transistorbauteile sind, da für frisch abgeschiedene Filme dieser Moleküle bereits moderate Ladungsträgermobilitäten um $0.01 \text{ cm}^2 \text{ V}^{-1} \text{ s}^{-1}$ an Luft gefunden wurden. Diese anfangs gemessenen Mobilitätswerte übersteigen die zuvor in der Literatur für das Squarain **SQd** genannten Werte (Abbildung 42) um bereits eine Größenordnung.^[7] Die Leistung der Bauteile ließ sich durch das Tempern der Dünnschichten unter inerter Atmosphäre deutlich verbessern, was eine Änderung der Orientierung der Moleküle durch die thermische Aktivierung zur Folge hatte und für die Squarainderivate **SQd** und **SQe** in Lochmobilitäten von nahezu $0.1 \text{ cm}^2 \text{ V}^{-1} \text{ s}^{-1}$ resultierte (Abbildung 42). Diese Ergebnisse zeigen, dass akzeptorsubstituierte Squaraine als effiziente p-Halbleitermaterialien in OTFT-Bauteilen eingesetzt werden können.

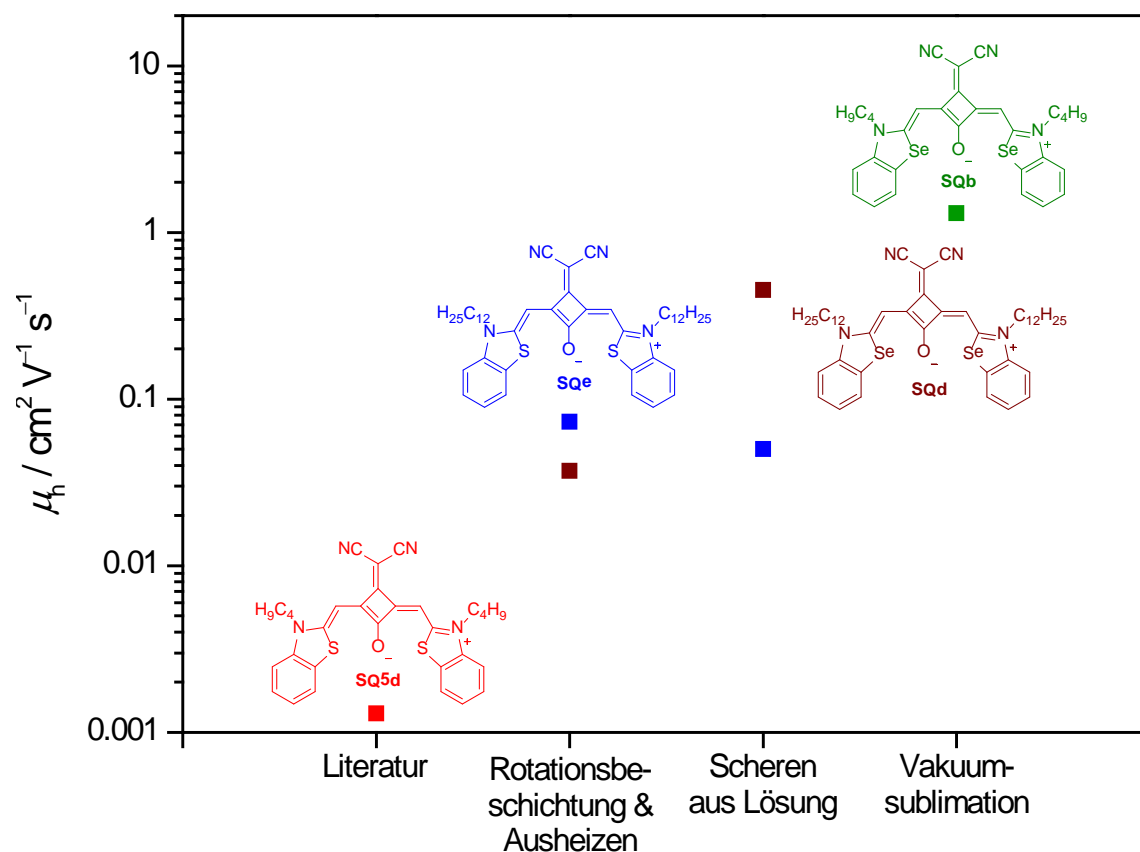


Abbildung 42. Lochmobilitäten von OTFT-Bauteilen, deren aktive Schicht aus Squarainmolekülen besteht und die mittels verschiedener Techniken prozessiert wurden. Die Bauteile weisen dabei alle dieselbe Geometrie auf ($W = 200 \mu\text{m}$, $L = 100 \mu\text{m}$). Das Literaturbeispiel **SQ5d** wurde durch Rotationsbeschichtung abgeschieden und im Anschluss ausgeheizt ($W = 1 \text{ cm}$, $L = 10 \mu\text{m}$).^[7]

Ein positiver Einfluss auf die Transistorleistung lässt sich erwarten, wenn man zur Abscheidung der aktiven Schicht zukunftsweisende Methoden wie das Scheren aus Lösung verwendet, da sich mit diesen hoch geordnete und großflächige Dünnschichten realisieren lassen.^[27] In dieser Arbeit wurde zunächst eine Apparatur für diese Methode konstruiert (Abbildung 43a) und im Anschluss eine Optimierung der Scherbedingungen durchgeführt. Da für die rotationsbeschichteten Transistorbauteile von dodecylsubstituierten Selen-, Schwefel- und Sauerstoffsquarainen (**SQd-f**) eine vielversprechende Transistorleistung gefunden wurde und diese eine ausgezeichnete Löslichkeit aufweisen, wurden die Squaraine **SQd-f** zur Dünnschichtprozessierung mittels Scheren aus Lösung ausgewählt. Für Transistoren, die auf solchen Filmen basieren, konnte anisotroper Ladungstransport in Bezug zur Scherrichtung beobachtet werden. Für Transistorbauteile mit paralleler Ausrichtung zur Scherrichtung wurden drei- bis viermal höhere Ladungsträgermobilitäten bestimmt als für diejenigen, die senkrecht ausgerichtet sind. Die höchste gemittelte Mobilität von $0,15 \text{ cm}^2 \text{V}^{-1} \text{s}^{-1}$ konnte aus dem Sättigungsbereich der Transfercharakteristik eines Transistorbauteils des Squarains **SQd** mit paralleler Orientierung extrahiert werden. Die Einführung einer selbstorganisierenden

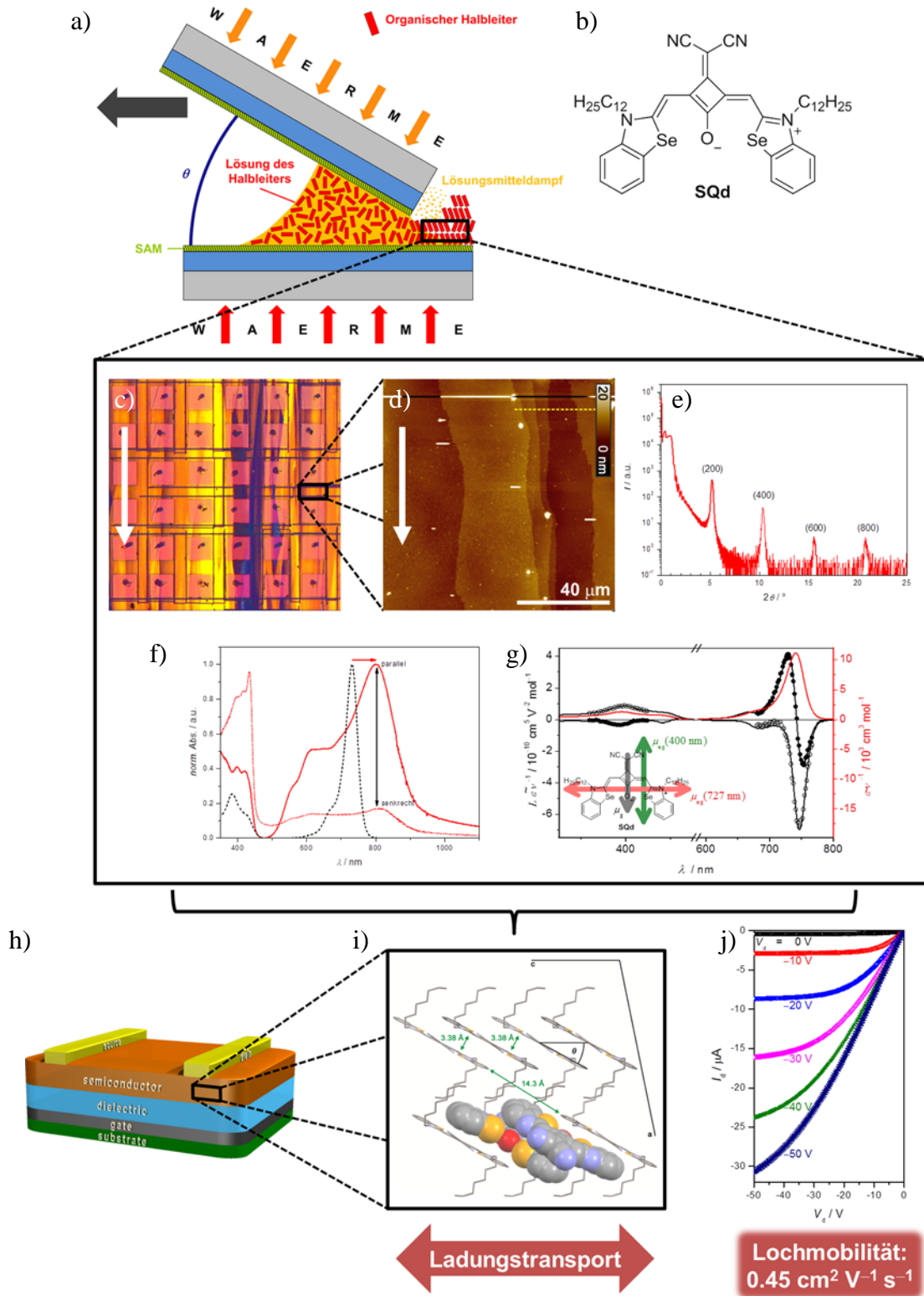


Abbildung 43. a) Schematische Darstellung des Scherens aus Lösung. b) Strukturformel des Squarains **SQd**, dessen lösungsprozessierte Transistoren die höchsten Mobilität zeigen. c) OPM-Aufnahme, d) AFM-Aufnahme, e) Röntgenbeugung und f) UV/VIS/NIR-Absorptionsexperimente mit polarisiertem Licht eines mittels Scherens prozessierten Dünnsfilms von **SQd**. g) EOAM-Experiment, das die Ausrichtung des Grundzustands- und Übergangsdipolmoments liefert. h) Aufbau der untersuchten OTFTs. i) Packung der **SQc**-Moleküle im Einkristall. Eine vergleichbare Anordnung kann für gescherte Filme von **SQd** angenommen werden, wobei die a -Achse senkrecht auf der Substratoberfläche steht und die c -Achse parallel zur Richtung des Ladungstransports orientiert ist. Die einem J-Aggregat ähnliche Packung ist anhand zweier als Kalottenmodell gezeichneter Moleküle dargestellt. j) Ausgangscharakteristik des gescherten Transistors mit der höchsten Mobilität.

HMDS-Monolage auf der Oberfläche des Si/SiO₂-Substrats führte zu mehr als einer Verdoppelung der Ladungsträgermobilität, wobei ein Mittelwert von 0.37 cm² V⁻¹ s⁻¹ und ein Maximalwert von 0.45 cm² V⁻¹ s⁻¹ gemessen wurden (Abbildung 42).

Eine Steigerung der Leistung der Transistoren auf Werte über 1 cm² V⁻¹ s⁻¹ konnte bei der Abscheidung der aktiven Schicht mittels Vakuumsublimation erzielt werden, da sich hierbei die Kristallinität im Vergleich zur Lösungsprozessierung besser kontrollieren lässt. Das sublimierbare **SQd**-Derivat mit kürzerer Alkylkette, **SQb**, wurde mittels Sublimation auf verschiedene Substrate aufgebracht, wobei ein Rekordmobilitätswert von 1.3 cm² V⁻¹ s⁻¹ erreicht werden konnte (Abbildung 42). Diese gut funktionierenden Bauteile zeigen auf beeindruckende Art und Weise, dass eine besonnene Wahl der Abscheidungsmethode den Weg zu OTFT-Bauteilen aus akzeptorsubstituierten Squarainfarbstoffen frei macht und dabei sogar die Leistung derjenigen Bauteile erreicht werden kann, die aus amorphem Silizium oder leistungsfähigen Molekülen wie Acenen oder Oligothiophenen aufgebaut sind.

Des Weiteren wurden die Morphologie der aktiven Schichten solcher OTFT-Bauteile sowie die Packung der Moleküle in diesen Schichten mit Hilfe von optischer Spektroskopie, AFM-Studien und Röntgenexperimenten ausführlich untersucht. UV/Vis/NIR-Spektren der Squaraindünnschichten wiesen im Vergleich zu Lösungsspektren rotverschobene Absorptionsbanden auf (Abbildung 43f). Dies konnte anhand einer Packung der Moleküle vergleichbar mit der in exzitonisch gekoppelten J-Aggregaten erklärt werden. Ein solches Packungsmotiv wurde für alle Filme beobachtet, die mit den in dieser Arbeit verwendeten Methoden prozessiert worden waren. Anhand dieser Studien zeigte sich auch, dass Tempern von rotationsbeschichteten Dünnschichten zu einer Veränderung in der Molekülpackung führt, welche – zumindest teilweise – für die Zunahme der Ladungsträgermobilitäten im Zuge eines solchen Heizprozesses verantwortlich gemacht werden kann. Fernerhin konnte die Morphologie aller Dünnschichten mit Hilfe von AFM-Studien untersucht werden. Nach dem Tempern von mittels Rotationsbeschichtung erhaltenen Dünnschichten konnte ein Anstieg der Kristallinität beobachtet werden. Dies lieferte eine weitere Ursache für die Zunahme der Leistung der Transistoren im Vergleich zu frisch abgeschiedenen Dünnschichten.

Ein weiterer Anstieg der Ladungsträgerbeweglichkeit, für die zudem Anisotropie in Bezug auf die Scherrichtung festgestellt wurde, lies sich durch die Abscheidung der aktiven Schicht mittels Scheren aus Lösung realisieren. Eine Erklärung ist der hohe Orientierungsgrad und die Kristallinität, die sowohl durch optische Polarisationsmikroskopie (Abbildung 43b) als auch AFM-Studien (Abbildung 43c) für großflächige Domänen nachgewiesen werden konnten. Die AFM-Aufnahmen von aufgedampften Dünnschichten zeigten Kristallite mit

terrassenartiger Struktur, welche für die exzellente Leistung solcher Transistoren ursächlich zu sein scheinen. Eine tiefere Untersuchung der Molekülpackung wurde für gescherte Dünnschichten durchgeführt. Aus EOAM-Experimenten (Abbildung 43g) konnte die Orientierung der Übergangs- und Grundzustandsdipolmomente in Bezug auf das molekulare Gerüst der Squaraine hergeleitet werden. Unter Beachtung der optischen Anisotropie, die für gescherte Schichten durch optische Spektroskopie mit polarisiertem Licht nachgewiesen wurde (Abbildung 43f), konnte die Schlussfolgerung gezogen werden, dass die lange Molekülachse in den Dünnschichten parallel zur Schichtorientierung orientiert sein muss. Das bedeutet darüber hinaus, dass das einem J-Aggregat ähnliche Packungsmotiv entlang dieser Richtung orientiert sein muss. Fasst man all diese Ergebnisse zusammen und bezieht den Ebenenabstand mit ein, der aus Röntgenbeugungsexperimenten an den Dünnschichten bestimmt werden kann, so kommt man zu dem Schluss, dass die Moleküle in den gescherten Schichten eine Packungsanordnung einnehmen, welche derjenigen in der Kristallstruktur ähnelt. Dabei ist die lange Molekülachse parallel zur Schichtorientierung orientiert, wie auch in Abbildung 43i dargestellt. Eine derartige Anordnung der Moleküle im Dünnschicht bietet eine Erklärung sowohl für die beobachtete Anisotropie des Ladungstransports in den gescherten Schichten als auch die im Vergleich zu rotationsbeschichteten OTFT-Bauteilen höheren Mobilitätswerte.

Zusammenfassend lässt sich sagen, dass die in dieser Arbeit untersuchten akzeptorsubstituierten Squarainfarbstoffe durchaus als leistungsfähige Kandidaten für den Einsatz in OTFT-Bauteilen angesehen werden können. Ihre Transistorleistung lässt sich durch geeignete Wahl der Abscheidungsmethode dahingehend einstellen, als dass sich Lochmobilitäten von bis zu $0.45 \text{ cm}^2 \text{ V}^{-1} \text{ s}^{-1}$ mittels Lösungsprozessierung und von bis zu $1.3 \text{ cm}^2 \text{ V}^{-1} \text{ s}^{-1}$ mittels Sublimation realisieren lassen. Schließlich ermöglichte die Untersuchung der Dünnschichtmorphologie mit Methoden wie der optischen Spektroskopie, Rasterkraftmikroskopie und Röntgenbeugung die Schlussfolgerung auf ein mutmaßliches Strukturmodell.

CHAPTER 6

—

EXPERIMENTAL SECTION

6.1 Equipment, Methods and Materials

Fluorescence Spectroscopy

The fluorescence spectra were recorded using a PTI QM-4/2003 spectrometer and 10 mm cuvettes (SUPRASIL[®], produced by Hellma). All measurements were performed at ambient conditions and the spectra were corrected against the photomultiplier and the intensity of the lamp. The fluorescence quantum yield Φ_{fl} was calculated from the averaged value of three different excitation wavelengths against Rhodamin 800 (Ethanol, $\Phi_{\text{fl}} = 0.21$) as standard (Acros) using the high dilution method ($Abs. < 0.05$).^[115]

UV/Vis/NIR spectroscopy

The UV/Vis/NIR spectra in solution were recorded against a reference cuvette filled with the respective solvent using a Lambda 950 UV/Vis/NIR spectrometer from Perkin Elmer in 10 mm or 1 mm quartz cuvettes (SUPRASIL[®], produced by Hellma). All measurements were performed with spectroscopic pure solvents (Uvasol, Merck). Thin-films for spectroscopy were obtained by spin coating (30 s, 2000 rpm) of a concentrated squaraine solution in chloroform onto quartz (SUPRASIL[®]) substrates. Solution-sheared thin-films were additionally prepared on quartz (SUPRASIL[®]) and Si/Al/AlO_x/TPA substrates by applying the same conditions as for processing OTFTs on Si/SiO₂ and Si/SiO₂/AlO_x/TPA substrates, respectively. While spectra for films on quartz could be obtained in transmission mode due to transparency, switching to reflection mode was required for non-transparent Si/Al/AlO_x/TPA substrates. A polarizer was used for recording transmission spectra of thin-films on quartz

substrates with linearly polarized light. Recorded reflection spectra were transformed to a qualitative absorption spectrum applying the embedded processing function of the spectrometer software, which performs the transformation according to the theory of Kubelka and Munk.^[114]

Differential scanning calorimetry, DSC

DSC thermograms were recorded using a DSC Q1000 (TA Instruments) at a scan rate of 10 K min⁻¹.

Thermogravimetric analysis, TGA

Thermogravimetric analysis was performed using a Perkin Elmer STA 6000 Simultaneous Thermal Analyzer under nitrogen atmosphere at a heating rate of 10 °C min⁻¹ up to a maximum temperature of 900 °C.

Cyclovoltammetry, CV

CV was performed on a standard commercial electrochemical analyzer (EC epsilon; BAS Instrument, UK) in a three electrode single-compartment cell under argon. Dichloromethane (HPLC grade) was obtained from J. T. Baker and dried over calcium hydride and degassed prior to use. The supporting electrolyte tetrabutylammonium hexafluorophosphate (TBAHFP) was synthesized according to literature,^[116] recrystallized from ethanol/water and dried in high vacuum. The measurements were carried out under exclusion of air and moisture at a concentration of 10⁻⁴ M with ferrocene as internal standard for the calibration of the potential. (Scanning rate: 100 mV s⁻¹; working electrode: Pt disc, Ø 1 mm; reference electrode: Ag/AgCl; auxiliary electrode: Pt wire; concentration of the solution of the electrolyte TBAHFP: 0.1 mol L⁻¹.)

Atomic Force Microscopy, AFM

AFM measurements were performed at ambient conditions with a Bruker AXS MultiMode™ Nanoscope IV System in tapping mode. Silicon cantilevers (OMCL-AC160TS, Olympus) with a resonance frequency of ~ 300 kHz and spring constant of ~ 42 N m⁻¹ were used.

Scanning Electron Microscopy, SEM

SEM images were recorded using a Zeiss Ultra *plus* field emission scanning electron microscope equipped with GEMINI e-Beam column operated at 10 kV.

Crystal Structure Determination

The crystal data of **SQc** were collected at a Bruker Kappa Apex II diffractometer with an Apex II CCD area detector and by Montel multilayer optics monochromated $\text{Mo}_{K\alpha}$ radiation. The structure was solved using direct methods, refined with SHELX software package^[117] and expanded using Fourier techniques. All non-hydrogen atoms were refined anisotropically. Hydrogen atoms were assigned idealized positions and were included in structure factor calculations.

X-Ray Diffractometry of Thin-Films

The measurements were performed with a GE Inspection Technologies X-ray diffractometer (model XRD 3003 T/T) applying Bragg-Brentano geometry. This arrangement means that the X-ray tube and the detector can rotate on the Rowland circle around the fixed sample. The X-ray is based on the copper K_{α} line with a wavelength λ of 1.5418 Å and may be focused by apertures and slits. ω - 2θ -scans were performed during the intensity measurement of the diffracted radiation, while the source is rotated through an angle ω with respect to the spatially fixed sample and the detector is rotated simultaneously through 2θ . The orientation of the source and the detector with respect to each other, the position of the sample in the beam path as well as the alignment of the beam itself is adjusted prior to each measurement. The angular resolution of this setup is limited to 0.005°. The layer spacing d_{hkl} for thin-films can be calculated with the aid of the Bragg equation from the angular position of the Bragg peaks:

$$2d_{hkl} \cdot \sin \theta = \lambda. \quad (6.1)$$

Rocking curves were recorded by adjusting the angles ω and 2θ to fulfill the Bragg condition for a certain reflection. Then the sample was tilted out of plane stepwise by a small angle α up to a final value of 2.5°, while the exposure to X-rays was continued.

Electro-optical absorption measurements, EOAM

Electro-optical absorption measurements were carried out like described in the following. Dipole moments of the ground state μ_g and the dipole moment differences $\Delta\mu = \mu_e - \mu_g$ (μ_e : excited state dipole moment) of chromophores have been determined by means of EOA spectroscopy by which the difference of absorption of a solution with ($\varepsilon^{\mathbf{E}}(\varphi, \tilde{\nu})$) and without ($\varepsilon(\tilde{\nu})$) an externally applied electric field \mathbf{E} is measured with light parallel ($\varphi = 0^\circ$) and perpendicularly ($\varphi = 90^\circ$) polarized to the direction of \mathbf{E} .^[105,118] For uniaxial phases, induced

in a solution by both an alternating and a constant electric field of about $3 \times 10^6 \text{ V m}^{-1}$, the dichroism $\varepsilon^{\mathbf{E}}(\varphi, \tilde{\nu}) - \varepsilon(\tilde{\nu})$ depends on the orientational order of the molecules due to their ground state dipole moment μ_{g} , the shift of the absorption band proportional to the dipole moments difference $\Delta\mu$, and on the electric field dependence of the electric transition dipole moment $\mu_{\text{eg}}(\mathbf{E})$. The transition dipole moment μ_{eg} was determined from UV/Vis/NIR spectra recorded at 298 K.^[118] All measurements were carried out in dry dioxane.

Spin Coater Spin 150

Cleaning of silicon wafers and substrates as well as deposition of thin-films from squaraine solutions were performed using an APT Spin 150 Spin Coater at rotation speeds between 2000 and 3000 rpm. Wafers and substrates were fixed on the turntable by vacuum.

UVO-Cleaner[®]-Ozone Cleaning Device 42A-220 Jelight

A UVO-Cleaner[®]-Ozone Cleaning Device 42A-220 (Jelight Company) was used to remove residues of organic material from the surface of the silicon wafers. The working principle is based on excitation and/or dissociation of impurities by short-wavelength UV radiation and the simultaneous generation of atomic oxygen, which then can react with the excited contaminant molecules.

BOC Edwards Auto 306 Evaporator

Deposition of gold source and drain contacts on top of semiconductor films and of **SQb** semiconductor thin-films on various substrates was performed with a BOC Edwards Auto 306 Evaporator. The deposition rate as well as the thickness of the deposited layer was monitored by a crystal oscillator. The deposition rate for gold was varied by manual control of the voltage applied to the tungsten boat, while the one for organic materials in quartz crucibles was determined by the temperature of the source, which was adjusted by an Edwards Oven Source Controller. The substrates attached to the substrate holder were heated from the backside with a heating lamp. The chamber was pumped down to a pressure of around 10^{-6} mbar prior to deposition of gold and the organic material, respectively.

Micromanipulator 4060 & Semiconductor Parameter Analyzer 4155C

Source, drain and gate electrodes of the OTFTs were contacted with a Micromanipulator 4060 for characterization of the transistor devices. For contacting, the sample was viewed through a reflection polarizing microscope with a camera attached. The output and transfer

characteristics were recorded in air by means of an Agilent Semiconductor Parameter Analyzer 4155C. The sample was fixed to the probe station by a vacuum chuck, which was kept at a temperature of 25 °C.

Drop Shape Analysis System DSA25

The contact angle θ for water on the substrates was determined with a Krüss Drop Shape Analysis System DSA25.

Solvents for the Preparation of Substrates and Transistors

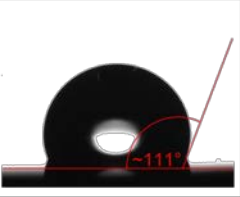
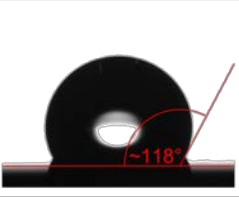
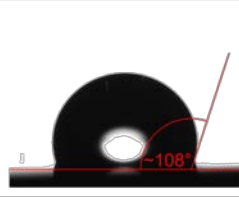
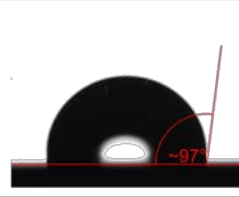
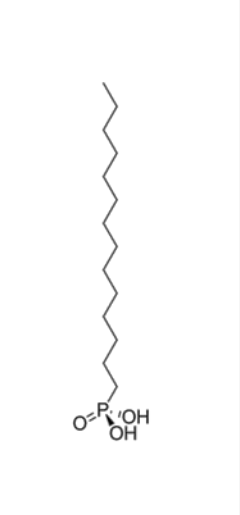
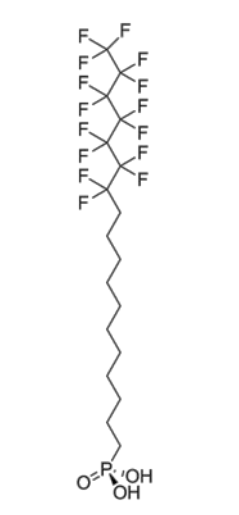
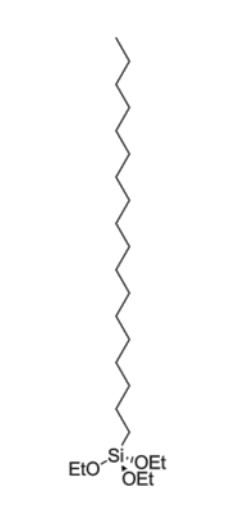
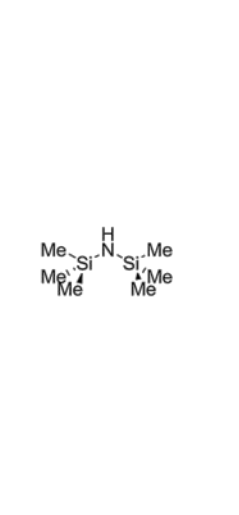
Chloroform (CHCl ₃), water-free ($\geq 99\%$)	(Sigma Aldrich)
<i>o</i> -Dichlorobenzene (<i>o</i> -DCB), water-free ($\geq 99\%$)	(Sigma Aldrich)
Acetone, semiconductor grade	(Sigma Aldrich)
Isopropanol, semiconductor grade	(Sigma Aldrich)
Toluene, AnalaR NORMAPUR	(VWR)
Hydrogen peroxide, 30 % (pa)	(Merck)
Trichloroethylene (TCE), anhydrous ($\geq 99\%$)	(Sigma Aldrich)
Sulfuric acid, $> 95\%$	(Fischer Scientific)

SAM reagents

Hexamethyldisilazane (HMDS), electronic grade, 99 %	(ABCR)
<i>n</i> -Octadecyltriethoxysilane (OTES), 94 % with 5 – 10 % branched C18-isomers	(ABCR)

6.2 Substrates

Table 10. Composition of SAM-modified substrates, the contact angles θ for water on these substrates and the molecular structures of the SAMs.

SAM	TPA (1.7 nm)	FOPA (1.7 nm)	OTES (2.1 nm)	HMDS (2.1 nm)
dielectric	AlO _x (3.6 nm ALD) SiO ₂ (100 nm thermal)	AlO _x (3.6 nm ALD) SiO ₂ (100 nm thermal)	SiO ₂ (300 nm thermal)	SiO ₂ (300 nm thermal)
gate	Si (heavily doped)	Si (heavily doped)	Si (heavily doped)	Si (heavily doped)
contact angle θ for H ₂ O				
molecular structure of the SAM				

Silicon substrates

P/Bor doped n-type Si (100) wafers ($<0.02 \Omega \text{ cm}$) were used as substrates, which also served as a common gate electrode of the transistors. In the case of bare substrates the gate dielectric consisted only of a 100 nm SiO₂ layer (capacitance per unit area $C_i = 34.0 \text{ nF cm}^{-2}$). The surface of the SiO₂ layer was also treated with HMDS and OTES to obtain SAM-modified Si/SiO₂ substrates (see below).

Additionally, Si/SiO₂/AlO_x substrates were prepared from such Si/SiO₂ wafers by atomic layer deposition of an 8 nm thick layer of AlO_x, which was done by Dr. Hagen Klauk from the Max Planck Institut in Stuttgart. This group prepared also highly reflecting Si/Al/AlO_x substrates, which were used for spectroscopy in reflection mode. First, a 20 nm thick aluminum layer was deposited onto silicon wafers by thermal evaporation and subsequently a 3.6 nm thick AlO_x layer was obtained by brief exposure of the aluminum to oxygen plasma.

Preparation of HMDS-modified wafers

Si/SiO₂ wafers were rinsed with toluene, acetone and finally isopropanol in the spin coater at 3.000 rpm for about 60 seconds and subsequently treated in the UVO-Cleaner for five minutes. These purified wafers were coated with a SAM of HMDS according to the following procedure: HMDS was filtered through a syringe filter (WICOM PERFECT-FLOW[®] PTFE, 13 mm, 0.2 μm). The surface of the wafers was covered with the filtered liquid and the residual was after an application time of 10 seconds removed in the spin coater at 3000 rpm for 30 seconds. A capacitance per unit area $C_i = 34.0 \text{ nF cm}^{-2}$ was determined for these substrates.

Preparation of OTES-modified wafers

Si/SiO₂ wafers were treated for 30 minutes in a bath of freshly prepared piranha solution, which is a mixture of concentrated sulfuric acid and hydrogen peroxide in a ratio of 7:3. To remove the residues of the etching process, the wafer was first sonicated for five minutes in demineralized water and subsequently rinsed with demineralized water at 5000 rpm in the spin coater. Coating with the OTES SAM succeeds this purification procedure. For this purpose a 3 mM solution of OTES (filtrated through a syringe filter, WICOM PERFECT-FLOW[®] PTFE, 13 mm, 0.2 μm) in TCE was prepared and filtrated at least two times through a syringe filter. The wafer is then covered completely with the solution, which is after an application time of 10 seconds removed in the spin coater at 3000 rpm for 30 seconds. The wafers were stored overnight in a desiccator over ammonia solution to interlink the SAM molecules. Afterwards they were sonicated for six minutes in toluene to remove possibly formed multilayers. Subsequent purification is done in the spin coater by rinsing with toluene, acetone and subsequently isopropanol at 3000 rpm for about 60 seconds. A capacitance per unit area $C_i = 34.0 \text{ nF cm}^{-2}$ was determined for these substrates.

Tetradecylphosphonic acid (TPA) and 12,12,13,13,14,14,15,15,16,16,17,17,18,18,18H-pentadecafluorooctadecyl phosphonic acid (FOPA) modified substrates

These substrates were kindly provided by Dr. Hagen Klauk from the Max Planck Institut in Stuttgart.

The Si/SiO₂/AlO_x substrates were coated by isopropanol solutions of TPA and FOPA to obtain densely packed monolayers with a thickness of 1.7 nm and 2.1 nm, respectively. A capacitance per unit area of $C_i = 32.4 \text{ nF cm}^{-2}$ was determined for these modified substrates.

The same procedure was applied to Si/Al/AlO_x substrates for formation of a self-assembled TPA monolayer with a thickness of 1.7 nm.

6.3 Thin-Film Deposition

6.3.1 Spin Coating

The substrates were cleaned in the spin coater by rinsing with toluene, acetone and subsequently isopropanol at 3000 rpm for about 60 seconds. Bare Si/SiO₂ substrates were additionally treated in the UVO-Cleaner for five minutes. A solution of the semiconductor material in chloroform with a concentration of 2.0 mg mL⁻¹ was prepared and filtrated through a syringe filter (WICOM PERFECT-FLOW[®] PTFE, 13 mm, 0.2 μm). The substrate was covered by this solution and the residual was after an application time of 10 seconds removed in the spin coater at 3000 rpm for 30 seconds. The substrates were split into two parts, where one was used for preparation of as cast devices and the other for preparation of annealed devices. Thermal treatment of the film was carried out under argon atmosphere at 130 °C for 10 minutes.

6.3.2 Solution Shearing

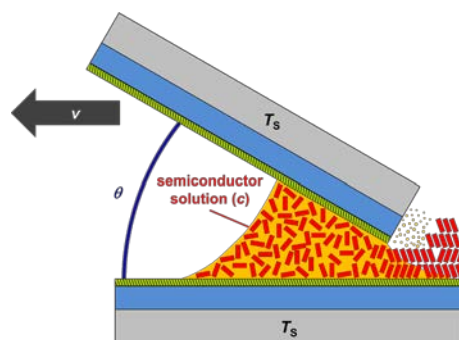


Figure 42. Schematic depiction of the shearing process illustrating the various shearing parameters.

Substrates were cut to the size of approximately 1.5 x 2.5 cm² to fit to the recess of the copper substrate holder. The substrates were cleaned in the spin coater by rinsing with toluene, acetone and subsequently isopropanol at 3000 rpm for about 60 seconds. Bare Si/SiO₂ substrates were additionally treated in the UVO-Cleaner for five minutes. The shearing tool, a piece of an OTES-modified Si/SiO₂ wafer, was cleaned by rinsing with chloroform, toluene, acetone and subsequently isopropanol. The substrates were placed in the recess of the substrate holder and heated to the substrate temperature T_S ($T_S = 100$ °C or 130 °C for **SQd**; $T_S = 130$ °C for **SQe** and **SQf**) by a precision hot plate (model PZ 28-2, Harry Gestigkeit GmbH). Semiconductor solutions were prepared with *o*-DCB at various concentrations

($c = 0.33 \text{ mg mL}^{-1}$, 0.65 mg mL^{-1} , 1.3 mg mL^{-1} , 2.0 mg mL^{-1} , 2.5 mg mL^{-1} , 5.0 mg mL^{-1} , 10 mg mL^{-1} , 20 mg mL^{-1} for **SQd**; $c = 2.0 \text{ mg mL}^{-1}$ for **SQe** and **SQf**). The solutions were stirred and heated at $100 \text{ }^\circ\text{C}$ for at least half an hour before filtration through a syringe filter (WICOM PERFECT-FLOW[®] PTFE, 13 mm, $0.2 \text{ }\mu\text{m}$). $40 \text{ }\mu\text{L}$ of the 100°C hot solution were dispensed by a $100 \text{ }\mu\text{L}$ EPPENDORF pipette between the shearing tool and the substrate. The shearing tool was bolted on copper holders, which were shaped in such a way that the shearing tool adopts an angle θ with respect to the substrate ($\theta = 0^\circ, 15^\circ, 30^\circ, 45^\circ, 60^\circ, 90^\circ$ for **SQd**, $\theta = 15^\circ$ for **SQe** and **SQf**). The shearing tool together with the shearing tool holder was heated to the respective substrate temperature for at least 5 minutes prior to the shearing process. After positioning of the shearing tool holder the distance between the edge of the shearing tool and the substrate was adjusted for $\theta > 0^\circ$ by a micrometer screw with the help of a laser pointer. Its laser beam was reflected by a piece of Si/SiO₂ wafer mounted upside down on the back of the shearing tool. On approaching the shearing tool to the substrate surface the reflected laser beam was projected onto a board with a grid. It was observed that the shearing tool is rebound after contact with the substrate, which means the laser beam moving from this point on to the opposite direction. This fact was used to assure that the shearing tool is in contact with the surface of the substrate. Because this method doesn't work for a shearing angle $\theta = 0^\circ$, the procedure was as follows: Prior to the deposition of the solution the shearing tool was brought into direct contact by adjusting the micrometer screw. The value for this position was read from the screw and noted down. After deposition of the solution the shearing tool was then approached to the substrate with the help of the micrometer screw, which was tuned to a value close to that noted down before to ensure a small gap between the shearing tool and the substrate. The proper adjustment of the distance between shearing tool and substrate was followed by the shearing process, where the shearing tool was moved over the substrate by a motor with the variable speed set to $v = 0.086 \text{ mm s}^{-1}$.

6.3.3 Vapor Deposition

A 30 nm thick layer of the squaraine dye **SQb** was deposited on bare Si/SiO₂, SAM-modified Si/SiO₂ and quartz substrates ($T_S = 180 \text{ }^\circ\text{C}$) in a BOC Edwards Auto 306 Evaporator by thermal sublimation ($T_{\text{sub}} = 212 \text{ }^\circ\text{C}$) at high vacuum ($p = 1.35 \times 10^{-6} \text{ mbar}$). The deposition rate was adjusted to a value of approximately 1.0 nm min^{-1} prior to opening of the shutter. The substrates were allowed to cool to room temperature before venting the evaporation chamber with nitrogen 5.0 and further processing of the substrates.

6.4 Device Fabrication and Characterization

The transistor devices of thin-films prepared by spin coating, solution shearing or vacuum deposition were finally completed by deposition of 30 nm thick source and drain electrodes. This was done in a BOC Edwards Auto 306 Evaporator by thermal sublimation of gold through steel shadow masks at high vacuum ($p \sim 1 \times 10^{-6}$ mbar). The deposition rate was adjusted to a value of about 2.0 nm min^{-1} . The pads had a size of $200 \times 200 \mu\text{m}^2$ and were separated from each other by a distance of $100 \mu\text{m}$ (see Figure 43). This means, that all devices had a channel width W of $200 \mu\text{m}$ and a channel length L of $100 \mu\text{m}$. All OTFTs were electrically isolated prior to the characterization by scratching the semiconductor film around the device with a needle of the micromanipulator. All devices were then characterized by first recording the transfer curve ($V_{\text{DS}} = -50 \text{ V}$; $V_{\text{GS}} = 10$ to -40 V) followed by the measurement of the output characteristics ($V_{\text{GS}} = 0 \text{ V}$, -10 V , -20 V , -30 V , -40 V , -50 V ; $V_{\text{DS}} = 0$ to -50 V) at ambient conditions.

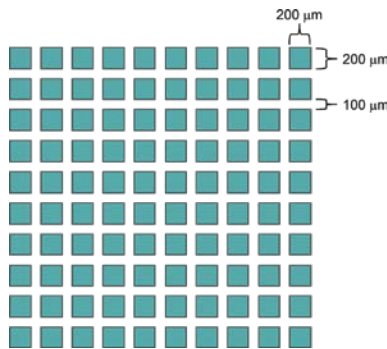


Figure 43. Mask design applied for deposition of the gold contacts.

6.5 Crystal Structure Data of SQc

Table 11. Overview for the crystal structure and refinement data for squaraine SQc.

Squaraine	SQc
Chemical formula	C ₃₉ H ₄₄ N ₄ OSe ₂
Molecular weight (g mol ⁻¹)	742.70
Temperature (K)	109(2)
Radiation, λ (Å)	MoK α , 0.71073
<i>Description of the crystal</i>	
Dimension of the crystal (mm × mm × mm)	0.045 × 0.22 × 0.42
Color	purple
Description	plate
Crystal system	monoclinic
Space group	C2/c
<i>Dimensions of the unit cell</i>	
<i>a</i> (Å)	27.572(3)
<i>b</i> (Å)	9.4876(9)
<i>c</i> (Å)	13.5972(13)
α (°)	90
β (°)	101.349(5)
γ (°)	90
Volume (Å ³)	3487.3(6)
<i>Z</i>	4
ρ_{calc} (g cm ⁻³)	1.415
μ (mm ⁻¹)	2.157
<i>F</i> (000)	1 528
Range of θ (°)	2.289 to 27.32
Number of recorded reflections	52 182
Number of independent reflections	4 321
Minimum / maximum of transmission	0.6037 / 0.7457
Method of refinement	full-matrix least-squares on F^2
Parameters / restraints	249 / 0
Goodness-of-fit for F^2	1.070
Final <i>R</i> indices [$I > 2\sigma(I)$]	$R_1 = 0.0306$; $wR_2 = 0.0681$
<i>R</i> indices (all data points)	$R_1 = 0.0438$; $wR_2 = 0.0726$
Maximum / minimum of residual electron density (e Å ⁻³)	0.68 / -0.59

Table 12. Atomic coordinates (x , y and z) and equivalent isotropic displacement parameter $U(\text{eq})$ [\AA^2] for the squaraine **SQc**. $U(\text{eq})$ is defined as one third of the trace of the orthogonalized U_{ij} tensors.

	x	y	z	$U(\text{eq})$
C1	0.58928(8)	1.1466(2)	-0.00984(15)	0.0209(4)
C2	0.60300(8)	1.2775(2)	-0.04105(16)	0.0244(5)
C3	0.62438(9)	1.2843(2)	-0.12474(17)	0.0262(5)
C4	0.63163(8)	1.1621(2)	-0.17666(16)	0.0250(5)
C5	0.61766(8)	1.0315(2)	-0.14612(15)	0.0222(4)
C6	0.59596(8)	1.0242(2)	-0.06242(16)	0.0213(4)
C7	0.55871(8)	0.9161(2)	0.05885(16)	0.0202(4)
C8	0.54113(8)	0.8035(2)	0.10848(15)	0.0219(4)
C9	0.51794(8)	0.8136(2)	0.18972(15)	0.0201(4)
C10	0.5000	0.9243(3)	0.2500	0.0195(6)
C11	0.5000	0.7086(3)	0.2500	0.0210(6)
C12	0.5000	0.5613(3)	0.2500	0.0230(6)
C13	0.52616(9)	0.4838(2)	0.18812(17)	0.0288(5)
C14	0.57923(8)	0.7669(2)	-0.07896(16)	0.0239(5)
C15	0.62979(9)	0.6952(2)	-0.05566(17)	0.0287(5)
C16	0.64637(9)	0.6525(2)	0.05400(18)	0.0319(5)
C17	0.69733(11)	0.5911(3)	0.0797(2)	0.0505(8)
C18	0.71196(15)	0.5707(4)	0.1966(3)	0.0314(10)
C19	0.76596(15)	0.5298(4)	0.2304(3)	0.0421(11)
C20	0.7815(2)	0.5006(6)	0.3421(4)	0.0457(12)
C21	0.7780(5)	0.6271(11)	0.4117(10)	0.055(3)
C17B	0.69733(11)	0.5911(3)	0.0797(2)	0.0505(8)
C18B	0.7221(4)	0.4924(12)	0.1557(9)	0.041(3)
C19B	0.7404(5)	0.5915(13)	0.2380(9)	0.035(3)
C20B	0.7595(7)	0.516(2)	0.3412(14)	0.053(5)
C21B	0.7737(14)	0.618(4)	0.413(3)	0.060(11)
N1	0.54836(10)	0.4225(2)	0.13900(19)	0.0439(6)
N2	0.57837(7)	0.90135(17)	-0.02452(13)	0.0207(4)
O1	0.5000	1.0540(2)	0.2500	0.0235(5)
Se1	0.559055(8)	1.10671(2)	0.099608(15)	0.02053(7)

Table 13. Anisotropic displacement parameters U_{ij} [\AA^2] for the squaraine **SQc**.

	U_{11}	U_{22}	U_{33}	U_{23}	U_{13}	U_{12}
C1	0.0291(11)	0.0163(9)	0.0190(10)	-0.0001(7)	0.0089(8)	-0.0011(8)
C2	0.0353(12)	0.0149(10)	0.0251(11)	-0.0010(8)	0.0111(9)	-0.0014(9)
C3	0.0360(13)	0.0174(10)	0.0276(12)	0.0022(8)	0.0119(10)	-0.0035(9)
C4	0.0345(12)	0.0228(11)	0.0202(11)	0.0017(8)	0.0110(9)	-0.0028(9)
C5	0.0315(12)	0.0182(10)	0.0183(10)	-0.0010(8)	0.0083(8)	-0.0005(9)
C6	0.0304(12)	0.0148(9)	0.0193(10)	-0.0002(8)	0.0066(8)	-0.0014(8)
C7	0.0292(11)	0.0128(9)	0.0199(10)	-0.0013(7)	0.0081(8)	0.0014(8)
C8	0.0341(12)	0.0128(9)	0.0207(10)	-0.0008(8)	0.0103(9)	-0.0006(8)
C9	0.0298(11)	0.0123(9)	0.0188(10)	-0.0005(7)	0.0062(8)	0.0002(8)
C10	0.0266(15)	0.0154(13)	0.0172(14)	0.000	0.0065(11)	0.000
C11	0.0288(16)	0.0169(14)	0.0185(14)	0.000	0.0077(12)	0.000
C12	0.0353(18)	0.0140(13)	0.0224(15)	0.000	0.0124(13)	0.000
C13	0.0478(15)	0.0117(9)	0.0311(12)	0.0011(8)	0.0184(11)	-0.0029(9)
C14	0.0393(13)	0.0157(10)	0.0187(10)	-0.0037(8)	0.0108(9)	-0.0004(9)
C15	0.0422(14)	0.0183(10)	0.0281(12)	-0.0013(9)	0.0130(10)	0.0036(10)
C16	0.0427(14)	0.0230(11)	0.0298(12)	0.0026(9)	0.0063(10)	-0.0013(10)
C17	0.0431(16)	0.0464(17)	0.0592(19)	0.0204(14)	0.0031(14)	-0.0040(13)
C18	0.033(2)	0.0283(19)	0.036(2)	0.0027(15)	0.0119(16)	0.0091(15)
C19	0.040(2)	0.044(2)	0.042(2)	-0.0050(16)	0.0084(16)	0.0188(19)
C20	0.046(3)	0.047(2)	0.042(2)	-0.0067(18)	0.004(3)	0.018(3)
C21	0.043(6)	0.052(4)	0.068(7)	-0.019(4)	0.006(4)	0.014(4)
C17B	0.0431(16)	0.0464(17)	0.0592(19)	0.0204(14)	0.0031(14)	-0.0040(13)
C18B	0.039(7)	0.031(6)	0.056(8)	0.000(5)	0.015(6)	0.009(5)
C19B	0.024(6)	0.037(6)	0.043(7)	0.007(5)	0.003(5)	0.008(5)
C20B	0.050(11)	0.073(11)	0.042(8)	0.004(7)	0.020(9)	0.029(10)
C21B	0.025(11)	0.12(3)	0.031(14)	-0.007(13)	-0.007(9)	-0.022(12)
N1	0.0727(17)	0.0149(9)	0.0571(15)	-0.0025(9)	0.0444(13)	-0.0031(10)
N2	0.0334(10)	0.0117(8)	0.0186(8)	-0.0007(7)	0.0093(7)	-0.0005(7)
O1	0.0372(13)	0.0115(9)	0.0245(11)	0.000	0.0126(9)	0.000
Se1	0.03393(13)	0.01177(10)	0.01838(11)	-0.00073(8)	0.01121(8)	-0.00071(9)

REFERENCES

- [1] P. Horowitz, W. Hill in *The Art of Electronics*, 2nd ed., Cambridge University Press, Cambridge, **1990**.
- [2] a) P. E. Burrows, S. R. Forrest, M. E. Thompson, *Curr. Opin. Solid State Mater. Sci.* **1997**, *2*, 236–243; b) W. A. MacDonald, *J. Mater. Chem.* **2004**, *14*, 4–10; c) G. H. Gelinck, H. E. A. Huitema, E. van Veenendaal, E. Cantatore, L. Schrijnemakers, J. B. P. H. van der Putten, T. C. T. Geuns, M. Beenhakkers, J. B. Giesbers, B.-H. Huisman, E. J. Meijer, E. M. Benito, F. J. Touwslager, A. W. Marsman, B. J. E. van Rens, D. M. de Leeuw, *Nat. Mater.* **2004**, *3*, 106–110; d) B. Geffroy, P. le Roy, C. Prat, *Polym. Int.* **2006**, *55*, 572–582; e) S. Ju, J. Li, J. Liu, P.-C. Chen, Y.-g. Ha, F. Ishikawa, H. Chang, C. Zhou, A. Facchetti, D. B. Janes, and T. J. Marks, *Nano Lett.* **2008**, *8*, 997–1004.
- [3] a) V. Subramanian, J. M. J. Frechet, P. C. Chang, D. C. Huang, J. B. Lee, S. E. Molesa, A. R. Murphy, D. R. Redinger, S. K. Volkman, *Proc. IEEE* **2005**, *93*, 1330–1338; b) M. Berggren, D. Nilsson, N. D. Robinson, *Nat. Mater.* **2006**, *6*, 3–5; c) H. Usta, A. Facchetti, T. J. Marks, *Acc. Chem. Res.* **2011**, *44*, 501–510.
- [4] a) *Organic Field-Effect Transistors* (Eds.: Z. Bao, J. Locklin), Taylor and Francis, Boca Raton, USA, **2007**; b) *Organic Electronics* (Ed.: H. Klauk), Wiley-VCH, Weinheim, Germany, **2006**; c) *Organic Electronics II* (Ed.: H. Klauk), Wiley-VCH, Weinheim, Germany, **2012**; d) H. Klauk, *Chem. Soc. Rev.* **2010**, *39*, 2643–2666.
- [5] C. Wang, H. Dong, W. Hu, Y. Liu, D. Zhu, *Chem. Rev.* **2012**, *112*, 2208–2267.
- [6] M. Noda, N. Kobayashi, M. Katsuhara, A. Yumoto, S. Ushikura, R. Yasuda, N. Hirai, G. Yukawa, I. Yagi, K. Nomoto, T. Urabe, *J. Soc. Inf. Disp.* **2011**, *19*, 316–322.
- [7] U. Mayerhöffer, K. Deing, K. Größ, H. Braunschweig, K. Meerholz, F. Würthner, *Angew. Chem.* **2009**, *121*, 8934–8937; *Angew. Chem. Int. Ed.* **2009**, *48*, 8776–8779.
- [8] a) R. A. Street, *Adv. Mater.* **2009**, *21*, 2007–2022; b) J. Zaumseil, H. Sirringhaus, *Chem. Rev.* **2007**, *107*, 1296–1323; c) G. Horowitz in *Organic Electronics, Materials, Manufacturing and Applications* (Ed.: H. Klauk), Wiley-VCH, Weinheim, **2006**, pp. 3–32; d) D. I. James, J. Smith, M. Heeney, T. D. Anthopoulos, A. Salleo, I. McCulloch in *Organic Electronics II: More Materials and Applications, 1st ed.* (Ed.: H. Klauk), Wiley-VCH, Weinheim, **2012**, pp. 3–26; e) D. Braga, G. Horowitz, *Adv. Mater.* **2009**, *21*, 1473–1486.
- [9] P. K. Weimer, *Proc. IRE* **1962**, *50*, 1462–1469.

-
- [10] P. G. LeComber, W. E. Spear, A. Ghaith, *Electron. Lett.* **1979**, *15*, 179–181.
- [11] a) A. Tsumura, K. Koezuka, T. Ando, *Appl. Phys. Lett.* **1986**, *49*, 1210–1212; b) A. Tsumura, H. Koezuka, Y. Ando, *Synth. Metal* **1988**, *25*, 11–23; c) G. Horowitz, D. Fichou, X. Z. Peng, Z. G. Xu, F. Garnier, *Solid State Commun.* **1989**, *72*, 381–384; d) G. Horowitz, X. Z. Peng, D. Fichou, F. Garnier, *J. Appl. Phys.* **1990**, *67*, 528–532.
- [12] a) F. C. Grozema, L. D. A. Siebbeles, *Int. Rev. Phys. Chem.* **2008**, *27*, 87–138; b) V. Coropceanu, J. Cornil, D. A. da Silva Filho, Y. Oliver, R. Silbey, J.-L. Bredas, *Chem. Rev.* **2007**, *107*, 926–952; c) H. Bässler, A. Köhler, *Top. Curr. Chem.* **2012**, *312*, 1–66; d) D. Hertel, H. Bässler, *ChemPhysChem* **2008**, *9*, 666–688.
- [13] a) H. Scher, M. Lax, *Phys. Rev. B* **1973**, *7*, 4491–4502; b) H. Scher, E. W. Montroll, *Phys. Rev. B* **1975**, *12*, 2455–2477.
- [14] H. Bässler, *Phys. Stat. Sol. B* **1993**, *175*, 15–56.
- [15] D. A. Neamen in *Semiconductor Physics and Devices: Basic Principles*, Richard D. Irwin Inc., Burr Ridge, **1992**.
- [16] A. Dieckmann, H. Bässler, P. M. Borsenberger, *J. Chem. Phys.* **1993**, *99*, 8136–8141.
- [17] A. Miller, E. Abrahams, *Phys. Rev.* **1960**, *120*, 745–755.
- [18] a) M. Vissenberg, M. Matters, *Phys. Rev. B* **1998**, *57*, 12964–12967; b) R. A. Street, J. E. Northrup, A. Salleo, *Phys. Rev. B* **2005**, *71*, 165202-1–13; c) C. Tanase, E. J. Meijer, P. W. M. Blom, D. M. de Leeuw, *Org. Electron.* **2003**, *4*, 33–37; d) C. Tanase, E. J. Meijer, P. W. M. Blom, D. M. de Leeuw, *Phys. Rev. Lett.* **2003**, *91*, 216601-1–4; e) D. H. Dunlap, P. E. Parris, V. M. Kenkre, *Phys. Rev. Lett.* **1996**, *77*, 542–545; f) I. I. Fishchuk, A. Kadashchuk, V. I. Arkhipov, H. Bässler in *Photophysics of Molecular Materials* (Ed.: G. Ganzani), Wiley-VCH, Weinheim, **2006**; g) V. I. Arkhipov, P. Heremans, E. V. Emelianova, G. J. Adriaenssens, H. Bässler, *J. Phys.: Condens. Matter* **2002**, *14*, 9899–9911.
- [19] a) B. Lucas, T. Trigaud, C. Videlot-Ackermann, *Polym. Int.* **2012**, *61*, 374–389; b) Y. Wen, Y. Liu, Y. Guo, G. Yu, W. Hu, *Chem. Rev.* **2011**, *111*, 3358–3406.
- [20] A. C. Mayer, J. M. Blakely, G. G. Malliaras in *Organic Field-Effect Transistors* (Eds.: Z. Bao, J. Locklin), CRC Press, Boca Raton, **2007**, 341–369.
- [21] X. Gao, C. Di, Y. Hu, X. Yang, H. Fan, F. Zhang, Y. Liu, H. Li, D. Zhu, *J. Am. Chem. Soc.* **2010**, *132*, 3697–3699.
- [22] H. Dong, H. Li, E. Wang, Z. Wie, W. Xu, W. Hu, S. Yan, *Langmuir* **2008**, *24*, 13241–13244.

- [23] C. Piliego, D. Jarzab, G. Gigli, Z. Chen, A. Facchetti, M. A. Loi, *Adv. Mater.* **2009**, *21*, 1573–1576.
- [24] E. J. W. Crossland, K. Tremel, F. Fischer, K. Rahimi, G. Reiter, U. Steiner, S. Ludwigs, *Adv. Mater.* **2012**, *24*, 839–844.
- [25] a) W. Pisula, A. Menon, M. Stepputat, I. Lieberwirth, U. Kolb, A. Tracz, H. Siringhaus, T. Pakula, K. Müllen, *Adv. Mater.* **2005**, *17*, 684–689; b) M. Mas-Torrent, S. Masirek, P. Hadley, N. Crivillers, N. S. Oxtoby, P. Reuter, J. Veciana, C. Rovira, A. Tracz, *Org. Electronics* **2008**, *9*, 143–148.
- [26] J. Jang, S. Nam, K. Im, J. Hur, S. N. Cha, J. Kim, H. B. Son, H. Suh, M. A. Loth, J. E. Anthony, J.-J. Park, C. E. Park, J. M. Kim, K. Kim, *Adv. Funct. Mater.* **2012**, *22*, 1005–1014.
- [27] a) Z. Liu, H. A. Becerril, M. E. Roberts, Y. Nishi, Z. Bao, *IEEE Transactions on Electron Devices* **2009**, *56*, 176–185; b) G. Giri, E. Verploegen, S. C. B. Mannsfeld, S. Atahan-Evrenk, D. H. Kim, Sang Yoon Lee, H. A. Becerril, A. Aspuru-Guzik, M. F. Toney, Z. Bao, *Nature* **2011**, *480*, 504–508; c) W.-Y. Lee, J. H. Oh, S.-L. Suraru, W.-C. Chen, F. Würthner, Z. Bao, *Adv. Funct. Mater.* **2011**, *21*, 4173–4181, d) J. H. Oh, S.-L. Suraru, W.-Y. Lee, M. Könnemann, H. W. Höffken, C. Röger, R. Schmidt, Y. Chung, W.-C. Chen, F. Würthner, Z. Bao, *Adv. Funct. Mater.* **2010**, *20*, 2148–2156; e) H. A. Becerril, M. E. Roberts, Z. Liu, J. Locklin, Z. Bao, *Adv. Mater.* **2008**, *20*, 2588–2594.
- [28] a) T. Minari, M. Kano, T. Miyadera, S. D. Wang, Y. Aoyagi, K. Tsukagoshi, *Appl. Phys. Lett.* **2009**, *94*, 093307; b) T. Minari, C. Liu, M. Kano, K. Tsukagoshi, *Adv. Mater.* **2012**, *24*, 299–306.
- [29] J. Soeda, T. Uemura, Y. Mizuno, A. Nakao, Y. Nakazawa, A. Facchetti, J. Takeya, *Adv. Mater.* **2011**, *23*, 3681–3685.
- [30] a) D. Shukla, S. F. Nelson, D. C. Freeman, M. Rajeswaran, W. G. Ahearn, D. M. Meyer, J. T. Carey, *Chem. Mater.* **2008**, *20*, 7486–7491; b) A. P. Adiga, D. Shukla, *J. Phys. Chem. C* **2010**, *114*, 2751–2755.
- [31] M. J. Kang, L. Doi, H. Mori, E. Miyazaki, K. Takimiya, M. Ikeda, H. Kuwabara, *Adv. Mater.* **2011**, *23*, 1222–1225.
- [32] M. Zhang, H. N. Tsao, W. Pisula, C. Yang, A. K. Mishra, K. Müllen, *J. Am. Chem. Soc.* **2007**, *129*, 3472–3473.
- [33] H. Yan, Z. H. Chen, Y. Zheng, C. Newman, J. R. Quinn, F. Dotz, M. Kastler, A. Facchetti, *Nature* **2009**, *457*, 679–687.

- [34] a) *Industrial Dyes* (Ed.: K. Hunger), Wiley-VCH, Weinheim, **2003**; b) H. Zollinger, *Color Chemistry*, 3rd ed., Wiley-VCH, Weinheim, **2003**.
- [35] A. Braun, J. Tcherniac, *Ber. Dtsch. Chem. Ges.* **1907**, *40*, 2709–2714.
- [36] a) R. P. Linstead, *J. Chem. Soc.* **1934**, 1016–1017; b) G. T. Byrne, R. P. Linstead, A. R. Lowe, *J. Chem. Soc.* **1934**, 1017–1022; c) R. P. Linstead, A. R. Lowe, *J. Chem. Soc.* **1934**, 1022–1027; d) C. E. Dent, R. P. Linstead, *J. Chem. Soc.* **1934**, 1027–1031; e) R. P. Linstead, A. R. Lowe, *J. Chem. Soc.* **1934**, 1031–1033; f) T. M. Reynolds, R. Robinson, *J. Chem. Soc.* **1934**, 1033–1039.
- [37] a) J. M. Robertson, I. Woodward, *J. Chem. Soc.* **1937**, 219–230; b) J. M. Robertson, *J. Chem. Soc.* **1935**, 615–621; c) J. M. Robertson, I. Woodward, *J. Chem. Soc.* **1940**, 36–48; d) J. M. Robertson, *J. Chem. Soc.* **1936**, 1195–1209.
- [38] A. T. Vartanyan, *Zh. Fiz. Khim.* **1948**, *22*, 769–782.
- [39] a) F. H. Moser, A. L. Thomas, *The Phthalocyanines*, CRC Press, Boca Raton, **1983**; b) K. Y. Law, *Chem. Rev.* **1993**, *93*, 449–486; c) D. Dini, M. Hanack in *The Porphyrin Handbook, Volume 17 / Phthalocyanines: Properties and Materials* (Eds.: K. M. Kadish, K. M. Smith, R. Guilard), Academic Press, San Diego, **2003**.
- [40] a) M. Madru, G. Guillaud, M. Al Sadoun, M. Maitrot, C. Clarisse, M. Le Contellec, J.-J. Andre, J. Simon, *Chem. Phys. Lett.* **1987**, *142*, 103–105; b) R. Madru, G. Guillaud, M. Al Sadoun, M. Maitrot, J.-J. Andre, J. Simon, R. Even, *Chem. Phys. Lett.* **1988**, *145*, 343–346; c) C. Clarisse, M. T. Riou, M. Gauneau, M. Le Contellec, *Electron. Lett.* **1988**, *24*, 674–675; d) P. Petit, P. Turek, J.-J. Andre, R. Even, J. Simon, R. Madru, M. Al Sadoun, G. Guillaud, M. Maitrot, *Synth. Met.* **1989**, *29*, 59–64; e) G. Guillaud, M. Al Sadoun, M. Maitrot, J. Simon, M. Bouvet, *Chem. Phys. Lett.* **1990**, *167*, 503–506.
- [41] G. Guillaud, R. Madru, M. Al Sadoun, M. Maitrot, *J. Appl. Phys.* **1989**, *66*, 4554–4556.
- [42] a) Z. Bao, A. J. Lovinger, A. Dodabalapur, *Appl. Phys. Lett.* **1996**, *69*, 3066–3068; b) Z. Bao, A. J. Lovinger, A. Dodabalapur, *Adv. Mater.* **1997**, *9*, 42–44.
- [43] H. Wang, F. Zhu, J. Yang, Y. Geng, D. Yan, *Adv. Mater.* **2007**, *19*, 2168–2171.
- [44] a) R. Zeis, T. Siegrist, C. Kloc, *Appl. Phys. Lett.* **2005**, *86*, 022103; b) R. W. I. de Boer, A. F. Stassen, M. F. Craciun, C. L. Mulder, A. Molinari, S. Rogge, A. F. Morpurgo, *Appl. Phys. Lett.* **2005**, *86*, 262109; c) K. Yamada, J. Takeya, K. Shigeto, K. Tsukagoshi, Y. Aoyagi, Y. Iwasa, *Appl. Phys. Lett.* **2006**, *88*, 122110-1–122110-3.
- [45] J. Zhang, J. Wang, H. Wang, D. Yan, *Appl. Phys. Lett.* **2004**, *84*, 142–144.

- [46] a) H. Tada, H. Touda, M. Takada, K. Matsushige, *Appl. Phys. Lett.* **2000**, *76*, 873–875; b) L. Li, Q. Tang, H. Li, X. Yang, W. Hu, Y. Song, Z. Shuai, W. Xu, Y. Liu, D. Zhu, *Adv. Mater.* **2007**, *19*, 2613–2617.
- [47] a) H. Ohta, T. Kambayashi, K. Nomura, M. Hirano, K. Ishikawa, H. Takezoe, H. Hosono, *Adv. Mater.* **2004**, *16*, 312–316; b) H. Wang, D. Song, J. Yang, B. Yu, Y. Geng, D. Yan, *Appl. Phys. Lett.* **2007**, *90*, 253510; c) L. Li, Q. Tang, H. Li, W. Hu, *J. Phys. Chem. B* **2008**, *112*, 10405–10410; d) L. Huang, C. Liu, X. Qiao, H. Tian, Y. Geng, D. Yan, *Adv. Mater.* **2011**, *23*, 3455–3459.
- [48] W. Hiller, J. Strähle, W. Kobel, M. Hanack, *Z. Kristallogr.* **1982**, *159*, 173–183.
- [49] Z. Bao, A. J. Lovinger, J. Brown, *J. Am. Chem. Soc.* **1998**, *120*, 207–208.
- [50] M. L. Tang, J. H. Oh, A. D. Reichardt, Z. Bao, *J. Am. Chem. Soc.* **2009**, *131*, 3733–3740.
- [51] a) D. Song, H. Wang, F. Zhu, J. Yang, H. Tian, Y. Geng, D. Yan, *Adv. Mater.* **2008**, *20*, 2142–2144; b) D. Song, F. Zhu, B. Yu, L. Huang, Y. Geng, D. Yan, *Appl. Phys. Lett.* **2008**, *92*, 143303.
- [52] a) A. Hirao, T. Akiyama, T. Okujima, H. Yamada, H. Uno, Y. Sakai, S. Aramaki, N. Ono, *Chem. Commun.* **2008**, 4714–4716; b) S. Dong, H. Tian, D. Song, Z. Yang, D. Yan, Y. Geng, F. Wang, *Chem. Commun.* **2009**, 3086–3088; c) N. B. Chaure, T. Basova, M. Zahedi, A. K. Ray, A. K. Sharma, M. Durmus, V. Ahsen, *J. Appl. Phys.* **2010**, *107*, 114503; d) E. Miyazaki, A. Kaku, H. Mori, M. Iwatani, K. Takimiya, *J. Mater. Chem.* **2009**, *19*, 5913–5915; e) S. Dong, H. Tian, L. Huang, J. Zhang, D. Yan, Y. Geng, F. Wang, *Adv. Mater.* **2011**, *23*, 2850–2854.
- [53] P. Ma, J. Kan, Y. Zhang, C. Hang, Y. Bian, Y. Chen, N. Kobayshi, J. Jiang, *J. Mater. Chem.* **2011**, *21*, 18552–18559.
- [54] a) A. Dodabalapur, H. E. Katz, L. Torsi, R. C. Haddon, *Science* **1995**, *269*, 1560–1562; b) G. Horowitz, F. Kouki, P. Spearman, D. Fichou, C. Nogue, X. Pan, F. Garnier, *Adv. Mater.* **1996**, *8*, 242–245.
- [55] J. G. Laquindanum, H. E. Katz, A. Dodabalapur, A. J. Lovinger, *J. Am. Chem. Soc.* **1996**, *118*, 11331–11332.
- [56] a) H. E. Katz, J. Johnson, A. J. Lovinger, W. Li, *J. Am. Chem. Soc.* **2000**, *122*, 7787–7792; b) H. E. Katz, T. Siegrist, J. H. Schön, C. Kloc, B. Batlogg, A. J. Lovinger, J. Johnson, *Chem. Phys. Chem.* **2001**, *2*, 167–172; c) H. E. Katz, A. J. Lovinger, J. Johnson, C. Kloc, T. Siegrist, W. Li, Y.-Y. Lin, A. Dobabalapur, *Nature* **2000**, *404*,

- 478–481; d) K. C. See, C. Landis, A. Sarjeant, H. E. Katz, *Chem. Mater.* **2008**, *20*, 3609–3616.
- [57] B. A. Jones, A. Facchetti, M. R. Wasielewski, T. J. Marks, *J. Am. Chem. Soc.* **2007**, *129*, 15259–15278.
- [58] F. Würthner, M. Stolte, *Chem. Commun.* **2011**, *47*, 5109–5115.
- [59] B. A. Jones, A. Facchetti, T. J. Marks, M. R. Wasielewski, *Chem. Mater.* **2007**, *19*, 2703–2705.
- [60] M. Stolte, S.-L. Suraru, F. Würthner, J. H. Oh, Z. Bao, J. Brill, M. Könemann, J. Qu, U. Zschieschang, H. Klauk, *Proc. of SPIE* **2010**, *7778*, 777804-1–777804-8.
- [61] a) P. R. L. Malenfant, C. D. Dimitrakopoulos, J. D. Gelorme, L. L. Kosbar, T. O. Graham, *Appl. Phys. Lett.* **2002**, *80*, 2517–2519; b) R. J. Chesterfield, J. C. McKeen, C. R. Newman, P. C. Ewbank, D. A. da Silva Filho, J.-L. Bredas, L. L. Miller, K. R. Mann, C. D. Frisbie, *J. Phys. Chem. B* **2004**, *108*, 19281–19292; c) S. Tatemichi, M. Ichikawa, T. Koyama, Y. Taniguchi, *Appl. Phys. Lett.* **2006**, *89*, 112108.
- [62] R. Schmidt, J. H. Oh, Y.-S. Sun, M. Deppisch, A.-M. Krause, K. Radacki, H. Braunschweig, M. Könemann, P. Erk, Z. Bao, F. Würthner, *J. Am. Chem. Soc.* **2009**, *131*, 6215–6228.
- [63] a) B. A. Jones, A. Facchetti, M. R. Wasielewski, T. J. Marks, *Adv. Funct. Mater.* **2008**, *18*, 1329–1339; b) B. A. Jones, M. J. Ahrens, M.-H. Yoon, A. Facchetti, T. J. Marks, M. R. Wasielewski, *Angew. Chem.* **2004**, *116*, 6523–6526; *Angew. Chem. Int. Ed.* **2004**, *43*, 6363–6366.
- [64] M. Gsänger, J. H. Oh, M. Könemann, H. W. Höffken, A.-M. Krause, Z. Bao, F. Würthner, *Angew. Chem.* **2010**, *122*, 752–755; *Angew. Chem. Int. Ed.* **2010**, *49*, 740–743.
- [65] A. S. Molinari, H. Alves, Z. Chen, A. Facchetti, A. F. Morpurgo, *J. Am. Chem. Soc.* **2009**, *131*, 2462–2463.
- [66] a) B. Yoo, B. A. Jones, D. Basu, D. Fine, T. Jung, S. Mohapatra, A. Facchetti, K. Dimmler, M. R. Wasielewski, T. J. Marks, A. Dodabalapur, *Adv. Mater.* **2007**, *19*, 4028–4032; b) H. Yan, Y. Zheng, R. Blache, C. Newman, S. Lu, J. Woerle, A. Facchetti, *Adv. Mater.* **2008**, *20*, 3393–3398; c) T. N. Ng, S. Sambandan, R. Lujan, A. C. Arias, C. R. Newman, H. Yan, A. Facchetti, *Appl. Phys. Lett.* **2009**, *94*, 233307-1–233307-3.
- [67] C. Piliego, F. Cordella, D. Jarzab, S. Lu, Z. Chen, A. Facchetti, M. A. Loi, *Appl. Phys. A* **2009**, *95*, 303–308.

- [68] M. Stolte, M. Gsänger, R. Hofmockel, S.-L. Suraru, F. Würthner, *Phys. Chem. Chem. Phys.* **2012**, *14*, 14181–14185.
- [69] S.-L. Suraru, U. Zschieschang, H. Klauk, F. Würthner, *Chem. Commun.* **2011**, *47*, 11504–11506.
- [70] a) M. Petit, R. Hayakawa, Y. Shira, Y. Wakayama, J. P. Hill, K. Ariga, T. Chikyow, *Appl. Phys. Lett.* **2008**, *92*, 163301-1–163301-3; b) C. Liu, Z. Liu, H. T. Lemke, H. N. Tsao, R. C. G. Naber, Y. Li, K. Banger, K. Müllen, M. N. Nielsen, H. Sirringhaus, *Chem. Mater.* **2010**, *22*, 2120–2124; c) J. H. Oh, W.-Y. Lee, T. Noe, W.-C. Chen, M. Könemann, Z. Bao, *J. Am. Chem. Soc.* **2011**, *133*, 4204–4207.
- [71] a) W. K. Chan, Y. Chen, Z. Peng, L. Yu, *J. Am. Chem. Soc.* **1993**, *115*, 11735–11743; b) G. Lange, B. Tieke, *Macromol. Chem. Phys.* **1999**, *200*, 106–112.
- [72] a) Z. Hao, A. Iqbal, *Chem. Soc. Rev.* **1997**, *26*, 203–213; b) O. Wallquist, R. Lenz, *Macromol. Symp.* **2002**, *187*, 617–630.
- [73] L. Bürgi, M. Turbiez, R. Pfeiffer, F. Bienewald, H.-J. Kirner, C. Winnewisser, *Adv. Mater.* **2008**, *20*, 2217–2224.
- [74] J. C. Bijleveld, A. P. Zoombelt, S. G. J. Mathijssen, M. M. Wienk, M. Turbiez, D. M. de Leeuw, R. A. J. Janssen, *J. Am. Chem. Soc.* **2009**, *131*, 16616–16617.
- [75] a) T. L. Nelson, T. M. Young, J. Liu, S. P. Mishra, J. A. Belot, C. L. Balliet, A. E. Javier, T. Kowalewski, R. D. McCullough, *Adv. Mater.* **2010**, *22*, 4617–4621; b) Y. Li, S. P. Singh, P. Sonar, *Adv. Mater.* **2010**, *22*, 4862–4866; c) S. Cho, J. Lee, M. Tong, J. H. Seo, C. Yang, *Adv. Funct. Mater.* **2011**, *21*, 1910–1916; d) Y. Li, P. Sonar, S. P. Singh, M. S. Soh, M. van Meurs, J. Tan, *J. Am. Chem. Soc.* **2011**, *133*, 2198–2204; e) P. Sonar, S. P. Singh, Y. Li, Z. Ooi, T. Ha, I. Wong, M. S. Soh, A. Dodabalapur, *Energy Environ. Sci.* **2011**, *4*, 2288–2296; f) A. R. Mohebbi, J. Yuen, J. Fan, C. Munoz, M. F. Wang, R. S. Shirazi, J. Seifert, F. Wudl, *Adv. Mater.* **2011**, *23*, 4644–4648.
- [76] H. Bronstein, Z. Chen, R. S. Ashraf, W. Zhang, J. Du, J. R. Durrant, P. S. Tuladhar, K. Song, S. E. Watkins, Y. Geerts, M. M. Wienk, R. A. J. Janssen, T. Anthopoulos, H. Sirringhaus, M. Heeney, I. McCulloch, *J. Am. Chem. Soc.* **2011**, *133*, 3272–3275.
- [77] H. Yanagisawa, J. Mizuguchi, S. Aramaki, Y. Sakai, *Jpn. J. Appl. Phys.* **2008**, *47*, 4728–4731.
- [78] M. Tantiwiwat, A. Tamayo, N. Luu, X.-D. Dang, T.-Q. Nguyen, *J. Phys. Chem. C* **2008**, *112*, 17402–17407.
- [79] S.-L. Suraru, U. Zschieschang, H. Klauk, F. Würthner, *Chem. Commun.* **2011**, *47*, 1767–1769.

- [80] Y. Zhang, C. Kim, J. Lin, T.-Q. Nguyen, *Adv. Funct. Mater.* **2012**, *22*, 97–105.
- [81] Y. Qiao, Y. Guo, C. Yu, F. Zhang, W. Xu, Y. Liu, D. Zhu, *J. Am. Chem. Soc.* **2012**, *134*, 4084–4087.
- [82] a) S. Dähne, *Science* **1978**, *199*, 1163–1167; b) S. R. Marder, B. Kippelen, A. K.-Y. Jen, N. Peyghambarian, *Nature* **1997**, *388*, 845–851; c) F. Würthner, R. Wortmann, K. Meerholz, *ChemPhysChem* **2002**, *3*, 17–31.
- [83] a) A. Mishra, R. K. Behera, P. K. Behera, B. K. Mishra, G. B. Behera, *Chem. Rev.* **2000**, *100*, 1973–2012; b) A. V. Kulinich, A. A. Ishchenko, *Russ. Chem. Rev.* **2009**, *78*, 141–164.
- [84] a) S. R. Marder, B. Kippelen, A. K. Y. Jen, N. Peyghambarian, *Nature* **1997**, *388*, 845–851; b) V. Z. Shirinian, A. A. Shimikin, *Top. Heterocycl. Chem.* **2008**, *14*, 75–105.
- [85] K. Kudo, M. Yamashina, T. Morizumi, *Jpn. J. Appl. Phys.* **1984**, *23*, 130.
- [86] F. Würthner, K. Meerholz, *Chem. Eur. J.* **2010**, *16*, 9366–9373.
- [87] a) N. M. Kronenberg, M. Deppisch, F. Würthner, H. W. A. Lademann, K. Deing, K. Meerholz, *Chem. Commun.* **2008**, 6489–6491; b) H. Bürckstümmer, N. M. Kronenberg, M. Gsänger, M. Stolte, K. Meerholz, F. Würthner, *J. Mater. Chem.* **2010**, *20*, 240–243; c) N. M. Kronenberg, H. Bürckstümmer, M. Deppisch, F. Würthner, K. Meerholz, *J. Photonics Energy* **2011**, *1*, 011101-1–011101-7; d) V. Steinmann, N. M. Kronenberg, M. R. Lenze, S. M. Graf, D. Hertel, K. Meerholz, H. Bürckstümmer, E. V. Tulyakova, F. Würthner, *Adv. Energy Mater.* **2011**, *1*, 888–893; e) H. Bürckstümmer, E. V. Tulyakova, M. Deppisch, M. R. Lenze, N. M. Kronenberg, M. Gsänger, M. Stolte, K. Meerholz, F. Würthner, *Angew. Chem.* **2011**, *123*, 11832–11836; *Angew. Chem. Int. Ed.* **2011**, *50*, 11628–11632.
- [88] L. Huang, M. Stolte, H. Bürckstümmer, F. Würthner, *Adv. Mater.* **2012**, *24*, 5750–5754.
- [89] a) L. Beverina, P. Salice, *Eur. J. Org. Chem.* **2010**, 1207–1225; b) S. Sreejith, P. Carol, P. Chithra, A. Ajayaghosh, *J. Mater. Chem.* **2008**, *18*, 264–274.
- [90] a) G. Wei, S. Wang, K. Sun, M. E. Thompson, S. R. Forrest, *Adv. Energy Mater.* **2011**, *1*, 184–187; b) X. Xiao, G. Wei, S. Wang, J. D. Zimmerman, C. K. Renshaw, M. E. Thompson, S. R. Forrest, *Adv. Mater.* **2012**, *24*, 1956–1960.
- [91] D. Bagnis, L. Beverina, H. Huang, F. Silvestri, Y. Yao, H. Yan, G. A. Pagani, T. J. Marks, A. Facchetti, *J. Am. Chem. Soc.* **2010**, *132*, 4074–4075.
- [92] E. C. P. Smits, S. Setayesh, T. D. Anthopoulos, M. Buechel, W. Nijssen, R. Coehoorn, P. W. M. Blom, B. de Boer, D. M. de Leeuw, *Adv. Mater.* **2007**, *19*, 734–738.

- [93] M. Binda, T. Agostinelli, M. Caironi, D. Natali, M. Sampietro, L. Beverina, R. Ruffo, F. Silvestri, *Org. Electron.* **2009**, *10*, 1314–1319.
- [94] C. Zhang, X. Zhang, X. Zhang, X. Ou, W. Zhang, J. Jie, J. C. Chang, C.-S. Lee, S.-T. Lee, *Adv. Mater.* **2009**, *21*, 4172–4175.
- [95] K. C. Deing, U. Mayerhöffer, F. Würthner, K. Meerholz, *Phys. Chem. Chem. Phys.* **2012**, *14*, 8328–8334.
- [96] Dr. Ulrich Mayerhöffer, PhD thesis, Universität Würzburg (DE), **2012**.
- [97] K. A. Kistler, C. M. Pochas, H. Yamagata, S. Matsika, F. C. Spano, *J. Phys. Chem. B* **2012**, *116*, 77–86.
- [98] F. Würthner, T. E. Kaiser, C. R. Saha-Möller, *Angew. Chem.* **2011**, *123*, 3436–3473; *Angew. Chem. Int. Ed.* **2011**, *50*, 3376–3410.
- [99] a) P. K. Nayak, N. Periasamy, *Org. Electron.* **2009**, *10*, 1396–1400; b) Z. Chen, P. Müller, T. M. Swager, *Org. Lett.* **2006**, *8*, 273–276; c) H. Klauk, U. Zschieschang, R. T. Weitz, H. Meng, F. Sun, G. Nunes, D. E. Keys, C. R. Fincher, Z. Xiang, *Adv. Mater.* **2007**, *19*, 3882–3887.
- [100] a) W. J. Kim, W. H. Koo, S. J. Jo, C. S. Kim, H. K. Baik, *J. Vac. Sci. Technol. B* **2005**, *23*, 2357–2362; b) H. Jung, T. Lim, Y. Choi, M. Yi, J. Won, S. Pyo, *Appl. Phys. Lett.* **2008**, *92*, 163504.
- [101] The shearing device was developed in cooperation with Michael Ramold from the workshop of the Department of Organic Chemistry of the University of Würzburg and Dr. Matthias Stolte.
- [102] The design drawing was done by Michael Ramold from the workshop of the Department of Organic Chemistry of the University of Würzburg.
- [103] D. I. James, J. Smith, M. Heeney, T. D. Anthopoulos, A. Salleo, I. McCulloch in *Organic Electronics II: More Materials and Applications, 1st ed.* (Ed.: H. Klauk), Wiley-VCH, Weinheim, **2012**, pp. 3–26.
- [104] a) J. L. West, G. R. Magyar, J. R. Kelly, *Appl. Phys. Lett.* **1995**, *67*, 155–157. b) S. W. Culligan, Y. Geng, S. H. Chen, K. Klubek, K. M. Vaeth, C. W. Tang, *Adv. Mater.* **2003**, *15*, 1176–1180. c) T. Nishizawa, H. K. Lim, K. Tajima, K. Hashimoto, *J. Am. Chem. Soc.* **2009**, *131*, 2464–2465.
- [105] W. Liptay in *Excited States* (Ed.: E. C. Lim), Academic Press, New York, **1974**, vol. 1, 129–229.
- [106] These measurements were performed by Dr. Matthias Stolte.

- [107] U. Mayerhöffer, M. Gsänger, M. Stolte, B. Fimmel, F. Würthner, *Chem. Eur. J.* **2013**, *19*, 218–232.
- [108] a) E. G. McRae, M. Kasha, *J. Chem. Phys.* **1958**, *28*, 721–722; b) M. Kasha, R. Rawls, M. A. El-Bayoumi, *Pure Appl. Chem.* **1965**, *11*, 371–392.
- [109] The crystal structure was determined with the help of Dr. Christian Burschka.
- [110] W. M. Davis, R. G. Hicks, R. T. Oakley, B. Zhao, *Can. J. Chem.* **1993**, *71*, 180–185.
- [111] These measurements were performed by Prof. Dr. Jens Pflaum.
- [112] *International Tables for Crystallography, Vol. A* (Ed.: Th. Hahn), Kluwer Academic Publishers, Dordrecht, 5th Ed., **2002**.
- [113] For a final proof, whether the molecules adopt the assumed packing arrangement or not further investigations such as in-plane XRD measurements are required, because out-of-plane XRD scans provide only data for planes parallel to the surface.
- [114] a) P. Kubelka, F. Munk, *Z. tech. Phys.* **1931**, *12*, 593–601; b) G. Kortüm, *Reflexionsspektroskopie – Grundlagen, Methodik, Anwendungen*, Springer-Verlag, Berlin, **1969**.
- [115] *Principles of Fluorescence Spectroscopy* (Ed.: J. R. Lakowitz), Kluwer Academic / Plenum, New York, 2nd Ed., **1999**, 52–55.
- [116] A. J. Fry in *Laboratory Techniques in Electroanalytical Chemistry* (Eds.: P. T. Kessing, W. R. Heineman), Marcel Dekker Ltd., New York, 2nd Ed., **1996**, 481.
- [117] G. M. Sheldrick, *Acta Crystallogr., Sect. A: Found. Crystallogr.* **2008**, *A64*, 112–122.
- [118] S. Beckmann, K. H. Etzbach, P. Krämer, K. Lukaszuk, R. Matschiner, A. J. Schmidt, P. Schuhmacher, R. Sens, G. Seybold, R. Wortmann, F. Würthner, *Adv. Mater.* **1999**, *11*, 536–541.

LIST OF PUBLICATIONS

Sequential FRET Processes in Calix[4]arene-Linked Orange-Red-Green Perylene Bisimide Dye Zigzag Arrays

C. Hippus, I. H. M. van Stokkum, M. Gsänger, M. M. Groeneveld, R. M. Williams, F. Würthner, *J. Phys. Chem. C* **2008**, *112*, 2476–2486.

Tailored merocyanine dyes for solution-processed BHJ solar cells

H. Bürckstümmer, N. M. Kronenberg, M. Gsänger, M. Stolte, K. Meerholz, F. Würthner, *J. Mater. Chem.* **2010**, *20*, 240–243.

A Crystal-Engineered Hydrogen-Bonded Octachloroperylene Diimide with a Twisted Core: An n-Channel Organic Semiconductor

M. Gsänger, J. H. Oh, M. Könemann, H. W. Höffken, A.-M. Krause, Z. Bao, F. Würthner, *Angew. Chem.* **2010**, *122*, 752–755; *Angew. Chem. Int. Ed.* **2010**, *49*, 740–743

Efficient Solution-Processed Bulk Heterojunction Solar Cells by Antiparallel Supramolecular Arrangement of Dipolar Donor-Acceptor Dyes

H. Bürckstümmer, E. V. Tulyakova, M. Deppisch, M. R. Lenze, N. M. Kronenberg, M. Gsänger, M. Stolte, K. Meerholz, F. Würthner, *Angew. Chem.* **2011**, *123*, 1183211836; *Angew. Chem. Int. Ed.* **2011**, *50*, 1162811632.

Improved ambient operation of n-channel organic transistors of solution-sheared naphthalene diimide under bias stress

M. Stolte, M. Gsänger, R. Hofmockel, S.-L. Suraru, F. Würthner, *Phys. Chem. Chem. Phys.* **2012**, *14*, 14181–14185.

Synthesis and Molecular Properties of Acceptor-Substituted Squaraine Dyes

U. Mayerhöffer, M. Gsänger, M. Stolte, B. Fimmel, F. Würthner, *Chem. Eur. J.* **2013**, *19*, 218–232.

Core-Brominated Tetraazaperopyrenes as n-Channel Semiconductors for Organic Complementary Circuits on Flexible Substrates

S. Geib, U. Zschieschang, M. Gsänger, M. Stolte, F. Würthner, H. Wadepohl, H. Klauk, L. H. Gade, *Adv. Funct. Mater.* **2013**, accepted.